2016

Modeling Fluid Interactions with Granular and Fibrous Surfaces

Mana Mokhtabad Amrei

Modeling Fluid Interactions with Granular and Fibrous Surfaces

A dissertation submitted in partial fulfillment of the requirements for the degree of Doctor of Philosophy at Virginia Commonwealth University.

by

Mana Mokhtabad Amrei

M.Sc. Aerospace Enginering, Sharif University of Technology, Tehran, Iran, 2009

Director: Hooman V. Tafreshi

Professor, Department of Mechanical and Nuclear Engineeing

Virginia Commonwealth University

Richmond, Virginia

Dec, 2016

Dedication

I would like to dedicate this work to my fiancé, Brian Murphy whose love and support made it possible for me to complete this work. I also dedicate it to my mother, Parvaneh and my father, Hossein and to my sisters Diba and Parissa, who through the thick and thin, have been there for me. Their encouragement and drive is what has made me who I am.

Acknowledgment

I wish to express my sincere thanks to my advisor and my mentor Prof. Hooman V. Tafreshi for his contiuous support of my scientific endeavors; valuable guidance, and encouragement.

I would also like to extend my feeling of gratitude to my committee members—Prof. Ken Wynne, Prof. Daren Chen, Prof. Christina Tang, Prof. Jayasimha Atulasimha and Prof. Reza Mohammadi for their insightful questions and comments which have helped strengthen my work.

My family, friends and my labmates for their love, patience, guidance, and inspiration. I will always be grateful to Shahla Pishdad and my American family Sherrie and Joe Kashinejad for their support during my first years in US.

I want to express my appreciation to various sources of funding during my graduate education: National Science Foundation, and Virginia Commonwealth University.

Table of Contents

List of Figures

length (c) as a function of hydrostatic pressure for COPDs with different population fractions of particles with $\theta_1 = 100^{\mathrm{o}}$ and $\theta_2 = 120^{\mathrm{o}}$ for an SVF of $\varepsilon = 0.4$ and a particle diameter of $d = 100$ µm.

Fig. 2.5 The equivalent contact angle concept shown schematically with the relationship between the angles and directions.

Fig. 2.6 CHP predictions, obtained from FB and SE calculations for bi-component COPDs comprised of particles with $\theta_1 = 100^{\mathrm{o}}$ and $\theta_2 = 120^{\mathrm{o}}$ and diameters of $d = 100$ µm and $d = 1$ µm. (a) and (b) show the case with positive and negative pressures, respectively.

Fig. 2.7 Variations of wetted area with hydrostatic pressure obtained from FB and SE calculations for COPDs having $\theta_1 = 100^{\mathrm{o}}$, $\theta_2 = 120^{\mathrm{o}}$ with $d = 100$ µm for $n_1^c = 0.25$.

Fig. 2.8 An example Voronoi diagram produced for a CRPD with an SVF of $\varepsilon = 0.25$ comprised of 34 particles is shown in (a). The AWI for the case of particles with a YLCA of $\theta = 120^{\mathrm{o}}$ at positive and negative CHPs of $P_h = 169$ kPa and $P_h = -40$ kPa are shown in (b) and (c) along with their height contour plots in (d) and (e) $P_h = -40$ kPa, respectively. The corresponding critical immersion angles are plotted for each particle and shown in (f) and (g). Note the location of the failure point shown with an arrow in (f) and (g).

Fig. 2.9 CHP predictions, obtained from FB and SE calculations for CRPDs and their ordered counterparts are shown in (a) and (b) for positive and negative pressures, respectively, along with their corresponding bubble volume ratios in the offset.

Fig. 2.10 CHP predictions vs. SVF, obtained from FB and SE calculations for bi-component CRPDs having $\theta_1 = 100^{\mathrm{o}}$ and $\theta_2 = 120^{\mathrm{o}}$ with population fractions of $n_1^c \cong 0.5$, are given in (a). Wetted area as a function of hydrostatic pressure obtained using from SE for CRPDs is shown in (b). Wetted area for CRPDs and their ordered counterparts are given in (c). Dimensionless slip length as a function of hydrostatic pressure for CRPDs having $\theta = 120^{\mathrm{o}}$ and bi-component CRPDs having $\theta_1 = 100^{\mathrm{o}}$, $\theta_2 = 120^{\mathrm{o}}$ and $n_1^c \cong 0.5$ are presented in (d).

pressure (b). A new stable AWI forms in Regime II (c). Further increase in the hydrostatic pressure causes the AWI to penetrate deeper into the coating as shown in (d).

Fig. 3.7 Critical capillary pressure predictions obtained from FB and SE calculations for mono-dispersed coatings comprised of particles with $d_1 = 100$ μm and $d_2 = 1$ μm.

Fig. 3.8 The minimum points for an AWI are shown with z_1 and z_2 at the cell boundary and cell center, respectively in (a). Maximum coarse-to-fine particle diameter ratio versus SVF for mono-dispersed coatings with different YLCAs is shown in (b).

Fig. 3.9 CCP values obtained from FB and SE calculations for bi-dispersed coatings having a coarse particle diameter of $d_1 =$ μm and an YLCA of $\theta = 120^{\circ}$ are given in (a) and (b) for with η =1.75 and η =2.5, respectively. CHPs for coatings of figure (a) are shown in (c).

Fig. 3.10 Wetted area versus hydrostatic pressure obtained from ED and SE calculations for bi-dispersed coatings having ε_b=0.2 and η =1.57 are shown in (a) for $n_1 = 0.75$, in (b) for $n_1 = 0.50$, and in (c) for $n_1 = 0.25$. Dimensionless slip length is presented as a function of hydrostatic pressure for bi-dispersed coatings having SVF of 0.2 and η =1.57 in (d).

Fig. 3.11 CCP (a) and CHP (b) predictions from FB and SE calculations for poly-dispersed coatings with ordered particle arrangements having different SVFs and YLCAs.

Fig. 3.12 Wetted area (a) and dimensionless slip length (b) versus hydrostatic pressure obtained from VED and SE calculations for bi-dispersed coatings with random particle distributions having ε_b=0.25, $n_1 = 0.5$, $d_1 = 100$ μm or 175 μm, and $\eta = 1.75$ or 2.5 in Regime II. AWI examples over these coatings are shown in (c) at a hydrostatic pressure of $P_h = 80$ kPa.

Fig. 3.13 Our CCP and CHP predictions are presented in (a) and (b) along with the SE results for poly-dispersed coatings with randomly distributed particles, respectively. The coatings consist of particles with diameters and YLCAs of $d_1 = 100$ μm, $\theta_1 = 120^{\circ}$, $d_2 = 57$ μm, $\theta_2 = 100^{\circ}$, $d_3 = 40$ μm, $\theta_3 = 80^{\circ}$, $d_4 = 31$ μm, and $\theta_4 = 60^{\circ}$. Wetted area and dimensionless slip length are reported for poly-dispersed coatings with $\varepsilon_p = 0.2$ in (c) and (d), respectively.

Detachment force obtained from experiment and numerical simulation for a single fiber is shown in (b). Droplet shape change in response to magnetic force is shown in (c) and (d) for droplets with a volume of 2.5 μL and 0.5 μL, respectively. The images on the left are taken in the absence of magnetic force (i.e., g = -9.8 N/kg), images on the right show the droplet residual on the fibers after detachment. $\theta_{YL} = 50^\circ$.

Fig. 6.5 Droplet shape from top (top row) and side (bottom row) views for $\alpha = 45^\circ$and 90° is given in (a). The images in the top row are taken in the absence of magnetic force (i.e., g = -9.8 N/kg) while the images in the bottom row show the droplet influenced by an out-of-plane magnetic force before detachment. Out-of-plane detachment force is shown in (b) as a function of the relative angle between the fibers. Experimental and computational data are shown with red and black symbols, respectively. Square, circle, diamond, gradient, and delta represent droplet volumes of 0.5 μL, 1 μL, 1.5 μL, 2.0 μL, and 2.5 μL, respectively. $\theta_{YL} = 50^\circ$.

Fig. 6.6 Droplet shape from side view is given in (a) for $\alpha = 60^\circ$and 150°. The images in the top row are taken in the absence of magnetic force (i.e., g = -9.8 N/kg) while the images in the bottom row show the droplets influenced by an in-plane magnetic force in the upward direction (direction bisecting the relative angle between the fibers) before detachment. In-plane detachment force is shown in (b) as a function of the relative angle between the fibers. Experimental and computational data are shown with red and black symbols, respectively. $\theta_{YL} = 50^\circ$.

Fig. 6.7 Droplet shape from side view is given in (a) for $\alpha = 90^\circ$. The images in the top row are taken in the absence of magnetic force (i.e., g = -9.8 N/kg) while the images in the bottom row show the droplets influenced by an in-plane magnetic force in the upward direction with $\phi = 20^\circ$ and 40° before detachment. In-plane detachment force is shown in (b) and (c) as a function of ϕ for $\phi + \psi = 90^\circ$and $+\psi = 150^\circ$, respectively. Experimental and computational data are shown with red and black symbols, respectively. $\theta_{YL} = 50^\circ$.

Abstract

Modeling Fluid Interactions with Granular and Fibrous Surfaces

By: Mana Mokhtabad Amrei, Ph.D.

A dissertation submitted in partial fulfillment of the requirements for the degree of Doctor of Philosophy at Virginia Commonwealth University.

Virginia Commonwealth University, 2016

Director: Hooman V. Tafreshi, Professor
Professor, Mechanical and Nuclear Engineeing Department

Understanding the interactions between a body of liquid and a curvy surface is important for many applications such as underwater drag force reduction, droplet filtration, self-cleaning, and fog harvesting, among many others. This study investigates ways to predict the performance of granular and fibrous surfaces for some of the above applications. More specifically, our study is focused on 1) modeling the mechanical stability of the air-water interface over submerged superhydrophobic (SHP) surfaces and their expected drag reduction benefits, and 2) predicting the mechanical stability of a droplet on a fiber in the presence of an external body force. For the first application, we modeled the air–water interface over submerged superhydrophobic coatings comprised of particles/fibers of different diameters or Young–Laplace contact angles. We developed mathematical expressions and modeling methodologies to determine the maximum depth to which such coatings can be used for underwater drag reduction as well as the magnitude of the depth-dependent drag reduction effect of the surface. For the second application, we studied the force required to detach a droplet from a single fiber or from two crossing fibers. The results of our numerical simulations were compared to those obtained from experiment with ferrofluid

droplets under a magnetic field, and excellent agreement was observed. Such information is of crucial importance in design and manufacture of droplet–air and droplet–fluid separation media, fog harvesting media, protective clothing, fiber-reinforced composite materials, and countless other applications.

Chapter 1. Introduction

1.1 Background Information

The interaction between liquid and a solid happens everywhere on a daily basis and its description is one of the important aspects of fluid dynamics. In this research we limit ourselves to study the interaction between the air-water interface (AWI) and different surfaces (granular coating, fibrous coating, surface of a single fiber and surface of crossing fibers). The shape of AWI over these surfaces is controlled by capillarity force -the cohesive forces among liquid molecules- in balance with other external forces. The AWI is deformable i.e., is free to change the shape in order to minimize the free energy which makes the physics of AWI sitting over media very complex (3).

On the other hand, the interaction between fiber and small droplets is another aspect of predicting the interaction of liquid and fibers. Drop on flat surfaces are widely discussed (4–8) but fewer researches have been focused on drop on fibers. In the following subsections the background information about capillarity force, fluid interactions with particles and with fibers are presented.

1.1.1 Capillarity Force

Capillarity is the physical mechanism resulted by surface, or interfacial forces which establish the conditions of two immiscible fluids i.e., shape and position of the deformable interface between them (3). The surface tension over the interface, for example, a droplet in midair causes the droplet to conform to a spherical shape within the constraints of forces such as air resistance and gravity. Concept of surface tension was first introduced by Young and Laplace in 1800s (9). Young formulated the wettability of a substrate in terms of contact angle between the liquid-gas and solid-liquid interface as

$$\sigma \quad cos\theta = \sigma_{SG} - \sigma_{SL} \tag{1.1}$$

Where σ, σ_{SG} and σ_{SL} represent the interfacial tensions of liquid-gas, solid-gas, and solid-liquid, respectively.

The result of the work of Laplace on capillary action states that the pressure difference across the interface –capillary pressure ΔP_{cap}- is proportional to the interfacial tension σ and depends on the curvature of surface at the considered point and can be written as a function of principal radii R_1^* and R_2^* as

$$\Delta P_{cap} = \sigma(\frac{1}{R_1^*} + \frac{1}{R_2^*}) \tag{1.2}$$

Since then, many researchers have worked on the interface shape and stability over different surfaces (10–15).

1.1.2 Fluid Interactions with Granular/Fibrous Coatings

Fluid interaction with a surface is affected by the wetting behavior of the solid surface which is determined by both the chemical composition and the geometrical attributes of the surface. Substrate topology can potentially alter the wetting behavior of the substrate of a given chemical composition (16). Thus, it is important to study the role of substrate topology on the spreading mechanism of a droplet.

Surface wetting behavior is categorized into two categories: hydrophobic surface (contact angle above 90◦) and hydrophilic surface (contact angle below 90◦). Superhydrophobicity could be achieved by a combination of low surface energy and micro- or nanoscale surface structure. Therefore, a hydrophilic substrate surface will be altered to a superhydrophobic (SHP) substrate by topographical modifications e.g., adding granular or fibrous coating to the surface. The

Superhydrophobicity is known for having static contact angles exceeding 150° and low contact-angle hysteresis and been subject of many studies (17–20). Examples of such surfaces in nature are the self-cleaning lotus leaves and water striders. The self-cleaning properties of Lotus leaves have motivated many studies in the past decade to investigate the superhydrophobicity effect (14). Superhydrophobic surfaces are often produced by imprinting micro- or nano-scale structures on a hydrophobic substrate or by chemically treating the surface of a substrate with the desired roughness (see e.g., among many others) as mentioned before (21,22). An alternative, perhaps more cost-effective, approach to micro-fabrication is to coat the substrate with a porous hydrophobic material, e.g., Polystyrene electrospun nanofibers or pulverized aerogel particles, where the pores of the coating serve as the above-mentioned roughness (23–27). In addition, SHP surfaces may also be used to reduce the drag force on an object submerged in moving water due to its ability to entrap air (10,12,15,22,28–31). When the pores in an SPH surface are completely filled with air, the surface is considered to be at the Cassie state. If the hydrostatic pressure over the surface is too high, water starts penetrating into the pores compressing the entrapped air (the case of closed pores) and finally fully wets the surface (Wenzel state) (32,33). The hydrostatic pressure at which a SHP surface starts departing from the Cassie state is referred to as the critical hydrostatic pressure (CHP) (34). This definition is often used in the context of pores with sharp-edged entrance where the AWI can anchor (pin) itself to the edges of the pore. In this case, the slope of the AWI at the wall increases by increasing the hydrostatic pressure up to the slope corresponding to the Young–Laplace contact angle (or an advancing contact angle) while the AWI is pinned. Increasing the hydrostatic pressure beyond this pressure can only result in the AWI detachment from the edges and moving downward into the pore with a fixed profile (while pressurizing the air entrapped below it). The AWI may reach the bottom of the pore, instantly if the hydrostatic pressure is high enough, or as the entrapped air eventually dissolves into water. Note that the entrapped air continuously dissolves in the ambient water, and the rate of dissolution increases with hydrostatic pressure (34). The definition of CHP is less clear when the pore entrance is round. This is because in this case, the AWI cannot anchor itself to any sharp corner, and has to conform to a shape that maintains YLCA at any point along the curved wall of the pore. Therefore, it is hard to define a fully dry (Cassie) state as the AWI has already entered the pore. Obviously, the AWI moves further down into the pore in response to any increase in the hydrostatic pressure. For the lack of a better alternative, we define critical pressure for a pore with round entrance, to be the hydrostatic pressure at which the AWI moves down into the pore to reach a highest capillary pressure (35,36). A transition to the Wenzel state can also occur if the AWI touches the bottom of the pore (either with sharp of round entrance) before reaching the critical pressure. This has been identified in the literature as failure due to AWI sagging or the lack of "robustness height" (11). In addition, the entrapped air continuously dissolves in the ambient water which causes Wenzel state with time (34,37).

To predict the drag-reduction achievable from a given SHP surface in a specific hydrodynamic condition, Navier–Stokes equations should be solved simultaneously with the equation for the transient shape of the AWI. This is a multi-scale 3-D unsteady-state two-phase flow problem, and the solution depends strongly on the microstructure of the surface. Given the complexity of the problem, the current study is limited to the effects of hydrostatic pressure on the wetted area of granular/fibrous SHP coatings. This is because even without solving the Navier–Stokes equations, one can disqualify a large group of coatings or operating conditions using relevant information about the wetted area of the coating.

Two different approaches are available to solve for 3-D shape of the AWI: 1) the balance of the forces that act on the interface and 2) the energy minimization approach. The force balance equation will be used for theoretical part of the work whenever is possible. For the numerical part the energy minimization approach has been used. For numerical simulations we used public domain software called the Surface Evolver (SE). The SE code is able to solve for the minimum-energy shape of an interface between two immiscible fluids. The general form of the energy equation E being integrated in the code can be expressed as (38,39):

$$E = p \iiint dv + \iint \sigma dA_{LG} - \sum \sigma cos\theta_i \iint dA_i \tag{1.3}$$

where p is the applied pressure difference across the interface which is being integrated over volume element dV. A_{LG} represents the liquid-gas area. The summation refers to the surface energy contributed by the wetted area of each particle/fiber associated with the interface dA_ie. To ensure proper calculation of the particle\fibers' energy contribution, the integrand dA_i must be derived for each AWI face and applied explicitly in the code. This approach will give us the shape of the interface and consequently the ability to calculate the wetted area A_w which is the solid-liquid area per unit area of a flat surface. Drag reduction is often characterized in terms of slip length; the imaginary distance below the slip-generating surface at which the water velocity extrapolates to zero (10). The slip length on a SHP surface is related to A_w, and is therefore pressure dependent. While there are several studies proposing an explicit relationship between slip length and A_w for internal flows over SHP surface comprised of streamwise or transverse sharp-edged grooves, the literature is scarce when it comes to slip length correlations for SHP surfaces made of particles. A relevant work to be used here in studying the slip length over granular\fibrous SHP surfaces is that of Srinivasan et al., who proposed an expression for the slip length over SHP monofilament woven screens in flow between two parallel plates (1):

$$b = \frac{L_s}{3\pi} ln\left(\frac{2(1+\sqrt{1-A_w})}{\pi\, A_w}\right) \tag{1.4}$$

Note that above was originally developed with the assumption that the woven screens have planar structures, i.e., A_w never exceeds 1. This assumption, however, is not accurate for granular coatings. Nevertheless, in the absence of a better alternative, we use this expression here as a means of discussing the effects of pressure on slip length, but only as long as $A_w \leq 1$.

Section 1.3 presents more details of how to predict air-water interface shape and stability over superhydrophobic coating comprised of poly-dispersed particles or fibers with different diameter and wettabilities.

1.1.3 Droplet Interactions with Fibers

The dynamics of wetting has received significant attention for years and still is an important topic. Wettability of the fibers is important to many industries such as coating processes, textile fabrication, self cleaning processes and filtration of fluids. In liquid-liquid filtration understanding the droplet displacement over the fiber surface and the dynamics of wetting behavior is crucial (40,41). Previous work has considered droplet on flat surfaces or fibrous coatings (42–45). Due to the cylindrical shape of the fiber, the wetting behavior of droplets on fibers differs from the wetting of flat surfaces. Early studies on the wetting phenomena of droplet-on-fiber systems have reported on determining the droplet shape and on extracting the contact angle accurately (46). These works details the measurement of the contact angle of a droplet on a cylindrical fiber (which is different from the contact angle that the same liquid would form on a flat plate). A number of previous studies of the droplets on fibers have dealt with the stability of droplet conformations, contact angles, and droplet geometry (47,48). Depending on the fiber radius, droplet volume and the surface energy of the fiber, two fundamentally different conformations of macroscopic droplets has been found (i.e., barrel and clam-shell conformations). Barrel shapes occur for large droplets relative to the fiber radius or for low contact angles. Clam-shell shapes occur for small droplets or high contact angles. However, for some certain droplet volume and fiber radius coexistence of both conformations has been observed (49). Droplet profile for barrel shape conformation for a known contact angle was also been described. Few studies also described the shape of the droplet in gravity field (50,51). Motion of the drop due to temperature gradient, gradient of cross-sectional radius of the fiber (conical fibers), and rolling motion of the contact line due to droplet spreading has also been studied experimentally (52–54). Despite the prevalence of such technology in industry, few researches investigated the drop motion on fibers due to external forces (e.g., drag force or magnetic force). Such motion can be described by time-dependant shape of the droplet, contact angle hysteresis (the difference between advancing and receding contact angle), internal viscous fluid motion, moving advancing and receding contact lines and boundary layer separation at a drop surface. Semi-empirical correlations have been reported to relate droplet mobility (along the fiber or perpendicular to the fiber) to volume of the droplet, surface tension, Reynolds number and capillary number (relative effect of viscous forces versus surface tension) which are applicable only over a narrow set of parameters (55–58). Contact angle hysteresis is the dominant factor to describe droplet motion over non-ideal fibers. Two different approaches have been proposed to explain the mechanism of contact angle hysteresis: adhesion hysteresis and mechanical pinning by defect. Adhesion hysteresis is due to dissipation of energy due to irreversibility of the motion.

While mechanical pinning is due to the inhomogenrities on a microscopic level, therefore, cannot happen for ideally smooth surfaces.

1.2 Overall Objectives of This Thesis

This dissertation develops necessaey models to predict fluid interactions with granular and fibrous surfaces for two distinct applications: 1) modeling the stability of the air-water interface over submerged superhydrophobic (SHP) surfaces, and the expected drag reduction effect generated by the surface, and 2) predicting droplet-fiber wettability and modeling droplet motion along\normal to fibers and fiber assemblies.

First, we model the air-water interface over submerged superhydrophobic coatings comprised of particles/fibers at differene pressures. We also studiy the effect of diameters and Young-Laplace contact angles. Our goal here is to develop simple ways (mathematical expressions or modeling strategies) to determine whether or not such coatings can be applied to a submersible vehicle for drag reduction (or similar) purposes by predicting how the solid-liquid area -and consequently surface slip length- varies with the depth at which the vehicle operates. Obviously, the formulations and methodologies that developed in this study can also be applied to granular/fibrous superhydrophobic coatings used in air for self-cleaning applications, among many others.

For the second application, we develop a computational method for predicting the force required to detach a droplet from a smooth\rough\trilobal fiber. This information is crucially important for understanding the dynamics, coalescence, and migration of liquid droplets in fibrous structures. The work begins with studying the interactions between a droplet and a single fiber and moves on to include additional fibers. The effect of different parameters (such as the fiber diameter, fiber wettabilities, the relative angles between fibers, relative size of fiber and droplet) on the force required to move the droplet along (or normal to) the fibers are studied thoroughly using numerical simulation and also experiment with ferrofluid in magnetic field.

The effect of hydrostatic pressure on air-water interface stability and wetted area of submerged monodispersed granular coating is provided in Chapter 2. We develop simple ways (mathematical expressions and modeling strategies) to determine slip length for a randomly distributed particle arrangemet to find out whether or not such coatings can be applied to a submersible vehicle for drag reduction (or similar) purposes. Effects of particle diameter, particle contact angles, particle packing fraction, and spatial distribution on positive and negative critical hydrostatic pressures and their corresponding wetted area are predicted and discussed in detail.

Chapter 3 is the extension of the work of chapter 2 to poly-disperesed coatings. Drag reduction associated to such coatings is calculated by introducing a simple analytical model to find the stability of the air-water interface and wetted area at a given pressure.

Chapter 4 establishes a model for predicting the resistance of superhydrophobic fiberous coatings to hydrostatic pressures. We generate simulation domains which represent orthogonal distribution of fibers, coatings with oriented finers and also wire screen coatings. We determine the shape and surface area of the minimum-energy state of air–water interface that exists between the fibers at some given pressure.

Chapter 5 reports on our investigation of the effects of surface roughness on the equilibrium shape and apparent contact angles of a droplet deposited on a fiber. In particular, the shape of a droplet deposited on a roughened fiber is studied. Sinusoidal roughness varying in both the longitudinal and radial directions is considered in the simulations to study the effects of surface roughness on the most stable shape of a droplet on a fiber (corresponding to droplet's global minimum energy state). A phase diagram that includes the effects of fiber roughness on droplet configurations—symmetric barrel, clamshell, and asymmetric barrel—is presented for the first time. The results presented in our study have been compared with experiment whenever possible, and good agreement is observed.

In chapter 6 a novel technique is developed to measure the force required to detach a droplet from a fiber or fiber crossovers experimentally by using ferrofluid droplets in a magnetic field. Unlike previous methods reported in the literature, our techniques does not require an air flow or a mechanical object to detach the droplet from the fiber(s), and therefore it simplifies the experiment, and also allows one to study the capillarity of the droplet–fiber system in a more isolated environment. In this chapter, we investigate the effects of the relative angle between intersecting fibers on the force required to detach a droplet from the fibers in the in-plane or out-of-plane direction. The in-plane and through-plane detachment forces are also predicted via numerical simulation and compared with the experimental results. Good agreement was observed between the numerical and experimental results.

The equilibrium shape of droplet on fibers with trilobal cross-section is studied in chapter 7 via numerical simulation. Special attention has been paid to droplet shape on trilobal fibers having different lobe amplitude. In addition, the effects of droplet volume and fiber crossectional orientation with respect to direction of gravity are investigated.

Finally, we will close with our overall conclusions in Chapter 8.

Chapter 2. Effects of Hydrostatic Pressure on Wetted Area of Submerged monodispersed Superhydrophobic Granular Coatings

2.1 Introduction

The self-cleaning properties of Lotus leaves have motivated many studies in the past decade to investigate the superhydrophobicity effect—a phenomenon which may arise from combining hydrophobicity with roughness (59–62). In addition, SHP surfaces may also be used to reduce the drag force on an object submerged in moving water (10,12,14,15,22). This is owing to the fact that a SHP surface can entrap the air in the surface-pores, which is in contact with water, thereby reducing the contact area between water and the solid surface. Depending on the conditions and surface morphology, the Wenzel state (fully wetted), the Cassie state (fully dry), or a series of transition states in between the two extreme states can be expected to prevail over a submerged SHP surface (11,13,19,32–34,63–67). While many studies have been conducted to better our understanding of the Cassie and Wenzel states, not much attention has been paid to the transition states despite their importance. Depending on the microscale geometry of the surface (i.e., roughness) and the hydrostatic/hydrodynamic pressure field, the air–water interface (AWI) may significantly ingress into the pores of the surface. The AWI may stay intact or even become impaled by the peaks of the surface. When the AWI is impaled, even when there is still air in the pores, an SHP surface may no longer provide a reduced solid–water contact area (referred to here as the wetted area), and hence, offers no drag reduction (68–71). In fact, it is quite possible that such a surface increases the drag force in certain hydrodynamic conditions (see the next paragraph).

When the pores in an SPH surface are completely filled with air, the surface is considered to be at the Cassie state. If the hydrostatic pressure over the surface is too high, water may start penetrating into the pores compressing the entrapped air (the case of closed pores). The forces acting on an AWI are due to hydrostatic pressure P_h, ambient pressure P_∞, pressure of the entrapped air, referred to here as the bubble pressure, P_{bub}, and the capillary pressure P_{cap}. The balance of static forces requires that

$$P_{cap} + P_{bub} = P_\infty + P_h \tag{2.1}$$

The bubble and capillary pressures (if positive) tend to resist against the hydrostatic pressure. The hydrostatic pressure at which a SHP surface starts departing from the Cassie state is referred to as the critical hydrostatic pressure (CHP) (16,72–74). This definition is often used in the context of pores with sharp-edged entrance where the AWI can anchor (pin) itself to the edges of the pore. In this case, the slope of the AWI at the wall increases by increasing the hydrostatic pressure up to the slope corresponding to the Young–Laplace contact angle (YLCA) (or an advancing contact angle) while the AWI is pinned (34). Increasing the hydrostatic pressure beyond this pressure can only result in the AWI detachment from the edges and moving downward into the pore with a fixed profile (while pressurizing the air entrapped below it). The AWI may reach the bottom of the pore, instantly if the hydrostatic pressure is high enough, or as the entrapped air eventually dissolves into water. Note that the entrapped air continuously dissolves in the ambient water, and the rate of dissolution increases with hydrostatic pressure (34,37). The definition of CHP is less clear when the pore entrance is round. This is because in this case, the AWI cannot anchor itself to any sharp corner, and has to conform to a shape that maintains YLCA at any point along the curved wall of the pore. Therefore, even at a zero hydrostatic pressure, it is hard to define a fully dry (Cassie) state as the AWI has already entered the pore, as can be seen in Fig. 2.1a. Obviously, the AWI moves further down into the pore in response to any increase in the hydrostatic pressure (13,75–79). For the lack of a better alternative, we define CHP for a pore with round entrance, to be the hydrostatic pressure at which the AWI moves down into the pore to reach a critical immersion angle of $\alpha = \alpha^{cr}$. This angle is defined as the immersion angle for which the capillary pressure P_{cap} is maximum (13,24).

A transition to the Wenzel state can also occur if the AWI touches the bottom of the pore (either with sharp of round entrance) before reaching the critical immersion angle α^{cr}. This has been identified in the literature as failure due to AWI sagging or the lack of "robustness height" (11), and has also been observed in the current study to be the dominant cause of AWI failure when the SVF of the surface is very small (less than about 8% for the set of parameters considered here).

To predict the drag-reduction achievable from a given SHP surface in a specific hydrodynamic condition, Navier–Stokes equations should be solved simultaneously with the equation for the transient shape of the AWI. This is a multi-scale 3-D unsteady-state two-phase flow problem, and the solution depends strongly on the microstructure of the surface. Given the complexity of the problem, the current study is limited to the effects of hydrostatic pressure on the wetted area of granular SHP coatings. This is because even without solving the Navier–Stokes equations, one can disqualify a large group of coatings or operating conditions using relevant information about the wetted area of the coating.

The remainder of this chapter is organized as follows. Our force balance (FB) formulations for calculating the critical hydrostatic pressure (CHP) and wetted area of a granular SHP coating is given in Sec. 2.2. In Sec. 2.3, we present examples of existing analytical expressions for calculating the slip length of a granular SHP surface in terms of wetted area. The results of our analytical formulation regarding the effects of coatings' microstructural and wetting properties on CHP and wetted area are compared and discussed along with those obtained from Surface Evolver (SE) code in Sec. 2.4. In this section, we also discuss the effects of randomness in the spatial distribution of the particles in SHP coatings of identical properties. The conclusions drawn from our work are given Sec. 2.5.

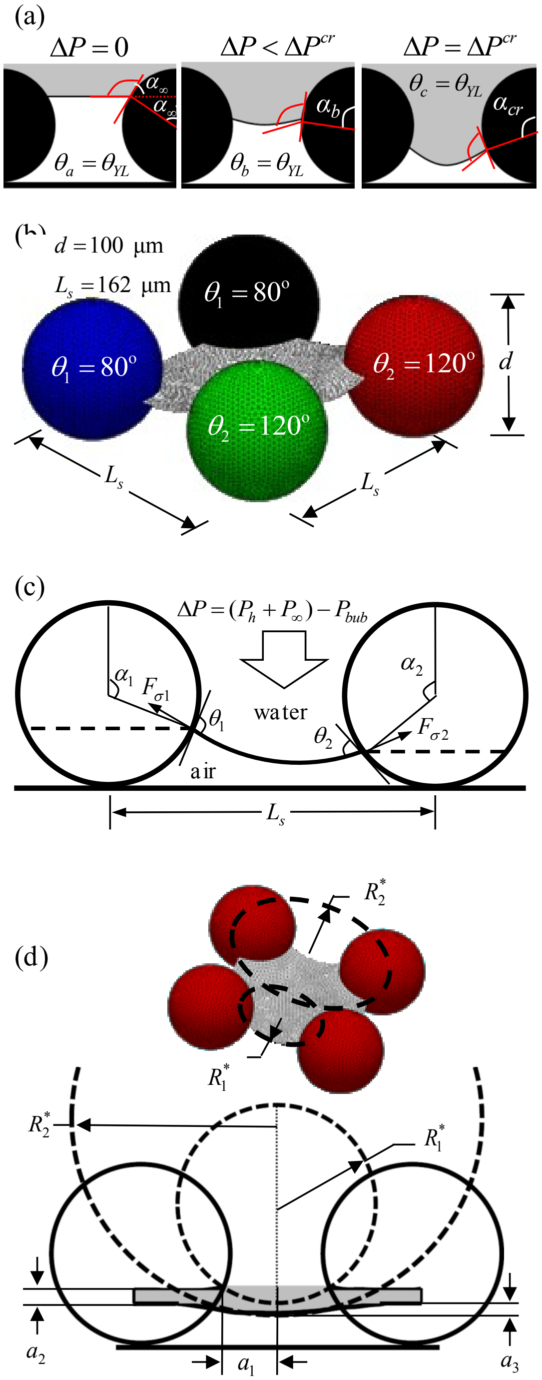

Fig 2.1 Schematic representation of the AWI over a coating made of a layer of equally sized hydrophobic particles as a function of pressure difference (increasing from top to down) is presented in (a). Four particles with a square arrangement representing a unit-cell for our COPDs along with an arbitrary AWI between them produced by SE for $d = 100$ μm, $L_s = 162$ μm, and $P_h = 548$ kPa, $\theta_1 = 80^o$, and $\theta_2 = 120^o$ (b). Force balance diagrams for the case of positive pressure difference across the AWI are given in (c). The AWI radius of curvature at the center of the unit-cell and at the symmetry boundary is shown in (d) and also the volume confined between the curved AWI and the horizontal plane slicing through the particles at contact points (gray-shaded volume) is approximated with a spherical cap added to a cuboids is shown.

2.2 Critical Hydrostatic Pressure and Wetted Area

Consider a layer of four particles with identical diameters but different contact angles deposited on a flat substrate in a square cell, as shown in Fig. 2.1b. Predicting the critical pressure and wetted area for a particle coating is a challenge as it requires detailed information about the 3-D shape of the AWI (both the direction and the magnitude of the capillary force vary depending on the vertical position of the contact-line around a particle). The problem becomes more complicated when the coating is comprised of particles with different YLCAs or when the particles are distributed randomly. In this chapter, the SE code is used to numerically obtain the 3-D shape of the AWI as a function of pressure (see (38,39) for more information about SE code). Figure 2.1b also shows an example of such calculations conducted for a coating with $d = 100$ µm, $L_s = 162$ µm, $\theta_1 = 80^o$, and $\theta_2 = 120^o$ when $P_{cap} = 0.30$ kPa. With the 3-D shape of the AWI available, one can easily calculate the wetted area.

To circumvent the need for running a numerical simulation for each and every combination of parameters, we developed an analytical method that can be used to approximate the CHP and wetted area of a SHP granular coating without actually producing a 3-D shape for the AWI. Considering a force balance (FB) approach for the AWI at equilibrium,

$$\Delta P \left(L_s^2 - \frac{\pi d^2}{4}\sum_{i=1}^{4} n_i sin^2\alpha_i\right) = \pi\sigma d \sum_{i=1}^{4} n_i sin\alpha_i cos\left(\frac{3\pi}{2} - \theta_i - \alpha_i\right) \qquad (2.2)$$

where $\Delta P = P_h + P_\infty - P_{bub}$. The main simplifying assumption in deriving Eq. 2.2 is that the contact-line between the AWI and the solid particles (shown with dashed line in Fig. 2.1c) remains in a horizontal plane. As will be shown later in Sec. 2.3, where we compare the results of our analytical formulations with the numerical results of SE, the error associated with this assumption is generally negligible but increases with increasing the coating's SVF defined as $\varepsilon = \frac{\pi d^2}{6\,L_s^2}$ with $\varepsilon_{max} = \frac{\pi}{6}$. We denote this position with an immersion angle α_i for each particle (13). For a given geometry and surface wettability (contact angle), the immersion angle α_i is only a function of the pressure difference across the AWI. By setting the derivatives of Eq. 2.2 calculated with respect to α_i equal to zero $\left(\frac{\partial \Delta P}{\partial \alpha_i}\right)\Big|_{\alpha_i=\alpha_i^{cr}} = 0$, one can obtain the critical capillary pressure (CCP) ΔP^{cr} and critical immersion angle α^{cr}. Note that α-values greater or smaller than 90° correspond to negative or positive CCPs, respectively. The bubble pressure P_{bub} can be obtained assuming that the entrapped air undergoes an isentropic compression,

$$P_{bub} = P_{\infty}\left(\frac{V_{\infty}}{V}\right)^{1.4} \tag{2.3}$$

where V_{∞} and V are the volume of the entrapped air at the zero hydrostatic pressure and at any P_h, respectively. Note that, $P_{bub}|_{P_h=0} = P_{\infty}$, and AWI has a flat profile which reaches equilibrium at a position $\alpha_{\infty} = \pi - \theta$ (as shown in Fig. 2.1a for particles having identical YLCAs). The volume of the trapped air can then be estimated as,

$$V_{\infty} = \frac{d}{2}[1-\cos\theta]L_s{}^2 - \left[\frac{\pi d^3}{6} - \pi\frac{\left(\frac{d}{2}+\frac{d}{2}cos\theta\right)^2}{3}\left(d-\frac{d}{2}cos\theta\right)\right] \tag{2.4}$$

Accurate calculation of V requires numerical values for the 3-D shape of the AWI. While such information can readily be obtained from the SE's numerical calculations, the above analytical derivation can only continue if this volume is approximated with a combination of some basic geometric volumes. Assuming that the volume under the actual (curved) AWI is the volume under a flat AWI minus the volume shown with gray color in Fig. 2.1d, we can develop an analytical expression to approximate the volume of the entrapped air as,

$$V = V_f - V_c = h{L_s}^2 - \frac{\pi}{3}h^2\left(\frac{3}{2}d - h\right) - \left(a_2 L_s^2 + \frac{\pi\, {a_3}^2}{3}(3R_2^* - a_3)\right) \tag{2.5}$$

where $V_f = h{L_s}^2 - \frac{\pi}{3}h^2\left(\frac{3}{2}d - h\right)$ and $V_c = a_2 L_s^2 + \frac{\pi\, {a_3}^2}{3}(3R_2^* - a_3)$ are the volume under the flat AWI and the volume of the gray-shaded region (the volume between a spherical cap with a radius of R_2^* placed at the center of the cell and a cuboids) in Fig. 2.1d, respectively. In these equations $a_2 = R_1^* - \sqrt{{R_1^*}^2 - {a_1}^2} = R_1^* - \sqrt{{R_1^*}^2 - (\frac{L_s}{2} - \frac{d}{2}\ sin\alpha)^2}$ and $a_3 = R_2^* - \sqrt{{R_2^*}^2 - (\frac{L_s\sqrt{2}}{2} - \frac{d\sqrt{2}}{2}\ sin\alpha)^2}$ where R_1^* and R_2^* are the principal radii of curvature of the AWI and are equal to $\frac{\sigma}{\Delta P}$ and $\frac{2\sigma}{\Delta P}$, respectively, according to the Laplace pressure equation (see Fig. 2.1d). The volumes of the above spherical cap and cuboids are $\frac{\pi}{3}{a_3}^2(3R_2^* - a_3)$ and $a_2 L_s^2$, respectively. Similar method will be used later for bi-component coatings and coatings with randomly arranged particles in Sec. 2.4. Substituting Eqs. 2.4 and 2.5 into Eq.2.3, one can obtain P_{bub} and consequently P_h. With α being available for all particles, one can then easily calculate a dimensionless wetted area A_w (assuming a planar contact line around the particles) as,

$$A_w = \frac{A_{SL}}{L_s^2} = \frac{\pi\, d^2}{2L_s^2}\sum_{i=1}^{4} n_i(1 - cos\alpha_i) \tag{2.6}$$

In Sec. 2.4, we present a comparison between the results for CHP and A_w calculated using our simple analytical expressions and SE.

2.3. Slip Length for Internal Flows

As mentioned earlier, reducing the friction drag is one of the most attractive properties of SHP surfaces. Drag reduction is often characterized in terms of slip length; the imaginary distance below the slip-generating surface at which the water velocity extrapolates to zero (60). The slip length on a SHP surface is related to A_w, and is therefore pressure dependent. While there are several studies proposing an explicit relationship between slip length and A_w for internal flows over SHP surface comprised of streamwise or transverse sharp-edged grooves (71,80–85). A relevant work to be used here in studying the slip length over granular SHP surfaces is that of Srinivasan et al. (1), who proposed an expression for the slip length over SHP monofilament woven screens in flow between two parallel plates:

$$b = \frac{L_s}{3\pi} ln\left(\frac{2(1+\sqrt{1-A_w})}{\pi\, A_w}\right) \tag{2.7}$$

Note that Eq. 2.7 was originally developed with the assumption that the woven screens have planar structures, i.e., A_w never exceeds 1. This assumption, however, is not accurate for granular coatings. Nevertheless, in the absence of a better alternative, we use this expression here as a means of discussing the effects of pressure on slip length, but only as long as $A_w \leq 1$. On a parallel track, Butt et al. (2) proposed an expression for slip length over an ordered array of spherical particles in a cylindrical capillary tube, as

$$b = \frac{{L_s}^2}{3\pi d f} \tag{2.8}$$

with $f = 0.5$ or 1 for when particles are half or completely wetted. This equation is derived simply on the basis of the Stokes drag on an isolated particle (i.e., Reynolds numbers near 1), which is obviously not the case when a coating is comprised of closely packed particles. Therefore, we modify this equation by replacing f with a more representative expression, and compared it with Eq. 2.7 (see the next section).

$$\frac{f}{{L_s}^2} = \frac{\frac{A_{sL}}{\pi\, d^2}}{{L_s}^2} = \frac{A_{sL}}{{L_s}^2}\frac{1}{\pi d^2} = \frac{A_w}{\pi d^2} \tag{2.9}$$

Substituting Eq. 2.9 in Eq. 2.8, we obtain

$$b = \frac{d}{3A_w} \tag{2.10}$$

Eqs. 2.7 and 2.10 will be later used in Sec. 2.4 to study the effects of hydrostatic pressure on slip length.

2.4. Results and Discussion

In this section, we study how granular coatings perform under different hydrostatic pressures. We combine and compare the results of analytical and numerical calculations, and discuss the effects of contact angle dissimilarity and particles' spatial distributions on the coatings' performance. Before we proceed to our results, we first studied the effects of mesh density on the accuracy of the SE simulations. We therefore, varied the interval size of the grid on the perimeter of the particles λ and monitored its effects on the resulting CHP and A_w. In our study, the SE results reached a state of mesh-independence at a mesh density of about $\frac{d}{\lambda} = 25$. For the numerical results presented here, a mesh density of $\frac{d}{\lambda}$ = 50 or greater was used.

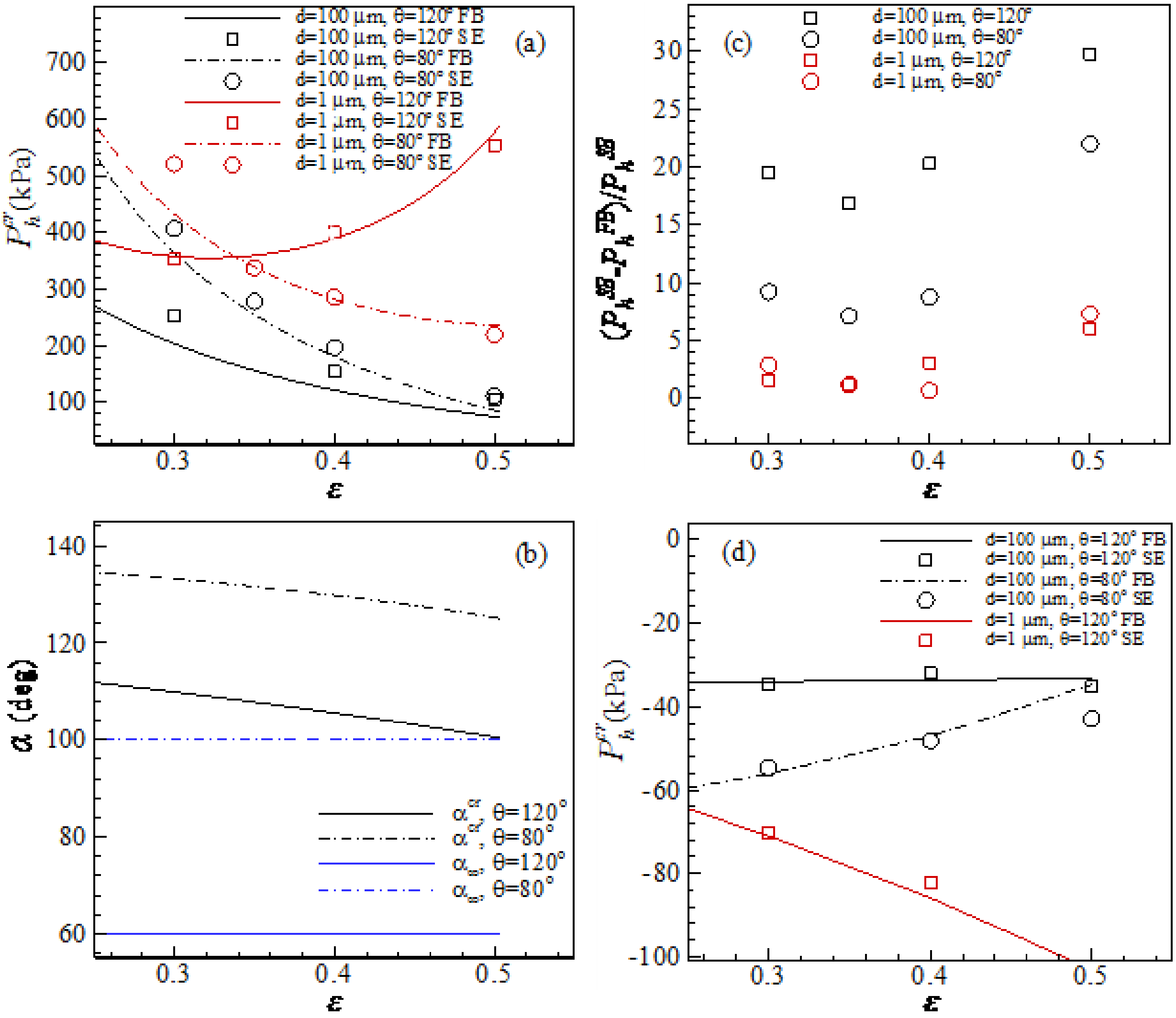

Fig. 2.2 CHP predictions, obtained from FB and SE calculations for COPDs comprised of particles with YLCAs of 80° and 120° and diameters of 100 µm and 1 µm, are shown in (a) along with their immersion angles from the FB method in (b). Percent relative error between the FB and SE calculations is given in (c) for coatings with different SVFs. The critical negative hydrostatic pressures are shown in (d) for the same COPDs.

2.4.1 Coatings with Uniform Wettability

A series of virtual coatings with ordered particle distribution (COPDs) having similar YLCAs but different SVFs are considered here. CHPs for these surfaces are predicted using the FB formulations, and are compared with those obtained from SE. For comparison, two very different diameters of 100 µm and 1 µm are considered with their SVFs ranging from 0.3 to 0.5. We also considered two arbitrary YLCA of 120° and 80°, as examples of highly and slightly hydrophobic materials, respectively. Figure 2.2a shows CHP vs. SVF. It can be seen from both the analytical and SE results that CHP first decreases with increasing SVF, and then increases for the small particles (i.e., 1 μm). For $d = 100$ μm on the other hand, CHP monotonically decreases. This behavior is due to the interplay between the capillary forces and the forces generated by the compressed air bubble (which vary with SVF and particle diameter). The capillary forces are proportional to the length of the three-phase contact line. By increasing SVF, the capillary pressure plays a greater role in balancing the hydrostatic pressure as the ratio of the three-phase contact line to the area of the AWI increases. Therefore, while α^{cr} is the same for particles of different diameters (see Eq. 2.2), the corresponding capillary pressure is greater for smaller particles. The compression forces, on the other hand, are proportional to the compression ratio of the entrapped air $C = \frac{V_\infty}{V}$, which being independent of particle diameter, is a function of immersion angle ratio $\frac{\alpha_\infty}{\alpha^{cr}}$. As can be seen in Fig. 2.2b, α^{cr} decreases as SVF increases, causing the compression ratio to decrease with increasing SVF. Therefore, increasing SVF decreases the resistance of the entrapped air in balancing P_h. Therefore, if capillary forces are small in comparison to the compression forces (for $d = 100$ μm), increasing SVF decreases CHP. However, when capillary forces are on the same order of magnitude of the compression forces, the increase in capillary forces at high SVFs may compensate for the decrease in the contribution of the compression forces ($d =$1 μm). To better examine the error associated with our approximate volume calculations (Sec. 2.2), we plotted the percent error for predictions obtained from our FB equation relative to those of SE in Fig. 2.2c. It can be seen that the results of our simple analytical FB method are in relatively good agreement with the more rigorous numerical calculation of the SE code, especially at lower SVFs (at high SVFs, the planar contact line assumption becomes less accurate). It is also worth mentioning that our SE calculations are in perfect agreement with those reported by Slobozhanin et al. (86) obtained for infiltration of water in closely packed spherical particles which coincide with the case of $\varepsilon_{max} = \frac{\pi}{6}$ in our simulation (the comparison is not shown for the sake of brevity).

Figure 2.2d shows CHP values of the coatings when the AWI is exposed to negative pressures, such as the condition caused by a flow-induced suction (Venturi effect), for instance. Here again, for coatings comprised of large particles, the bubble pressure plays the dominant role in balancing the negative hydrostatic pressure, while for surfaces with smaller particles, the capillary forces determine the critical suction pressure. Here the AWI shape is concave and the capillary force component is in the same direction as hydrostatic force ($\alpha^{cr} < \alpha_{\infty}$). Note that critical suction pressures below the water vapor pressure is unphysical and so not shown.

The SE and FB predictions of A_w for SHP surfaces comprised of particles with different diameters, YLCA, and SVFs are presented in Fig. 2.3a and 2.3b. These figures indicate that, other parameters being constant, A_w increases with P_h, although the increase is not monotonic. The increase in A_w is because of the AWI moving further down into the pore space between the particles as P_h increases. It can be seen in Fig. 2.3a that $A_w > 1$ for coatings with the smaller contact angle (i.e., $\theta = 60^{\mathrm{o}}$). Note in this figure that, despite the very different range of operating pressures for large and small particles, the range of variation of A_w is identical for both particle diameters. This is simply due to the fact that $\alpha^{cr}$is independent of particle diameter.The effects of P_h on dimensionless slip length for flow over a granular SHP surface inside a capillary tube (calculated using Eqs. 2.7 and Eq. 2.10) are shown in Fig. 2.3c. It can be seen that predictions of Eq. 2.7 and 2.10 are not in perfect agreement, as they were derived on the basis of two very different sets of physics (see Sec. 2.3). In the remainder of this chapter, we only use Eq. 2.7 but only as long as

$A_w < 1$. It can be seen that $\frac{b}{L_s}$ decreases with increasing P_h. Using Eq. 2.7 along with A_w from Fig. 2.3b, it can be expected that $\frac{b}{L_s}$ is smaller for coatings with higher SVFs at constant P_h.

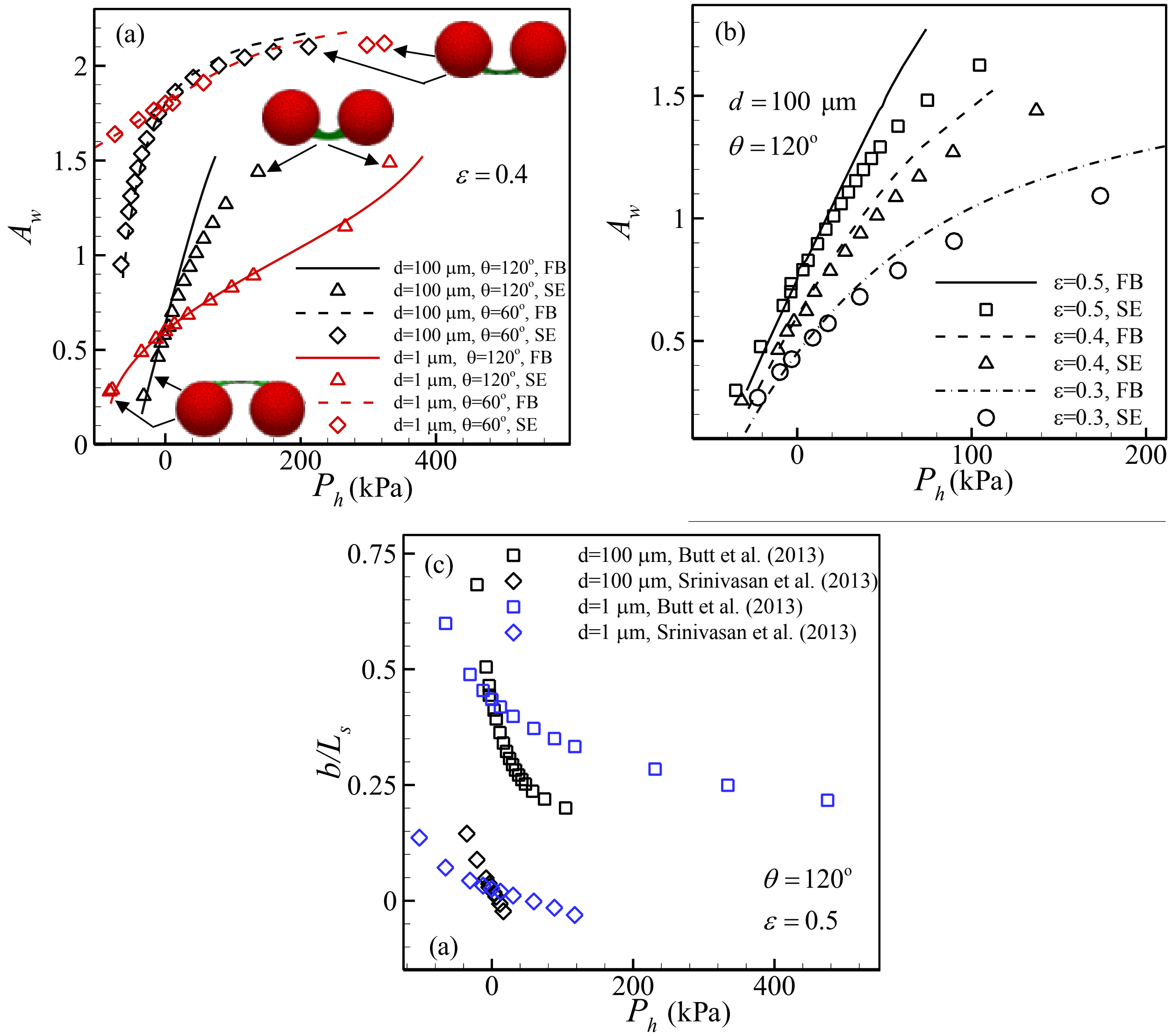

Fig. 2.3 Variations of wetted area with hydrostatic pressure obtained from FB and SE calculations for COPDs having a solid volume fraction of $\varepsilon = 0.4$, particle diameters of 100 μm and 1 μm, and YLCAs of 60° and 120° are shown in (a). The effects of SVF on wetted area is shown in (b) for the case of $\theta = 120^{\circ}$ and $d = 100$ μm. Estimations of the dimensionless slip length versus hydrostatic pressure obtained from the expressions of Refs. (1) and (2) for COPDs with $\theta = 120^{\circ}$ and $\varepsilon = 0.5$ in (c).

2.4.2 Coatings with Dissimilar Wettabilities: Equivalent Contact Angle

In this section, we consider bi-component coatings, i.e., coatings composed of particles with two different contact angles. Four different arrangements are considered for these four particles. Here we define n_1^c and $n_2^c = 1 - n_1^c$ to refer to the number fraction of particles with contact angles of $\theta_1 = 100^\circ$ and $\theta_2 = 120^\circ$, respectively. The case of $n_1^c = 0.5$ can have two different configurations in which particles of the same contact angles can be arranged in line or diagonal with respect to one another. Sample AWI profiles obtained from SE are shown in Fig. 2.4a for $n_1^c = 0.25$ and $n_1^c = 0.75$ with d =100 µm (note that the particle diameter does not affect the AWI profile). The two extreme conditions of $n_1^c = 0$ and $n_1^c = 1.00$ are also shown for comparison. Note that the equilibrium position of the AWI under both positive and negative CHP is lower when n_1^c is lower. The reason for this is that as n_1^c increases the coating becomes less hydrophobic. Also note that A_w increases with increasing n_1^c for the same reason.

Figure 2.4b shows A_w for bi-component coatings comprised of particles with YLCAs of $\theta_1 = 100^\circ$ and $\theta_2 = 120^\circ$ as a function of P_h. In this figure $d = 100$ µm and SVF of $\varepsilon = 0.4$. Obviously, increasing P_h increases A_w. More importantly, comparing coatings of different n_1^c shows that A_w increases with increasing n_1^c. This is due to the fact that water tends to penetrate deeper into the coating as n_1^c increases. Note that for $n_1^c = 0.5$, the choice of diagonal or in-line arrangement does not matter (see the offset of Fig. 2.4b) as the choice of particle configuration does not affect the net capillary pressure generated by the particles.

The other interesting, yet expected, result in this figure is that the maximum and minimum values of A_w are associated with the highest and lowest values of n_1^c, respectively. The slip length values corresponding to A_w of Fig. 2.4b are calculated using Eq. 2.7 and are shown in Fig. 4c. As expected, slip length is less for coatings with higher A_w.

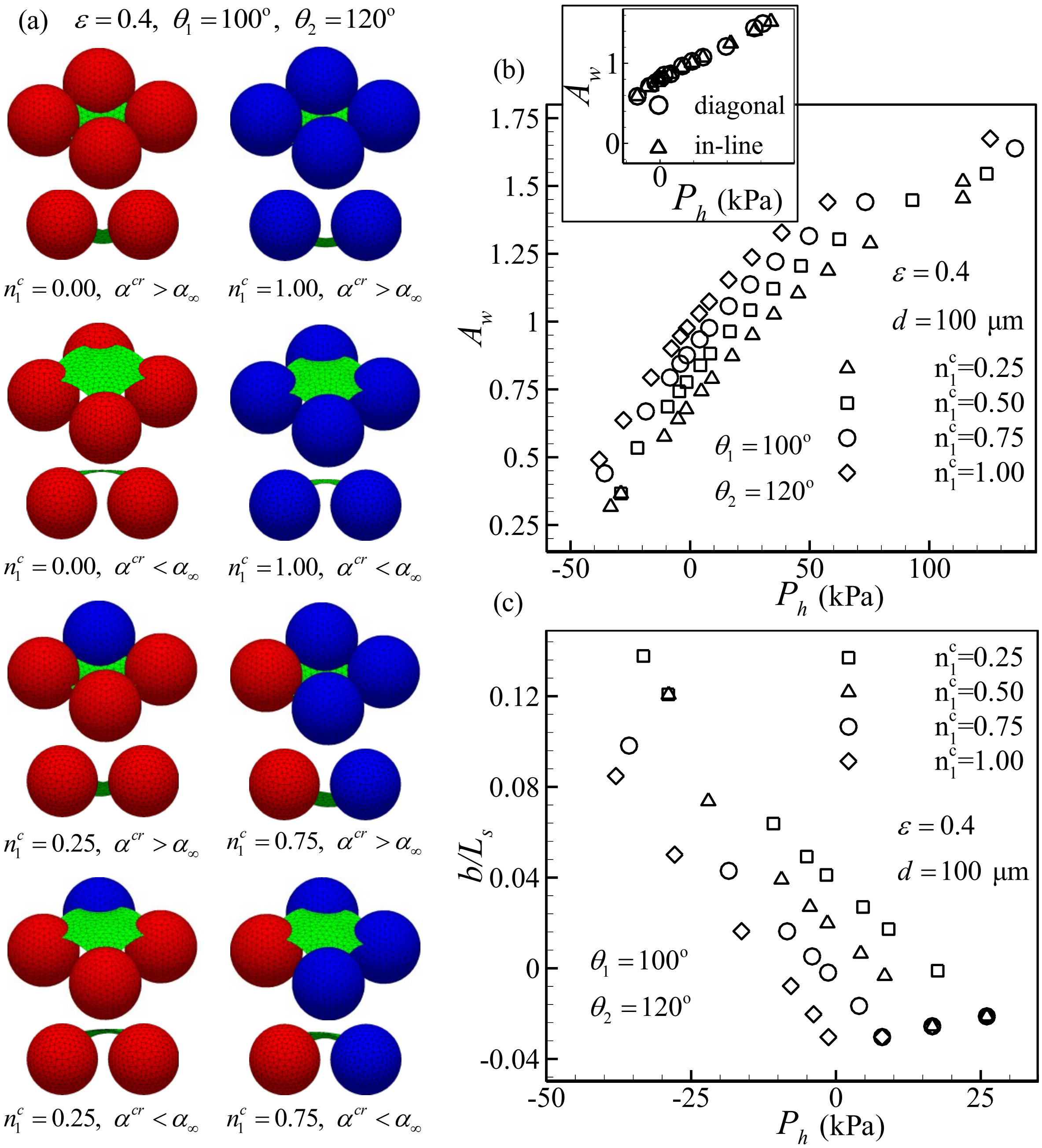

Fig. 2.4 Examples of the critical AWI for bi-component COPDs with different microstructural and wetting properties (given below each sub-figure) (a). Wetted area (b) and dimensionless slip length (c) as a function of hydrostatic pressure for COPDs with different population fractions of particles with $\theta_1 = 100^\circ$ and $\theta_2 = 120^\circ$ for an SVF of $\varepsilon = 0.4$ and a particle diameter of $d = 100$ μm.

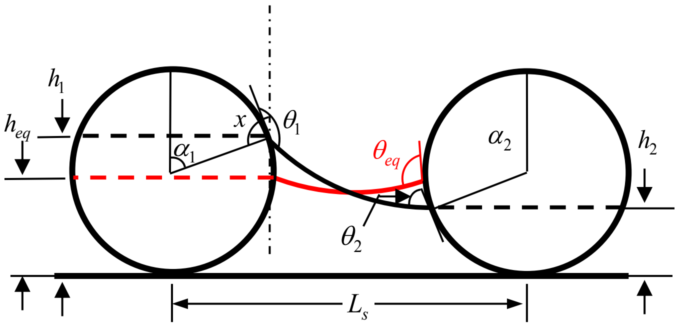

Fig. 2.5 The equivalent contact angle concept shown schematically with the relationship between the angles and directions.

The analytical formulations given in Sec. 2.2 can be used to produce predictions for the CCP, critical immersion angle, and critical wetted area for a bi-component coating. However, they need to be modified before they can be used to predict the CHP (or α_i and A_w for capillary pressures other than the CCP) for a coating comprised of particles with more than one contact angle. We therefore, defined an equivalent contact angle θ_{eq} to simplify the otherwise complicated calculations needed to estimate the volume of the entrapped air under the 3-D AWI. In order to calculate θ_{eq}, we define an equivalent height for the AWI as the weighted average of the AWI height at each particle $h_{eq} = n_1^c h_1 + n_2^c h_2$ where $h_1 = \frac{d}{2}(1 - cos\alpha_1)$ and $h_2 = \frac{d}{2}(1 - cos\alpha_2)$ as shown in Fig. 2.5. Therefore,

$$h_{eq} = \frac{d}{2}(1 - cos\alpha_{eq}) \tag{2.11}$$

Obviously, the equivalent AWI height corresponding to an equivalent immersion angle α_{eq} can be expressed as

$$cos\alpha_{eq} = n_1^c cos\alpha_1 + n_2^c cos\alpha_2 \tag{2.12}$$

α_{eq} is a function of $P_h$and is related to the angle between the vertical direction and the capillary force (x) as $\alpha(\Delta P) = \frac{3\pi}{2} - x(\Delta P) - \theta$ (see Fig. 2.5). For the special case of zero hydrostatic pressure, $x(\Delta P = 0) = \frac{\pi}{2}$and therefore $\alpha(\Delta P = 0) = \pi - \theta$. Rewriting Eq. 2.12, we obtain

$$cos\theta_{eq} = n_1^c cos\theta_1 + n_2^c cos\,\theta_2 \tag{2.13}$$

Equation 2.13 can be substituted into Eq. 2.2 for pressure calculation. Although Eq. 2.13 was derived using $\Delta P = 0$, this equation is valid for every P_h as the contact angle is a material property independent of operating pressure.

Figure 2.6a shows our CHP predictions for coatings comprised of particles having contact angles of $\theta_1 = 100^{\circ}$ and $\theta_2 = 120^{\circ}$ with different n_1^c. For these calculations, θ_{eq} (Eq. 2.13) was used to estimate the volume of the entrapped air. Predictions of the SE code are also added for comparison. Our results indicate that for coatings made of smaller particles ($d = 1$ µm), the CHP is higher when all particles have a higher contact angle, i.e., $n_1^c = 0$, when the coatings have an SVF of $\varepsilon >$ 0.3. Interestingly however, for coatings with an SVF of $\varepsilon < 0.3$, the trend is reversed. A similar effect is also observed for the coatings with the larger particles ($d = 100$ µm), but with the transition SVF moved to about $\varepsilon = 0.3$. For the larger particles however, the dependence of the CHP on particle's hydrophobicity is negligible for $\varepsilon > 0.4$ (see also Fig. 2.2 for the effects of particle diameter on CHP). Figure 2.6b shows similar results for when the AWI is exposed to negative pressures. Note again that the negative critical pressures are limited to the vapor pressure of water in this figure. Figures 2.6a and 2.6b both indicate that our simple FB analytical formulations can produce predictions in reasonable agreement with the significantly more rigorous calculations of the SE code.

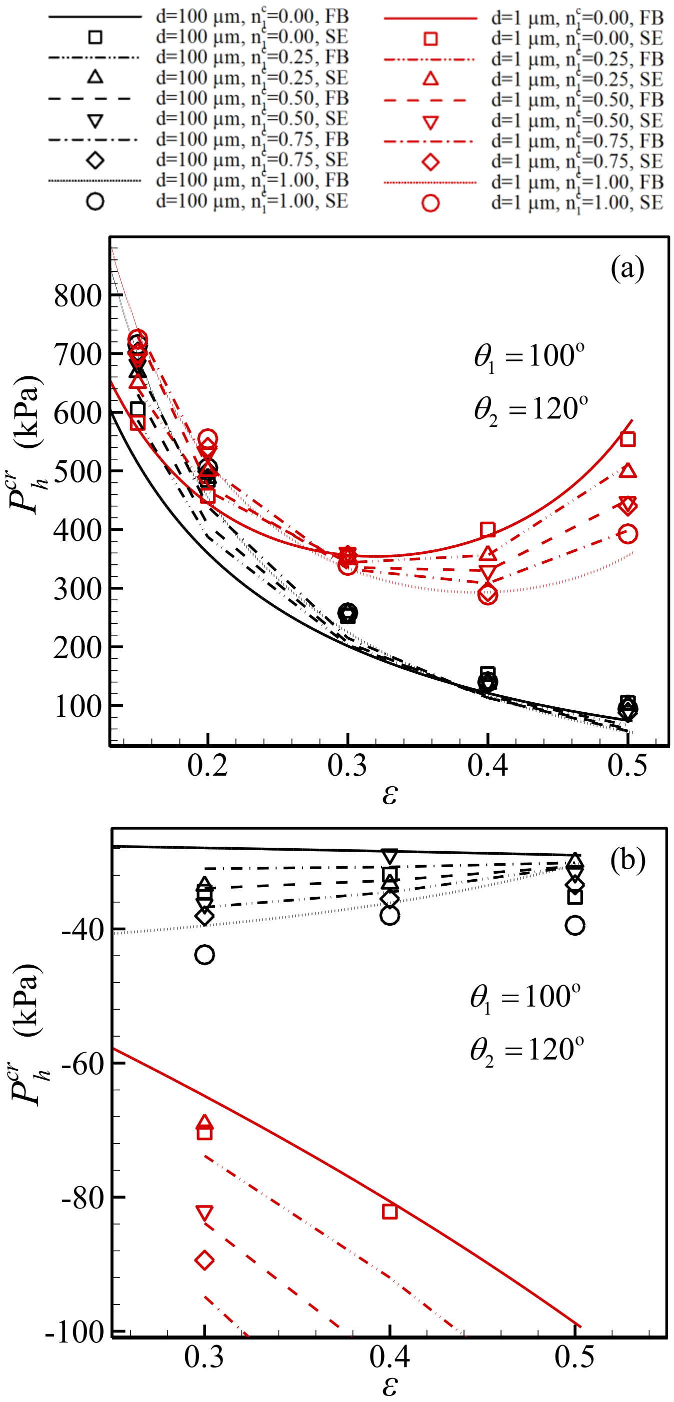

Fig. 2.6 CHP predictions, obtained from FB and SE calculations for bi-component COPDs comprised of particles with $\theta_1 = 100^\circ$ and $\theta_2 = 120^\circ$ and diameters of $d = 100$ μm and $d = 1$ μm. (a) and (b) show the case with positive and negative pressures, respectively.

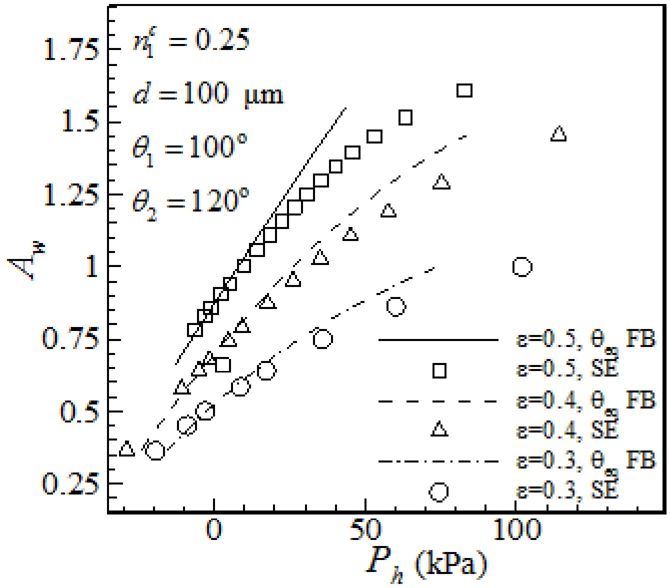

Fig. 2.7 Variations of wetted area with hydrostatic pressure obtained from FB and SE calculations for COPDs having $\theta_1 = 100^{\text{o}}$, $\theta_2 = 120^{\text{o}}$ with $d = 100$ μm for $n_1^c = 0.25$.

Figure 2.7 shows A_w versus P_h for $n_1^c = 0.25$ obtained from both the FB formulations and SE. Good general agreement between the two methods is evident. Similar behavior but slightly higher in magnitude is observed for $n_1^c = 0.50$ and $n_1^c = 0.75$ but not shown for the sake of brevity. One can also estimate the slip length for the flow over a granular SHP surface under different P_h (using Eq. 2.7 or any other relevant explicit expression) without needing to run a numerical calculation (results not shown but are similar to Fig. 2.4c).

2.4.3 Randomly Distributed Particles

In this section, we discuss the effects of randomness in the spatial distribution of the particles. We consider $d = 1$ μm and $d = 100$ μm with YLCA equals 120^{o}. The virtual coatings with random particle distributions (CRPDs) were generated via an in-house MATLAB code. In generating these virtual coatings, we enforced a minimum particle-to-particle distance of $d/8$ to prevent the formation of pendular rings and to also ease the subsequent meshing process in SE.

We chose a simulation domain eight times greater than the particle diameter in length and width with periodic boundaries. The simulation size was found to be large enough to reduce the statistical uncertainty of the results without requiring excessive CPU time. We produced a Voronoi diagram for each CRPD to produce the input data files needed for SE simulations (see Fig. 2.8a). These data files contain information about the AWI geometry described in a descretized form comprised of vertices, edges, and faces. To generate the information, we first placed vertices around the perimeter of each particle in the domain, and then produced a list of neighbors for each particle in the coating using Voronoi diagram. We then connected the vertices to make edges between the neighboring particles, and finally produced faces from these edges. To calculate CHP in these simulations, the pressure was incrementally increased until α_i reached α^{cr} for one of the particles in the coating, or until the AWI touched the bottom of the pore space between the particles. For the range of SVFs considered in this chapter, the former has been observed to be the failure mode, although the latter is expected to be the sole cause of failure at very low SVFs. Note that for CRPDs, one should distinguish between local failure and overall failure. The former is failure at some specific locations in the coating with perhaps a low local particle number density and used in this work to define the CHP, while the latter is failure at all points in the coating (26).

Figure 2.8b shows the AWI over a coating with $d = 100$ µm, $\theta = 120^{\circ}$, and $\varepsilon = 0.25$ under $P_h = 169.4$ kPa ($\Delta P = 0.86$ kPa). Figure 2.8c shows the AWI under a negative CHP of $P_h = -40.36$ kPa ($\Delta P = -0.30$ kPa) for the exact same virtual coating. Note that the three-phase contact-line around the particles is smaller in Fig. 2.8c when compared to that of Fig. 2.8b. This is because the AWI in Fig. 2.8c is farther away from the equator of the particles. This can be seen more clearly in Figs. 2.8d and 2.8e where contour plots of the AWI height are shown (the numeric values corresponding to the colors are presented in the color bar).

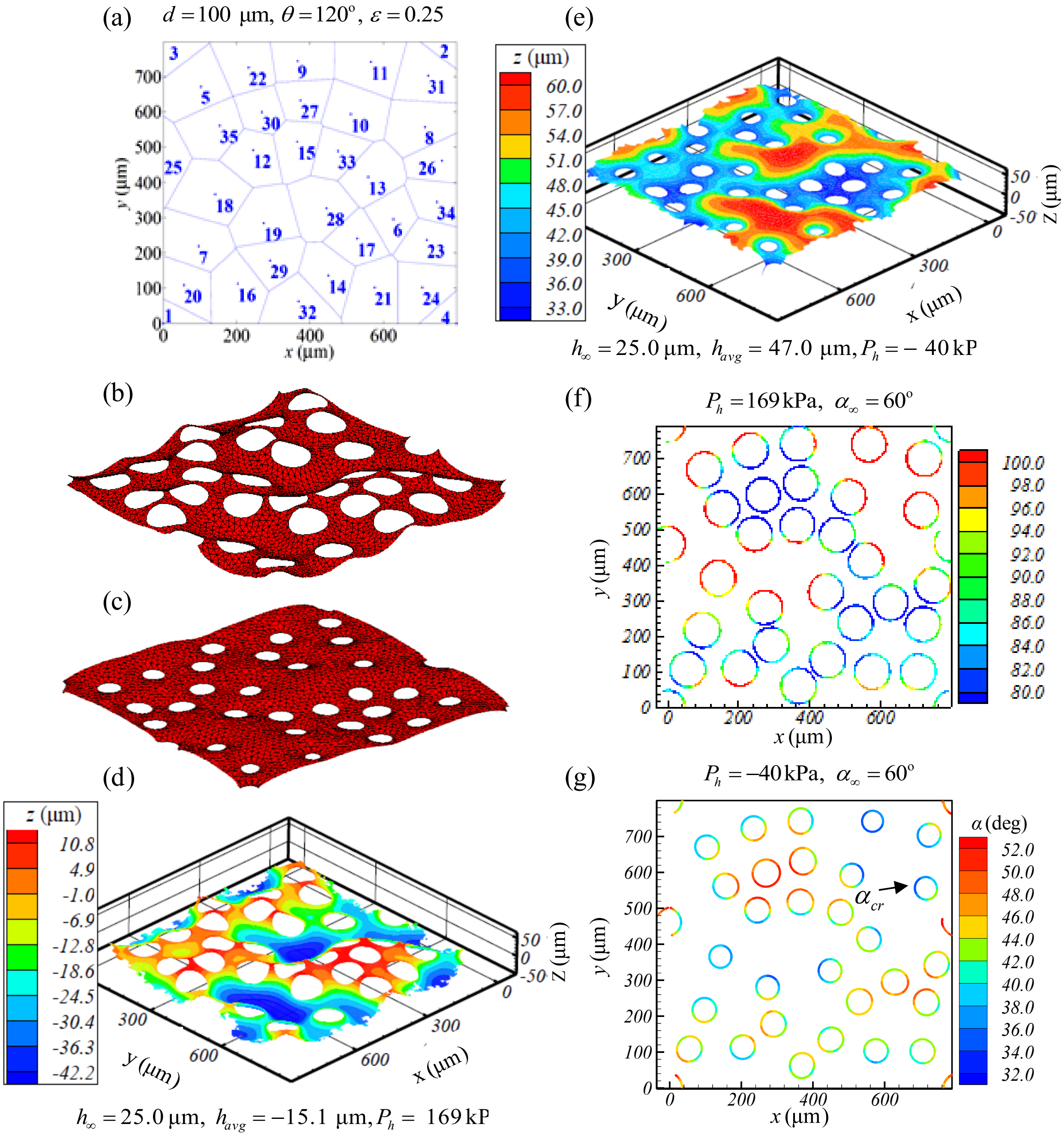

Fig. 2.8 An example Voronoi diagram produced for a CRPD with an SVF of $\varepsilon = 0.25$ comprised of 34 particles is shown in (a). The AWI for the case of particles with a YLCA of $\theta = 120^{\circ}$ at positive and negative CHPs of $P_h = 169$ kPa and $P_h = -40$ kPa are shown in (b) and (c) along with their height contour plots in (d) and (e) $P_h = -40$ kPa, respectively. The corresponding critical immersion angles are plotted for each particle and shown in (f) and (g). Note the location of the failure point shown with an arrow in (f) and (g).

It can be seen that in regions where the distances between the particles is larger, the AWI height is low (high), for the positive (negative) CHP. Note in Fig. 2.8d that nowhere in the domain does the AWI contact the bottom surface (i.e., the minimum AWI height is greater than -50 µm). Also, note in Fig. 2.8e that the maximum AWI height is greater than particle radius (50 µm from center). Figures 2.8f and 2.8g show α_i of the particles in the coating under the above-mentioned CHPs (note the numeric values corresponding to the colors in the color). The α^{cr} corresponding to CHP values also reported in the figures. We again used Voronoi diagrams in the FB method for CHP prediction (referred to here as FB–Voronoi method). In particular, the Voronoi diagram is used to locate the weakest point in a coating; the Voronoi cell with the largest area (corresponding to the lowest local SVF). That area is then used to construct a square unit-cell with the same surface area L_s^2 to be used in Eq. 2.2 to predict the CCP (as well as α^{cr}) for the whole coating. Predicted CCP is then used to obtain the CHP for the coating after incorporating the compression pressure of the entrapped air (see Sec. 2.2). Fortunately, the latter is a straightforward calculation as the pressure of the entrapped air is not specific to any Voronoi cell, i.e., it is the same for all cells in the domain. Therefore, the compression ratio for the CRPD can be approximated (using the same formulations given in Sec. 2.2) with that of a COPD having the same overall SVF under the above-mentioned CCP (note that this pressure, CCP of the CRPD, should not be confused with the CCP of the COPD).

Figure 2.9a shows CHP for CRPDs in comparison to their ordered counterparts. In this figure, the predictions of SE are also included for comparison. To decrease the statistical uncertainty of the results obtained for the CRPDs, each case was repeated at least three times. It can be seen that, for both particle diameters, CHP decreases with SVF for $0 < \varepsilon < 0.3$. The decrease is sharp for

COPDs and slow for CRPDs (note that when $d = 1$ μm and $0.3 < \varepsilon$, CHP increases with increasing SVF as has been shown and discussed in Fig. 2.2).

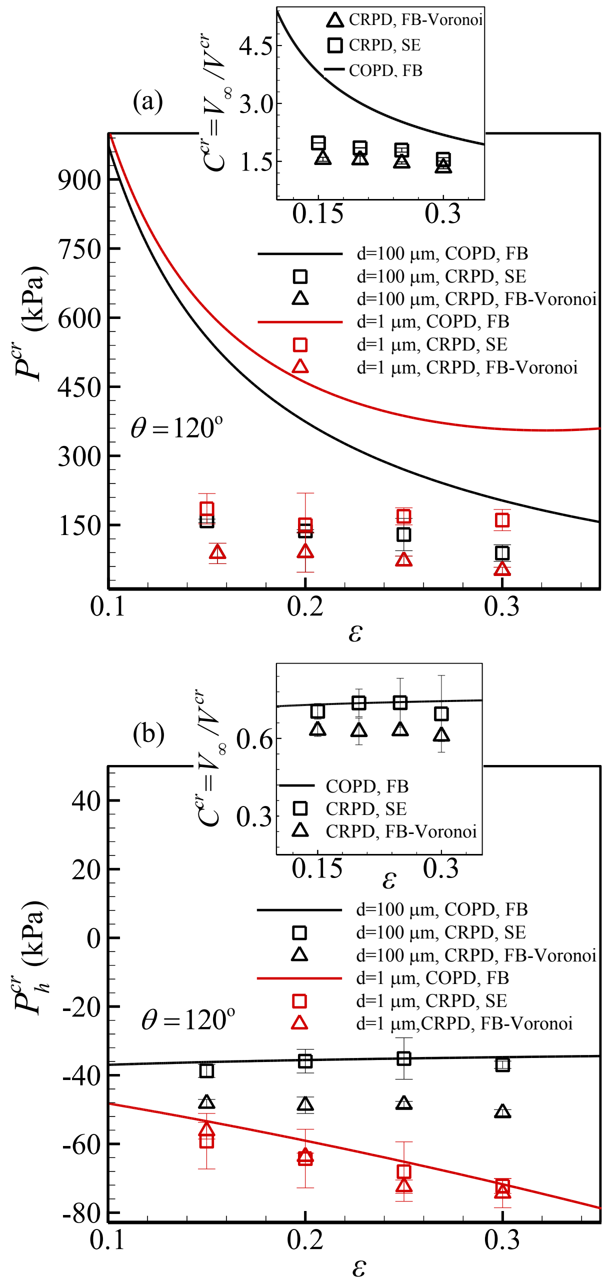

Fig. 2.9 CHP predictions, obtained from FB and SE calculations for CRPDs and their ordered counterparts are shown in (a) and (b) for positive and negative pressures, respectively, along with their corresponding bubble volume ratios in the offset.

Figure 2.9a shows a striking difference between CHPs obtained for CRPDs and their ordered counterparts (COPDs). The reason for this is that in response to an increasing pressure, α_i can rapidly increase to reach α^{cr} in certain regions of a CRPD (where local SVFs is low) resulting in a relatively low CCP for the coating. A low CCP consequently results in a less overall AWI deflection, i.e., a lower compression ratio for the entrapped air and so a lower CHP for CRPDs. The inset in Fig. 2.9a shows the critical compression ratio $C^{cr} = \frac{V_\infty}{V^{cr}}$ for CRPD and COPD at their corresponding CHPs, supporting the above argument. Note that these results are shown only for one particle size as they are independent of particle diameter (same as α^{cr}, Sec. 2.4.1). Figure 2.9b shows negative CHPs for the above coatings. Interestingly, here CRPDs and COPDs have almost identical CHPs. This is only because the compression ratios are about the same for both cases. Also, note that for coatings with larger diameters, the critical suction pressure is almost independent of SVF, while for the coatings made of smaller particles, the balance of capillary and bubble pressure leads to a decrease in the critical suction pressure with SVF as discussed earlier for the results shown in Fig. 2.2d. Figure 2.9 indicates that predictions of FB–Voronoi method are in good relative agreement with the results of SE for CRPDs, while being significantly simpler.

For completeness of the study, we also considered coatings comprised of particles with two different YLCAs ($\theta_1 = 100^{\circ}$ and $\theta_2 = 120^{\circ}$) distributed randomly over the surface with an almost equal population ($n_1^c \cong 0.5$). Figure 2.10a shows the SE and FB–Voronoi predictions of CHP for such bi-component CRPDs. It can be seen that CHP generally decreases with increasing SVF, which is in agreement with the results of Fig. 2.6a for $0 < \varepsilon < 0.3$. For the analytical calculations, we used the equivalent contact-angle concept of Eq. 2.12 to extend the utility of our

FB–Voronoi method to CRPDs of dissimilar YLCA. The difference between CRPDs and their ordered counterparts is similar to those discussed for Fig. 2.9 and so is not repeated here (see Fig. 2.6 for CHP values given for COPD).

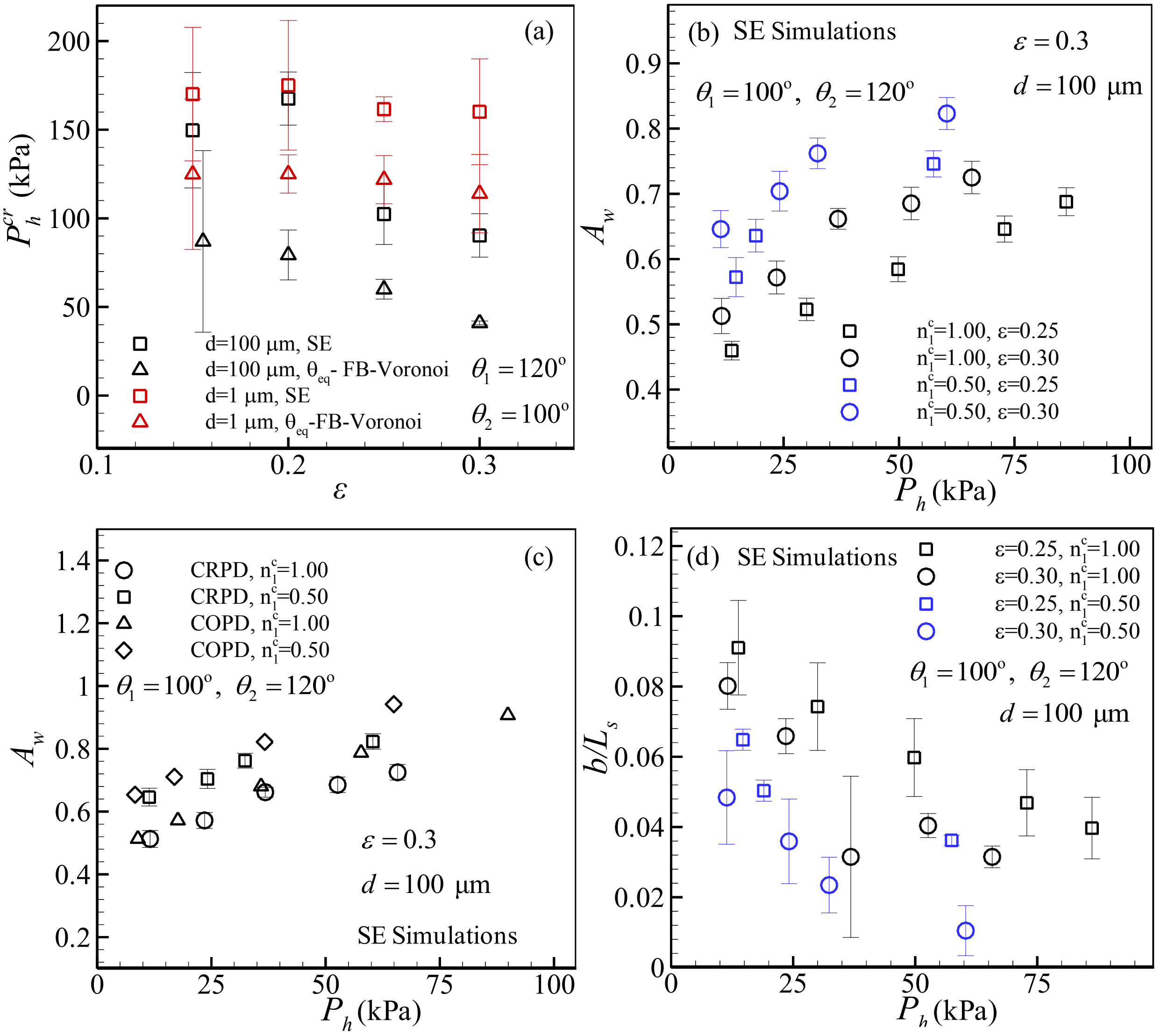

Fig. 2.10 CHP predictions vs. SVF, obtained from FB and SE calculations for bi-component CRPDs having $\theta_1 = 100^o$ and $\theta_2 = 120^o$ with population fractions of $n_1^c \cong 0.5$, are given in (a). Wetted area as a function of hydrostatic pressure obtained using from SE for CRPDs is shown in (b). Wetted area for CRPDs and their ordered counterparts are given in (c). Dimensionless slip length as a function of hydrostatic pressure for CRPDs having $\theta = 120^o$ and bi-component CRPDs having $\theta_1 = 100^o$, $\theta_2 = 120^o$ and $n_1^c \cong 0.5$ are presented in (d).

Figure 2.10b shows A_w versus P_h for bi-component CRPDs with $d = 100$ μm and two different SVFs ($\varepsilon = 0.25$ and 0.3), obtained from SE and FB–Voronoi method. Similar to the case of COPD, A_w increases with P_h raise. It can also be seen that for a constant P_h, the wetted area increases with SVF due to the increase in the number of particles in the coating. In Fig. 2.10c A_w is shown as a function of P_h, for CRPDs and their corresponding COPDs to investigate the effect of the distribution of the particles on A_w (and so perhaps on $\frac{b}{L_s}$). It can be seen that at a given P_h the distribution of the particles in a coating does not affect A_w (only the SE results are shown for the clarity of the presentation). $\frac{b}{L_s}$ for CRPDs follows a trend similar to COPDs (Fig. 2.4b), i.e., it decreases with increasing P_h (see Fig. 2.10d).

2.5. Conclusions

A The skin-friction drag on a submerged object is related to the area of contact between the solid surface of the object and water—the wetted area of the surface. Properly designed SHP coatings can reduce the area of contact between water and solid surface. Although, the relationship between the wetted area and drag-reduction is complicated and reducing the wetted area does not necessarily guarantee a reduction in the drag force, the ability to predict the wetted area of a surface allows one to better engineer the microstructure of SHP surfaces. In regard, we have developed a force balance analytical method to predict the stability (CHP) and wetted area of a SHP surface made of a single layer of ordered or randomly distributed particles of dissimilar wettabilities. Our simple analytical method was benchmarked using more accurate calculations of the SE code and reasonable agreement was observed.

Our results indicate that CHP of COPDs made of hydrophobic large particles (e.g., 100 μm) decreases with SVF but shows a U-shaped behavior if the particles are smaller (e.g., 1 μm). Our results also revealed that, depending on SVF and contact angle, dimensionless wetted area can exceed 1 at hydrostatic pressures much smaller than the CHP of the surface. Such quantitative information is very relevant in designing a SHP coating for a given application. Similar results but with greater or smaller magnitude were also obtained for CRPDs and coatings comprised of particles with different YLCAs under positive or negative hydrostatic pressures, and discussed in detail. More specifically, it was observed that CHP of CRPDs can be much smaller than that of their ordered counterparts (COPDs) because of the heterogeneity in the particle distribution allowing for regions with low local SVF to fail rather quickly under elevated pressures. It was also found that, at a given hydrostatic pressure, randomness in the distribution of the particles does not affect the wetted area.

Chapter 3. Effects of Hydrostatic Pressure on Wetted Area of Submerged polydispersed Superhydrophobic Granular Coatings

3.1 Introduction

The reduced cost of manufacturing has played an important role in making spray-on granular superhydrophobic coatings attractive alternatives to superhydrophobic surfaces produced via microfabrication (see e.g., (87–89)). Such surfaces can be used for applications ranging from self-cleaning and drag reduction to corrosion resistance and heat transfer (12,22,60,90). The essential attribute of superhydrophobic (SHP) surfaces is the reduced water–solid contact area (wetted area), which helps to reduce the friction between a moving body of water and the surface (12,14,15,60). An analytical force balance method to approximate the wetted area of a SHP surface comprised of particles of equal size but different Young–Laplace contact angles (YLCAs) was presented in the first part of this two-part publication (chapter 2 of this dissertation) (35). In current chapter, we extend our formulations to the most general case of SHP coatings made up of particles of different diameters and YLCAs. As in Chapter 2, the instantaneous shape and position of the air–water interface (AWI) between the particles is also used to predict the effective slip length of the surface, when used in a microchannel for instance. An introductory discussion along with a thorough literature review is given in Chapter 2 to put this study in the proper context of prior studies, and so it will not be repeated here (see (11,13,24,73,76,77,80,81) for additional information). Here we present a condensed overview of the background information needed for the continuity of our discussion.

The shape and position of the AWI over a SHP surface may be explained using the balance of the forces that act on the interface. For a submerged SHP surface, these forces are due to hydrostatic pressure P_h, ambient pressure P_∞, pressure of the air trapped in the pore, referred to here as the bubble pressure P_{bub}, and the pores' capillary pressure P_{cap}. The bubble and capillary pressures, if positive, tend to balance the hydrostatic pressure (35). A submerged SHP surface may not always be in the Cassie state (fully-dry); depending on the hydrostatic pressure and the surface morphology, the surface may move to the Wenzel state (fully-wetted) or to a transition state between the two extreme states (63,67,71,91). There are two main paths by which a submerged SHP surface may reach a transition state: a gradual transition from the Cassie state over a certain period of time under a moderate hydrostatic pressure, or a sudden transition upon exposure to an elevated pressure. The former takes place due to the dissolution of the entrapped air in the ambient water, whereas the latter occurs because of the imbalance of the mechanical forces acting on the air–water interface (63,67,71,73,76,77,91). Therefore, the drag-reduction effect generated by a SHP surface varies depending on both the operating pressure and the time in service. The hydrostatic pressure at which a SHP surface starts departing from the Cassie state (where the capillary pressure is at its highest value) is referred to as the critical hydrostatic pressure (CHP) (16,34,63) for a SHP surface with sharp-edged pores/grooves. We assume the CHP for a pore with round entrance to be the hydrostatic pressure at which the AWI reaches the maximum capillary pressure, unless the AWI deflects enough to touch the bottom of the pore at a lower pressure (92). In that case, the latter pressure will be considered as the CHP.

In the following section, we first start with a force balance (FB) formulation for an AWI formed between the particles of a submerged granular SHP coating. This is followed by a simple method to relate the hydrostatic pressure of water above the surface to the capillary pressure of the coating's pores in Sec. 3.2.2. In Sec. 3.2.3, we propose mono-dispersed equivalent diameter definitions for bi-dispersed and poly-dispersed coatings to be used for critical capillary pressure (CCP) and wetted area predictions. Comparison between the predictions of our analytical method and those from the numerical simulations carried out using the Surface Evolver (SE) finite element code are given in Sec. 3.3. This section also contains detailed analyses for the effects of randomness in the spatial distribution of the particles, amongst many other parameters, in a poly-dispersed SHP coating. The condensed summary of the calculation procedure developed in our work is given in Sec. 3.4 in the form of a flowchart. The conclusions drawn from the work are given in Sec. 3.5.

3.2 Analytical Formulation

3.2.1 Critical Capillary Pressure

Consider an idealized condition for a single-layer bi-dispersed granular coating in which the particles with identical YLCAs are arranged in a square pattern as shown in Fig. 3.1a. Predicting the critical pressure and wetted area for the AWI over such coatings is a challenge, as it requires detailed information about the 3-D shape of the AWI. More specifically, one needs to keep track of both the instantaneous direction and the magnitude of the capillary force $F_{\sigma i} = \sigma \pi d_i sin\alpha_i$ as the AWI adjusts itself in the pore space between the particles. Obviously, the problem becomes even more complicated when the particles are distributed randomly. In this chapter, the SE code is used to numerically obtain the 3-D shape of the AWI as a function of pressure (see (38,39) for more information about SE). Figure 3.1a shows an example of such numerical calculations conducted for a coating with $d_1 = 100$ μm, $d_2 = 57$ μm, $\varepsilon = 0.3$, and $\theta = 120^{\mathrm{o}}$ at a capillary pressure of $\Delta P = 0.50$ kPa. One can easily calculate the wetted area of a coating once the 3-D shape of the AWI is available. Writing the balance of forces acting on an AWI in the vertical direction for a positive ΔP (in the negative z-direction), we obtain (13,24)

$$\Delta P\left(L^2 - \sum_{i=1}^{2} n_i \frac{\pi d_i^2}{4} sin^2\alpha_i\right) = \sum_{i=1}^{2} n_i \pi\sigma d_i sin\alpha_i cos\left(\frac{3\pi}{2} - \theta - \alpha_i\right) \tag{3.1}$$

where n_i is the number fraction of the particles with the diameter d_i.

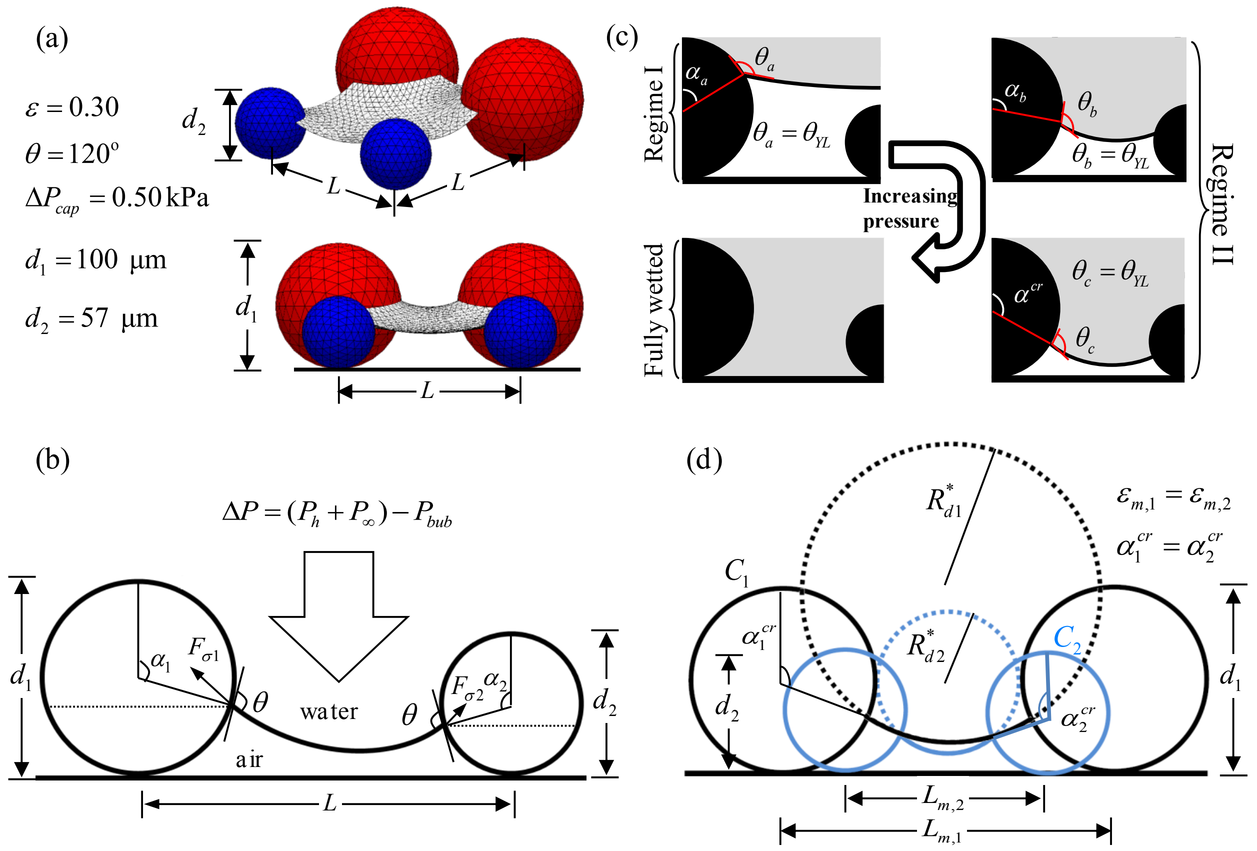

Fig. 3.1 (a): an AWI example over a bi-dispersed coating obtained using the SE code; (b): a 2-D diagram showing an AWI between two particles; (c): a schematic representation of AWI over a bi-dispersed coating under different hydrostatic pressures; and (d): 2-D representation of two mono-dispersed coatings with identical SVF but different particle diameters overlaid on top of one another.

We denote the average vertical position of the contact line around a particle in a granular coating with an immersion angle (IA) α_i for each particle (see Fig. 3.1b). The main simplifying assumption in deriving Eq. (3.1) is that the contact line between the AWI and the particles (shown with dotted line in Fig. 3.1b) remains in a horizontal plane. We expect the error associated with this assumption to be generally negligible, but it may become considerable if the solid volume fraction (SVF) is so high that the particles touch one another. For a single-layer bi-dispersed coating, we define SVF as $\varepsilon_b = \frac{\pi}{6}\frac{\sum_{i=1}^{2} n_i d_i^3}{L_b^2 d_c}$ where d_c is the diameter of the coarse particles (similarly $\varepsilon_p = \frac{\pi}{6}\frac{\sum_{i=1}^{4} n_i d_i^3}{L^2 d_c}$ for our poly-dispersed coatings as will be seen later in this chapter). By setting the derivative of Eq. (3.1) with respect to α_i equal to zero, $\left(\frac{\partial \Delta P}{\partial \alpha_i}\right)\Big|_{\alpha_i=\alpha_i^{cr}} = 0$, one can obtain the maximum (i.e., critical) pressure difference ΔP^{cr} and consequently, the CHP of the coating. Note that the values of α smaller or greater than 90° correspond to negative or positive critical pressure differences, respectively.

Equation (3.1) can be used for both a mono-dispersed and bi-dispersed (or poly-dispersed) coating, as long as the AWI is in contact with all of the particles. However, it is not impossible for an AWI over a bi-dispersed (or poly-dispersed) coating to reach an equilibrium position without coming into contact with the smaller particles when the hydrostatic pressure is low. In such conditions, the AWI may move down into the void between the coarse particles to reach the smaller particles if the hydrostatic pressure is increased (see Fig 3.1c). To better formulate the behavior of bi-dispersed coatings under pressure, we define two different pressure regimes, referred to here as Regime I and Regime II. Regime I is when the hydrostatic pressure is so low that the AWI wets the coarse particles only. Regime II, on the other hand, describes the range of pressures at which the AWI is in contact with both the coarse and fine particles. Note that as the hydrostatic pressure increases, some fine particles may come into contact with the AWI sooner than others, depending on their relative population in a coating. Regime II, therefore, starts when at least one fine particle comes into contact with the AWI. Excessive hydrostatic pressures can lead to failure (wetting) either due to the AWI sagging deep enough to touch the substrate or becoming mechanically unstable. Equation (3.1) can be rearranged for a mono-dispersed coating at its CCP to read as

$$\Delta P_m^{cr} = \frac{4\, sin\alpha^{cr}\; cos\left(\frac{3\pi}{2} - \theta - \alpha^{cr}\right)}{d\left[\frac{2}{6\varepsilon_m} - sin^2\alpha^{cr}\right]} \tag{3.2}$$

where $\varepsilon_m = \frac{\pi}{6}(\frac{d}{L_m})^2$ is the SVF of the mono-dispersed coating. As mentioned in Chapter 2, for mono-dispersed coatings with constant YLCAs, the critical IA, α^{cr}, is independent of particle size (depends only on the SVF) (35). Equation (3.2) also shows that at a constant SVF, capillary pressure is inversely proportional to d. Therefore, capillary pressure increases with decreasing particle size. The inverse relationship between the particle size and capillary pressure at a constant SVF can also be explained in terms of the AWI radii of curvature. Figure 3.1d shows the critical AWI over two mono-dispersed coatings with a constant SVF of $\varepsilon_{m,1}$=$\varepsilon_{m,2}$ but different particle diameters d_1 and d_2. As can be seen in Fig. 3.1d, the AWI over the coating with smaller particles has a smaller radius of curvature and consequently, a higher CCP ($\Delta P_{m,1}^{cr} = \frac{\sigma}{R_{d1}^*} < \Delta P_{m,2}^{cr} = \frac{\sigma}{R_{d2}^*}$) even though $\alpha_1^{cr} = \alpha_2^{cr}$. We use this to predict the CCP of bi-dispersed coatings in the next sections.

3.2.2 Hydrostatic Pressure

As explained before, the forces acting on an AWI are due to hydrostatic pressure, ambient pressure, bubble pressure, and the capillary pressure. Therefore,

$$P_{cap} + P_{bub} = P_{\infty} + P_h \tag{3.3}$$

One can obtain the CCP and α^{cr} using Eq. (3.1). The bubble pressure, on the other hand, should be obtained separately, assuming that the entrapped air undergoes an isentropic compression as the AWI penetrates into the pore, i.e.,

$$P_{bub} = P_{\infty} \left(\frac{V_{\infty}}{V}\right)^{\gamma} \tag{3.4}$$

where V_{∞} and V are the volumes of the entrapped air at a hydrostatic pressure of zero ($P_{bub}|_{p_h=0} = P_{\infty}$) and at any arbitrary pressure of P_h, respectively, and γ is the ratio of the specific heats. The air volumes V_{∞} and V can be obtained numerically (using the SE code as will be shown later in Sec. 3.3) or approximated analytically, the way we described in Chapter 2 (35). With volumes V_{∞} and V substituted into Eqs. (3.4) and (3.3), one can obtain the bubble and hydrostatic pressures using the capillary pressure information for a mono-dispersed coating. One can also calculate a dimensionless wetted area A_w (assuming a planar contact line around the particles) knowing the IA,

$$A_w = \frac{A_{SL}}{L^2} = \frac{\pi\, d_i^2}{2L^2} \sum_{i=1}^{2} n_i (1 - cos\alpha_i) \tag{3.5}$$

In Sec. 3.3, we present a comparison between our CHP and wetted area predictions using our simple analytical expressions and those obtained from numerical simulations conducted using SE.

3.2.3 Mono-Dispersed Equivalent Coating of a Bi-Dispersed Coating

Consider a unit cell of a bi-dispersed coating as shown in Fig. 3.2a. The red and blue colors represent coarse and fine particles, respectively, and the parameter n_i denotes the number fraction of particles with diameter d_i. Here, we present a simple method to predict the capillary pressure of such coatings using the analytical formulations developed originally for mono-dispersed coatings. For the sake of simplicity, we discuss the concept of equivalent mono-dispersed coating using a 2-D cross-section of the unit cell. Consider a system of two particles supporting an AWI as shown in Fig. 3.2b (e.g., a bi-dispersed coating with $n_1 = 0.5$). We define the mono-dispersed equivalent of this bi-dispersed system to be a system with the same capillary pressure (i.e., the mono-dispersed system that supports an AWI with the same radius of curvature). Assume the CCP for a mono-dispersed coating with a SVF of $\varepsilon_{m,1}$ comprised of particles with a diameter of d_1 to be $\Delta P_{m,1}^{cr}$. Using Eq. 3.2, one can find another mono-dispersed coating comprised of particles with a diameter of d_2 that has the same CCP, i.e., $\Delta P_{m,1}^{cr} = \Delta P_{m,2}^{cr}$. The second coating however, will have a different SVF $\varepsilon_{m,2}$ that can be obtained iteratively. Now consider a bi-dispersed coating comprised of particles with diameters d_1 and d_2. In a similar fashion, one can find the SVF ε_b of the bi-dispersed coating that provides the same CCP, i.e.,

$$\Delta P_{m,1}^{cr} = \Delta P_{m,2}^{cr} = \Delta P_b^{cr} \tag{3.6}$$

Recall that SVFs $\varepsilon_{m,1}$, $\varepsilon_{m,2}$, and ε_b are related to particles' center-to-center distances $L_{m,1}$, $L_{m,2}$, and L_b, respectively. On the other hand, from the 2-D geometric representation of the equal capillary pressure concept of Fig. 3.2b one can conjecture that

$$L_b = \frac{L_{m,1} + L_{m,2}}{2} \tag{3.7}$$

Or in a more general form,

$$L_b = n_1 L_{m,1} + n_2 L_{m,2} \tag{3.8}$$

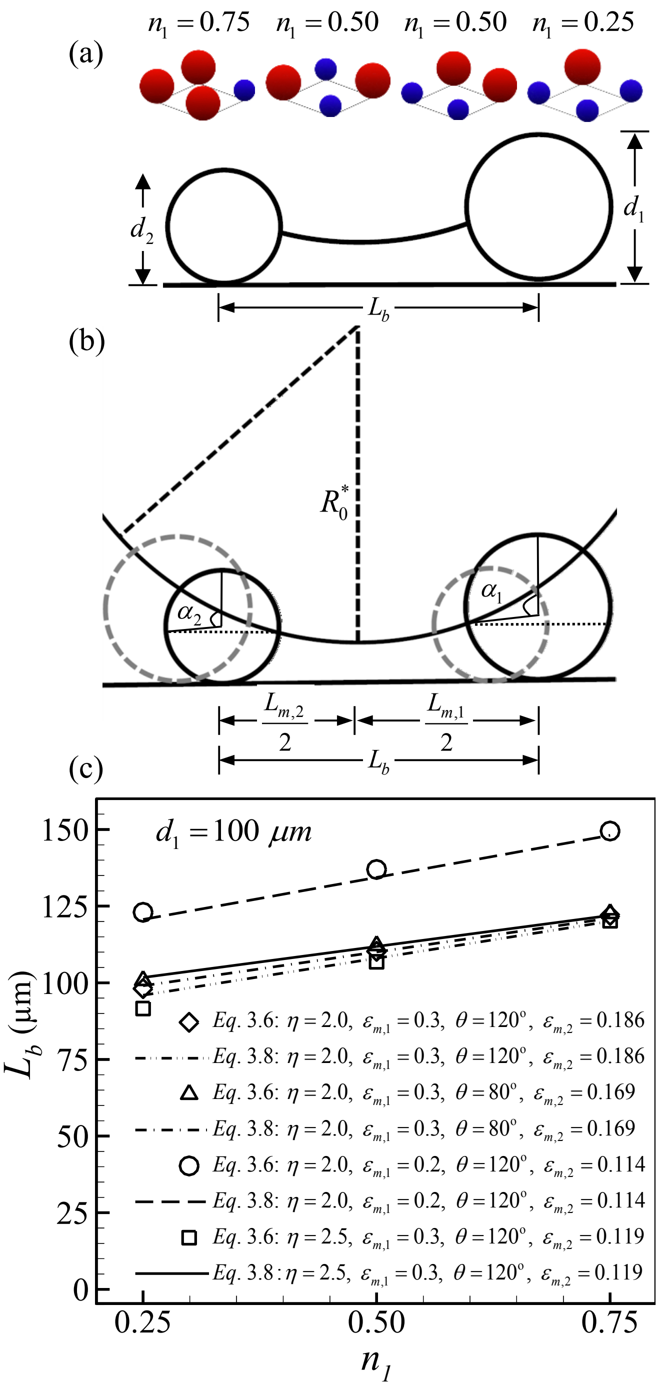

Fig. 3.2 (a): different arrangements of particles in a unit cell of a bi-dispersed coating; (b): the AWI in Regime II over a bi-dispersed coating can be modeled as AWIs over two different mono-dispersed coatings; and (c): comparison between bi-dispersed particles' center-to-center distance L_b obtained from of Eqs. (3.6) and (3.8) for coatings with a coarse particle diameter of $d_1 = 100$ μm with SVFs of $\varepsilon_{m,1} = 0.2$ and 0.3, YLCAs of $\theta = 120^\text{o}$ and 80^o, and different coarse-to-fine diameter ratios of $\eta = 2.0$ and 2.5.

The comparison between the center-to-center distance for bi-dispersed coatings L_b calculated from the force balance equation of Eqs. (3.2) and (3.6) and those from the conjectured Eq. (3.8) are given in Fig. 3.2c for coatings with a coarse particle diameter of $d_1 = 100$ μm, different SVFs of $\varepsilon_{m,1} = 0.2$ and 0.3, different YLCAs of $\theta = 120^{\circ}$ and 80° and different coarse-to-fine diameter ratios of $\eta = 2.0$ and 2.5. The encouraging agreement shown in Fig. 3.2c was in fact a motivation to use Eq. (3.8) in the remainder of this chapter.

We can now propose a simple method to find a mono-dispersed equivalent coating in terms of the geometric and hydrostatic parameters of bi-dispersed structures as shown in Figs. 3.3a and 3.3b with $L_b = L_{eq}$. In these figures, $O_1O_0 = S_1$ and $O_2O_0 = S_2$ where $O_1\!:\left|\begin{matrix}\frac{L_{m,1}}{2}\\ \frac{d_1}{2}\end{matrix}\right.$, $O_2\!:\left|\begin{matrix}-\frac{L_{m,2}}{2}\\ \frac{d_2}{2}\end{matrix}\right.$ are the center of the particles and $O_0\!:\left|\begin{matrix}0\\ z_0\end{matrix}\right.$ is the center of the meniscus. Considering the triangles $\varDelta M_1O_0O_1$ and $\varDelta M_2O_0O_2$,

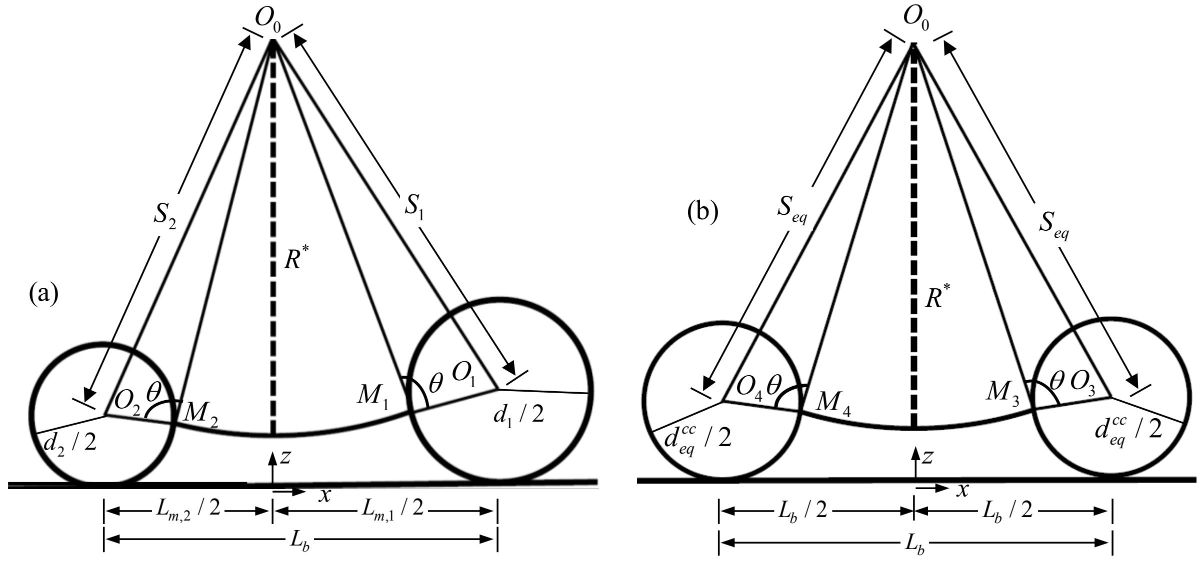

Fig. 3.3 Schematic presentation of an AWI over a bi-dispersed coating (a) and over its mono-dispersed equivalent (b).

we can write,

$$\begin{cases} (\frac{d_1}{2})^2 + R^{*2} - 2\frac{d_1}{2}R^*cos\theta = (\frac{L_{m,1}}{2})^2 + \left(z_0 - \frac{d_1}{2}\right)^2 \\ (\frac{d_2}{2})^2 + R^{*2} - 2\frac{d_2}{2}R^*cos\theta = (L_b - \frac{L_{m,1}}{2})^2 + (z_0 - \frac{d_2}{2})^2 \end{cases} \tag{3.9}$$

Now assume that the same interface (with $O_0\!:\left|\begin{matrix}0\\ z_0\end{matrix}\right.$) is formed over a coating having an equivalent diameter d_{eq}^{cc} (the superscript cc denoting the constant curvature concept) with $O_4\!:\left|\begin{matrix}-\frac{L_{eq}}{2}\\ \frac{d_{eq}^{cc}}{2}\end{matrix}\right.$ as shown in Fig. 3.3b. One can now solve Eq. (3.9) for z_0 and $L_{m,1}$ and use this information in similar system of algebraic equations developed using Fig. 3.3b to obtain d_{eq}^{cc} as (note that $R^* = \frac{\sigma}{\Delta P}$),

$$d_{eq}^{cc} = \frac{L_{eq}^2 - 4R^{*2} + 4z_0^2}{4(z_0 - R^*cos\theta)} \tag{3.10}$$

The results of such calculations for a bi-dispersed system with $d_1 = 100$ µm and a coarse-to-fine particle diameter ratio of $\eta = 1.75$ are shown in Fig. 3.4a. Note that in this figure, d_{eq}^{cc} is almost a constant value that can be approximated with $d_{eq} = \frac{d_1+d_2}{2}$. In Fig. 3.4b, we investigated the effects of varying the particles' YLCA on the proposed equivalent mono-dispersed diameter for coatings with $\eta = 1.75$ and a constant SVF of $\varepsilon_b = 0.2$. It can again be seen that d_{eq} can be a good approximation for the equivalent mono-dispersed diameter d_{eq}^{cc}. Figure 3.4c shows the equivalent mono-dispersed diameter for bi-dispersed coatings with $\varepsilon_b = 0.2$ and a YLCA of $\theta = 120^{\circ}$ but with different coarse-to-fine particle diameter ratios. It can be seen that the mismatch between d_{eq}^{cc} and the suggested d_{eq} value somewhat increases with increasing the coarse-to-fine particle diameter ratio. Nevertheless, the simplicity of the definition $d_{eq} = \frac{d_1+d_2}{2}$ makes it an appealing proposal for obtaining an equivalent mono-disperse counterpart for a bi-disperse coating. In fact in a more generalized form one can write

$$d_{eq} = n_1 d_1 + n_2 d_2 \tag{3.11}$$

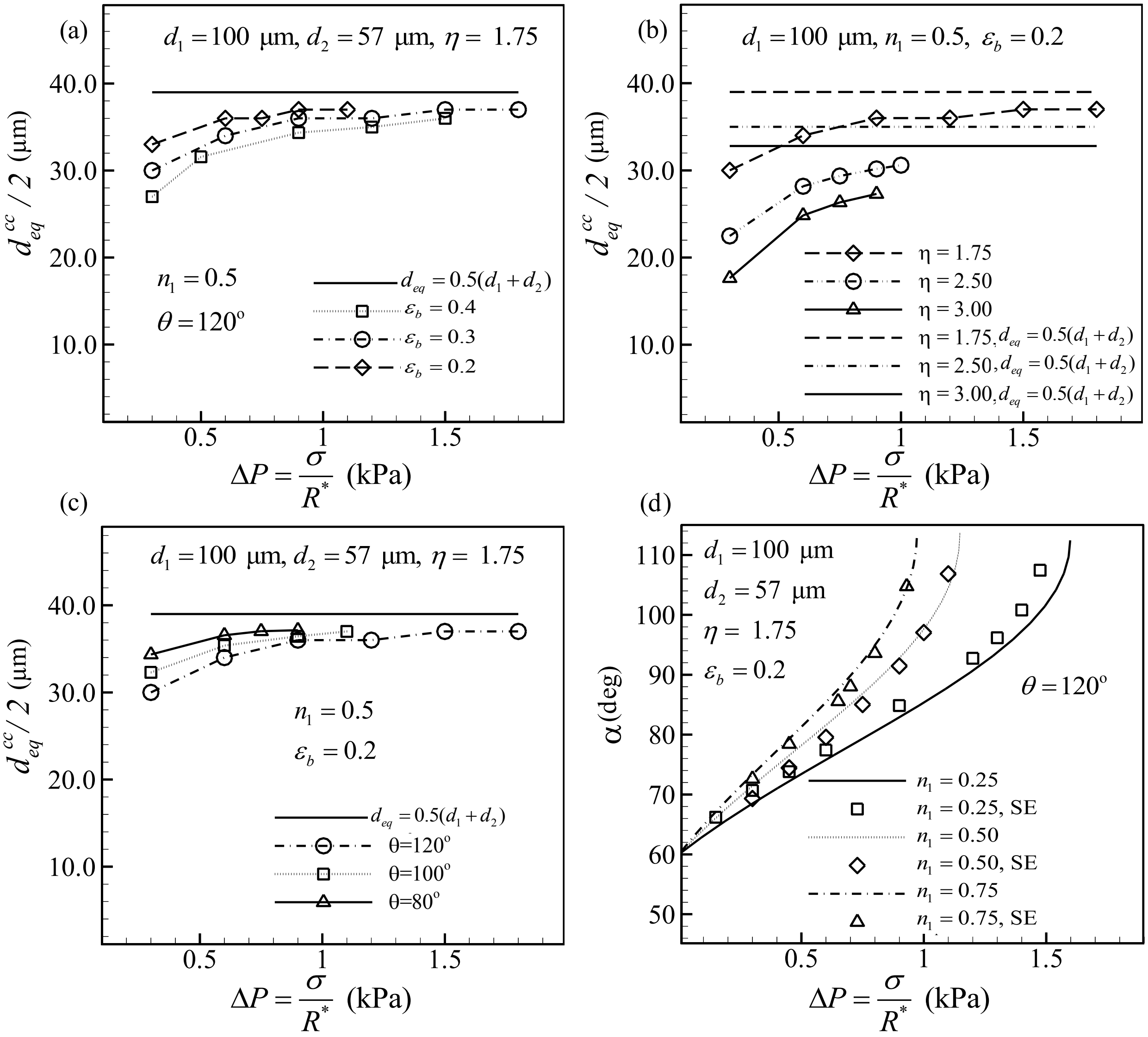

Fig. 3.4 Mono-dispersed equivalent diameter a function of capillary pressure from Eq. 10 is compared with that of Eq. 11 for bi-dispersed coatings with $d_1 = 100$ µm and $n_1 = 0.5$; (a): coatings with different SVFs; (b): coatings with different coarse-to-fine particle diameter ratios; and (c): coatings with different YLCAs. A Comparison between the immersion angles obtained from SE simulations and our ED analytical method is given in (d) for coatings with different coarse particle number fractions.

To further examine the accuracy of such a simple equivalent diameter definition, we compared the IA values obtained from SE simulation of bi-dispersed coatings with those of mono-dispersed equivalent coating from analytical formulations in Fig. 3.4d. In this figure in particular, we considered a bi-dispersed coating with $d_1 = 100$ µm and $\eta = 1.75$ but with different number fraction for the coarse particles. We then used Eq. (3.1) along with Eq. (3.11) to calculate the IA. Good agreement between the two predictions is evident from Fig. 3.4d.

The above-mentioned equivalent diameter can actually be modified and used for bi-dispersed coatings with particles having random spatial distributions (see Fig. 3.5).

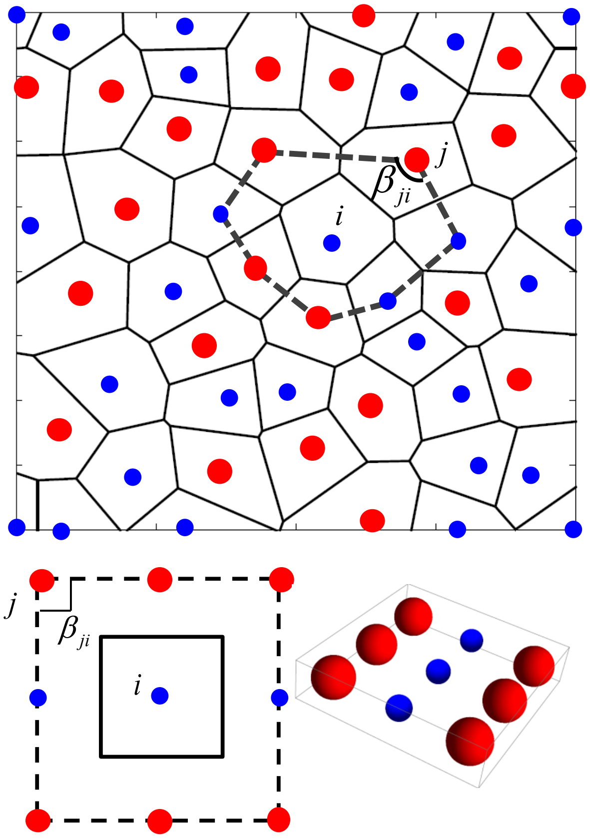

Fig. 3.5 An example coating with randomly distributed bi-dispersed particles shown with its Voronoi diagram. Note the particles surrounding particle i in the center of the largest Voronoi cells. Particles arranged in an ordered configuration present a special case for the analysis presented in this in this article.

Each cell in a Voronoi diagram marks the points whose distance to the particle in the center of the cell is less than or equal to their distance to the other particles in the domain. For a cell-hosting particle i surrounded by k different particles, one can write

$$d_{eq} = \frac{2\pi d_i + \sum_{j=1}^{k} \beta_{ji} d_j}{k\pi} \tag{3.12}$$

where β_{ji} is the angle at which particle j sees particle i. For particles with ordered arrangements, Eq. (3.12) reduces to Eq. 3.11 as shown in the lower figures in Fig. 3.5. CHP and the wetted area of a submerged bi-dispersed coating can now be predicted via simple analytical formulations using the equivalent diameter expressions given in Eq. (3.12). This analytical calculation method is hereon referred to as Equivalent Diameter (ED) method and its predictions are compared with those of SE simulations later in Sec. 3.3 for validation.

3.2.4 Pressure Regimes

As mentioned earlier, we consider two different pressure regimes for the performance of submerged bi-dispersed granular coatings. Figure 3.6a shows the AWI in Regime I. Increasing the hydrostatic pressure forces the AWI to penetrate into the pore space between the particles. At some hydrostatic pressure, the AWI comes into contact with the smaller particles and the surface starts to transition to Regime II, as can be seen in Fig. 3.6b. At the hydrostatic pressure where the transition from Regime I (Fig.3. 6b) to Regime II (Fig. 36.6c) takes place, one can assume that $P_{cap} + P_{bub}$ is a constant value as $P_\infty + P_h$ is a constant (see Eq. (3.3)). For the new interface $A'B'$ (with the coordinates of the A': $\left| \begin{matrix} x_{A'} \\ z_{A'} \end{matrix} \right.$ and B': $\left| \begin{matrix} x_{B'} \\ z_{B'} \end{matrix} \right.$), we can use a similar method as discussed in Fig. 3.3a to calculate $x_{A'}, x_{B'},\ z_{A'}$ and $z_{B'}$.

In addition, considering an isentropic compression for the volumes $V_{A'B'}$ and V_{AB}, we obtain

$$P_{bub,A'B'} = P_{bub,AB}\left(\frac{V_{AB}}{V_{A'B'}}\right)^{\gamma} \tag{3.14}$$

where the subscripts AB and $A'B'$ denote to the quantities associated with interfaces AB and $A'B'$.

Finally

$$\Delta P_{A'B'} = P_{\infty} + P_h - P_{bub,A'B'} \tag{3.15}$$

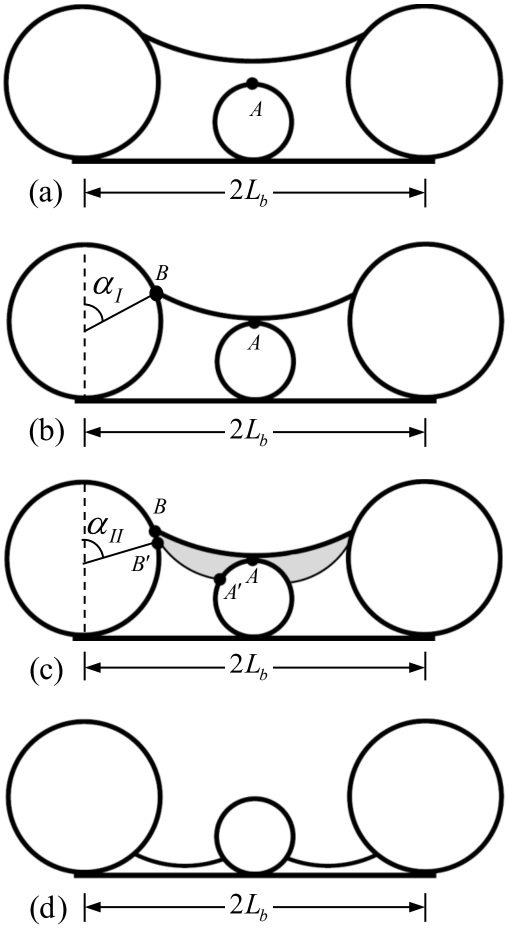

Fig. 3.6 A schematic presentation of the AWI in Regime I is shown in (a). Transition from Regime I to Regime II takes place when the AWI comes into contact with smaller particles at a higher pressure (b). A new stable AWI forms in Regime II (c). Further increase in the hydrostatic pressure causes the AWI to penetrate deeper into the coating as shown in (d).

Examining Eqs. (3.13) through (3.15), one can show that $\Delta P_{A'B'} < \Delta P_{AB}$ and therefore, $P_{bub,A'B'} > P_{bub,AB}$, i.e. the bubble pressure increases at the moment when the AWI comes into contact with the smaller particles. Both our analytical and numerical calculations indicate that the change in the IA at the moment of transition from Regime I to Regime II is relatively small, i.e. $\alpha_I \cong \alpha_{II}$ (points B and B'in Fig 3.6c are very close to one another). Obviously, further increase in the hydrostatic pressure causes the AWI to penetrate deeper into the coating as shown in Fig. 3.6d. The surface will transition to the fully wetted Wenzel state if the AWI touches substrate or become unstable under excessive pressures. Note that transition from Regime I to Regime II is irreversible, i.e. decreasing the hydrostatic pressure does not necessarily result in the formation of an AWI that is in contact with the larger particles only.

3.3 Results and Discussion

In this section, we study how granular coatings perform under different hydrostatic pressures. For the sake of continuity, we start this section with a study on mono-dispersed coatings with ordered particles. Figure 3.7 shows the variation of CCP with SVF for different mono-dispersed coatings with particle diameters of $d_1 = 1$ µm and $d_2 = 100$ µm and YLCAs of $\theta = 120^{\circ}$and 80°(all parameters are chosen arbitrarily for demonstration purposes). Figure 3.7 shows that for a constant diameter and a constant YLCA, increasing the SVF increases the capillary forces leading to higher CCPs. Note also that from Eq. (3.2), for constant YLCAs and particle diameter, the maximum capillary pressure depends only on the coating's SVF and increases as SVF increases. On the other hand, for a specific SVF and particle diameter, the critical pressure decreases with decreasing YLCA.

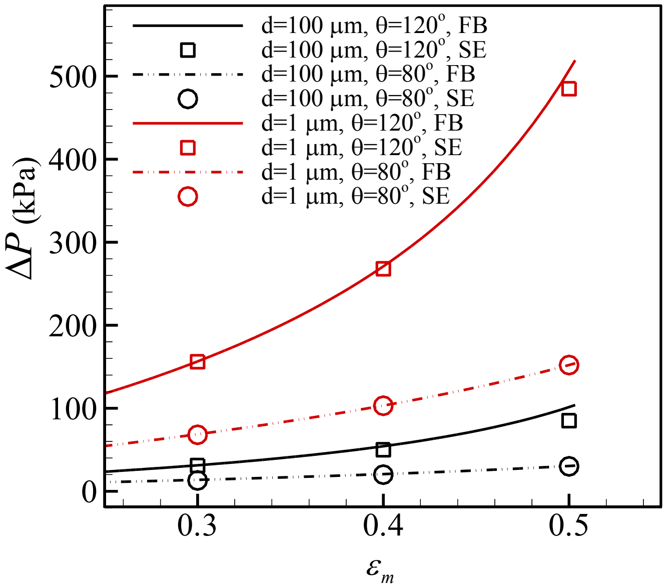

Fig. 3.7 Critical capillary pressure predictions obtained from FB and SE calculations for mono-dispersed coatings comprised of particles with $d_1 = 100$ μm and $d_2 = 1$ μm.

This is because by decreasing the YLCA, the capillary forces decrease and the AWI penetrates deeper into the pores of the coating. Finally, for a constant SVF and YLCA, critical pressure is higher for smaller diameters as capillary forces become stronger when the particles are smaller. Figure 3.7 also shows perfect agreement between the results of our FB analytical calculations and those of SE simulations, verifying the accuracy of our calculations. As mentioned in Chapter 2, the small discrepancy between the analytical and SE results at high SVFs is because the variation of the IA along the perimeter of the particles is neglected in our analytical formulations.

3.3.1 Bi-Dispersed and Poly-Dispersed Coatings with Ordered Particle Distributions

As discussed before, the AWI over a bi-dispersed coating may only be in contact with the large particles if the hydrostatic pressure is low (Regime I). With increasing hydrostatic pressure, however, water starts penetrating into the pore space between the particles until it comes into contact with the smaller particles (Regime II) or touches the hydrophilic bottom surface. In fact, when the coarse-to-fine particle diameter ratio η is high, the AWI may fail before transitioning to

Regime II. Therefore, one can determine a maximum coarse-to-fine particle diameter ratio η_{max} below which the coating experiences Regime II before transitioning to the fully-wetted state.

Consider a 3-D AWI over a bi-dispersed coating with the coarse and fine particles having diameters of d_1 and d_2, respectively (see Fig. 3.8a). Figure 3.8a shows the interface over the large particles with $R_1^*= \frac{\sigma}{\Delta P}$ being the radius of curvature of the AWI on the symmetry boundary of the unit cell (assume for a moment that the fine particles did not exist). Therefore, using the information given in the previous sections, one can obtain the distance between the AWI and the substrate at the CCP, ΔP^{cr}, calculated for a mono-dispersed coating made of the coarse particles (i.e., $z_{min}^{cr} = z_{min}|_{\Delta P_m = \Delta P^{cr}}$).

For a bi-dispersed coating to experience Regime II before failure, the minimum distance between the AWI and substrate should be smaller than the diameter of the fine particles, i.e. $z_{min}|_{\Delta P = \Delta P^{cr}} < d_2$. In other words, if $\eta = \frac{d_1}{d_2} > \eta_{max} = \frac{d_1}{z_{min}^{cr}}$, then the smaller particles cannot contribute to the stability of the AWI under pressure, as the interface fails before reaching them. However, note that depending on whether the smaller particle happens to be on the boundary of the cell or in the middle of it, different z_{min} values should be considered in the analysis, i.e., z_1 or z_2 (minimum AWI height at the boundary or in the center of the cell, respectively). Here for simplicity we define η_{max} assuming that the smaller particle is at the cell boundary.

$$\eta_{max} = \frac{d_1}{z_1^{cr}} \tag{3.16}$$

From Fig. 3.8a, we can obtain $b_1 = R_1^* - \sqrt{{R_1^*}^2 - {b_2}^2}$ and finally we can write

$$z_1 = \frac{d_1}{2} - \frac{d_1}{2} sin\alpha - \left(R_1^* - \sqrt{R_1^{*2} - \left(\frac{L_b}{2} - R_1^* sin\alpha\right)^2}\right) \tag{3.17}$$

Figure 3.8b shows η_{max} versus SVF for bi-dispersed coatings with different YLCAs. As can be seen, η_{max} decreases with increasing SVF. Based on the above discussion, we chose η=1.75 and 2.5 with a contact angle of 120^o for our simulations.

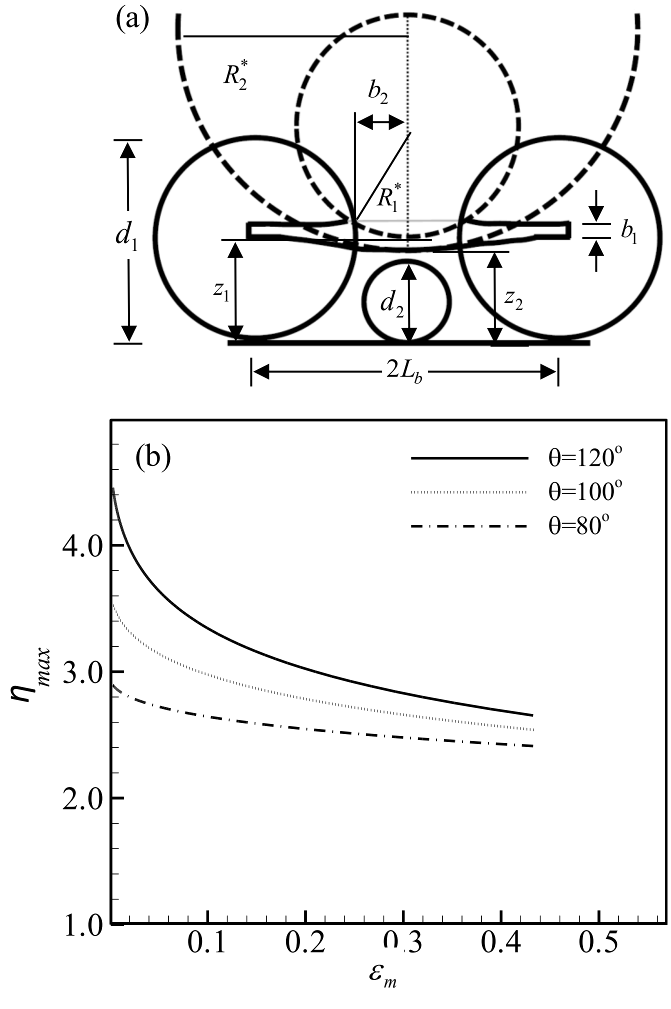

Fig. 3.8 The minimum points for an AWI are shown with z_1 and z_2 at the cell boundary and cell center, respectively in (a). Maximum coarse-to-fine particle diameter ratio versus SVF for mono-dispersed coatings with different YLCAs is shown in (b).

The critical IA on coarse particles in Regime I (i.e., when the AWI is in contact with coarse particles only) is always greater than that in Regime II (i.e., when the AWI is in contact with both particle types). Therefore, if a bi-dispersed coating is expected to fail in Regime I due to AWI going beyond the critical IA, it will also fail in Regime II. In other words, presence of the fine particles cannot improve the stability of such an AWI.

Figure 3.9a shows a comparison between the CCP values obtained from SE simulations and those from our ED method. As can be seen in this figure, CCP increases with increasing SVF. As expected, the critical pressure values associated with bi-dispersed particles are bounded by their corresponding limiting cases of mono-dispersed coatings made of coarse or fine particles. It can also be seen that predictions of our simple analytical formulation are in good agreement with the results of the more rigorous calculations of SE code. To further examine the accuracy of our equivalent particle diameter definition for predicting the CCP of a bi-dispersed coating, we repeated the results of Fig. 3.9a for when the coarse-to-fine particle diameter ratio is 2.5. Good agreement can again be observed between the SE results and those of our ED method.

Figure 3.9c shows the CHP versus SVF for bi-dispersed coatings with different number fractions. Good agreement between our equivalent diameter formulations and the SE results can again be observed in this figure. It can be seen that CHP first decreases with increasing SVF, and then increases. This behavior is due to the interplay between the capillary forces and the forces generated by the compressed air bubble. To better understand this behavior, one should pay close attention to how the capillary forces and air resistance vary with SVF. By increasing the SVF, the capillary pressure plays a greater role in balancing the hydrostatic pressure as the ratio of the three-phase contact line to the area of the AWI increases.

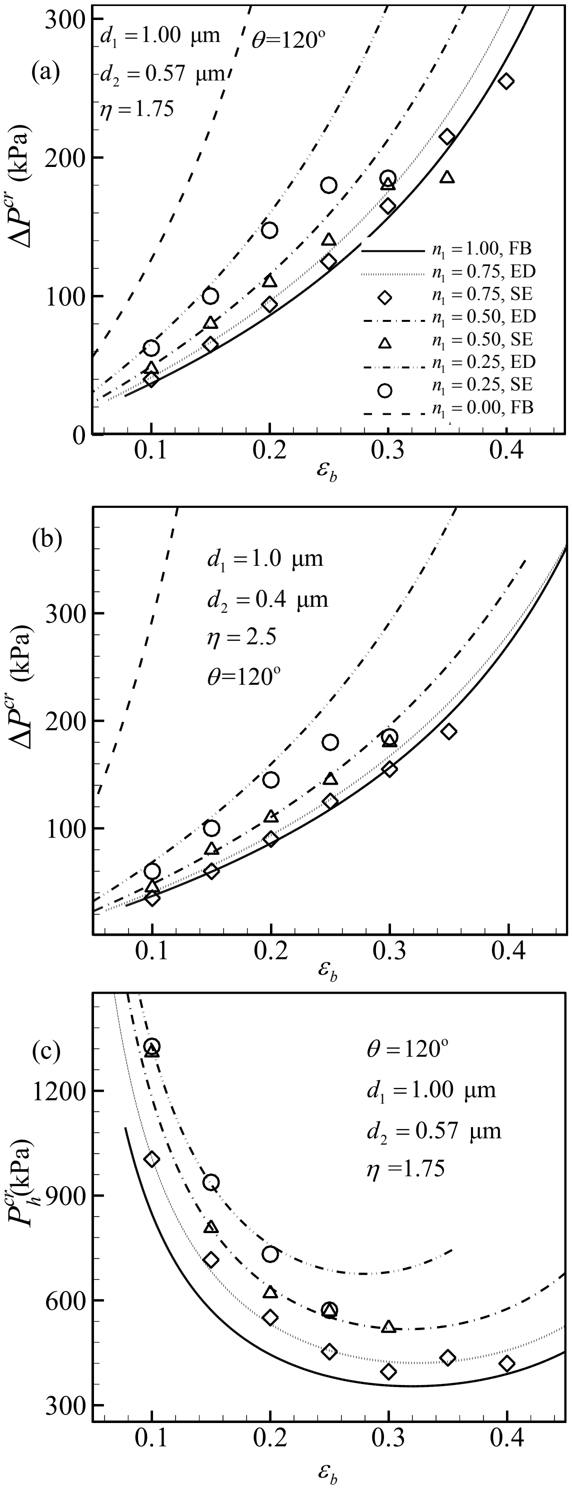

Fig. 3.9 CCP values obtained from FB and SE calculations for bi-dispersed coatings having a coarse particle diameter of $d_1 =$ μm and an YLCA of $\theta = 120^{\mathrm{o}}$ are given in (a) and (b) for with η =1.75 and η =2.5, respectively. CHPs for coatings of figure (a) are shown in (c).

The compression forces, on the other hand, are proportional to the compression ratio of the entrapped air $C = \frac{V_\infty}{V}$, which is a function of IA ratio $\frac{\alpha_\infty}{\alpha^{cr}}$. As explained before, the critical IA decreases as SVF increases, causing the compression ratio to decrease when SVF increases. Therefore, increasing SVF decreases the resistance of the entrapped air against the hydrostatic pressure but increases the capillary force. The outcome, therefore, varies depending on the SVF and size of the particles.

We also checked the validity of our equivalent particle diameter definition in conditions where it was expected to be least accurate according to Fig. 3.8b and Fig. 3.5, i.e., coatings with $\varepsilon_{m,1} = 0.1$ and $\eta = 3.3$, or coatings with $\varepsilon_{m,1} = 0.5$ and $\eta = 2.85$. Table 1 compares the results of our calculations with those of SE simulations.

Figures 3.10a–3.10c show the wetted area A_w as a function of hydrostatic pressure for three bi-dispersed coatings with $\varepsilon_b = 0.2$, $d_1 = 1$ µm, and $\eta = 1.75$ but different n_1 values of 0.75, 0.5, and 0.25, respectively. Note that the wetted area for mono-dispersed coatings comprised of coarse-only or fine-only particles are identical (the case of $n_1 = 0$ and $n_1 = 1$). This is because for mono-dispersed coatings with constant SVFs, the AWI shape is independent of the particle diameter (35). As expected, wetted area increases with hydrostatic pressure. It is interesting to note in Figs. 3.10a–3.10c that, at small hydrostatic pressures (e.g., 40 kPa), the wetted area for the coating with $n_1 = 0.25$ is quite smaller than that of the two other coatings with $n_1 = 0.5$ and $n_1 = 0.75$. This trend, however, does not remain the same at higher hydrostatic pressures (e.g., 380 kPa) as shown with red dashed lines on the figures. To better understand this, one should pay close attention to the number of particles in contact with the AWI in each coating. For bi-dispersed coatings, the AWI is only in contact with the coarse particles when the hydrostatic pressure is low (Regime I), but it penetrates into the coating and eventually makes contact with smaller particles as pressure increases (see the insets in Fig. 3.10c). In contrast, the AWI is always in contact with two and three coarse particles in the case of coatings with $n_1 = 0.5$ and $n_1 = 0.75$, respectively (see the insets in Fig. 3.10b and 3.10a). Therefore, one can expect a lower wetted area (and perhaps a lesser skin friction) from a bi-dispersed coating with $n_1 = 0.25$ at low hydrostatic pressures.

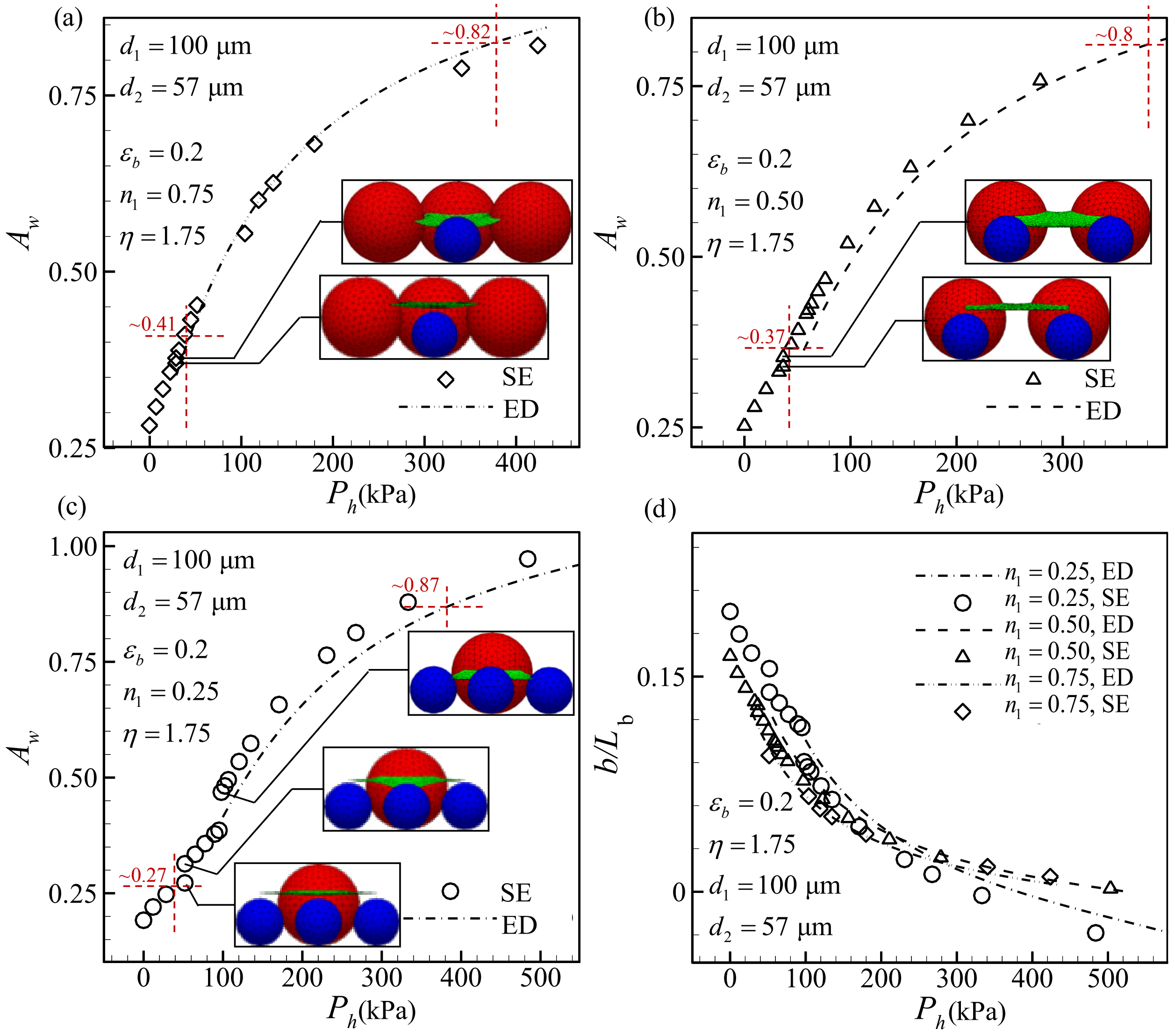

Fig. 3.10 Wetted area versus hydrostatic pressure obtained from ED and SE calculations for bi-dispersed coatings having ε_b=0.2 and η =1.57 are shown in (a) for $n_1 = 0.75$, in (b) for $n_1 = 0.50$, and in (c) for $n_1 = 0.25$. Dimensionless slip length is presented as a function of hydrostatic pressure for bi-dispersed coatings having SVF of 0.2 and η =1.57 in (d).

At higher pressures, the wetted areas for coating with different population of coarse particles are comparable to one another. It is also interesting to report that an increase in the wetted area is observed when the AWI comes into contact with the fine particles, at an almost constant hydrostatic pressure (see the insets in Fig. 3.10a–3.10c). This happens once for coatings with $n_1 = 0.5$ and $n_1 = 0.75$ but two times for the coating with $n_1 = 0.25$. As can be seen in Figs. 3.10a–3.10c, our analytical formulations can successfully predict a coating's wetted area in Regime II. However, note that our equivalent diameter equation was derived using constant center-to-center distance between the particles. In other words, the wetted area of a bi-dispersed coating is obtained using an equivalent mono-dispersed coating with the same center-to-center distance (not the same SVF).

As mentioned earlier, one of the main attributes of SHP surfaces is their ability to reduce the water skin-friction drag. The reduction in the skin-friction drag is often characterized by the so-called slip length, the imaginary distance below the surface at which the water velocity extrapolates to zero (60). As discussed in Chapter 2, there are only a few explicit formulas that relate the slip length and wetted area to one another (see for instance (82–85) for internal flows over SHP surfaces comprised sharp-edged grooves in the stream-wise or transverse directions). The slip length for flow between two parallel plates over SHP monofilament woven screens is given as (1):

$$b = \frac{L}{3\pi} ln\left(\frac{2(1+\sqrt{1-A_w})}{\pi\, A_w}\right) \tag{3.18}$$

As discussed in Chapter 2, Eq. (3.18) assumes a planar structure for the surface (i.e., where A_w never exceeds 1), and so it is not very accurate for the coatings considered in this chapter. Nevertheless, in the absence of a better alternative, we use this expression here as a means of demonstrating the effects of hydrostatic pressure on slip length, but only for coatings with $A_w \leq$

1. Figure 3.10d shows the dimensionless slip length as a function of hydrostatic pressure for a bi-dispersed coating with $\varepsilon_b = 0.2$. One can easily detect the changes in the slip length values corresponding to those shown in Figs. 3.10a–3.10c for wetted area.

To study coatings comprised of poly-dispersed particles with ordered distribution, we study the case of having four different particle diameters in a unit cell. We propose a mono-dispersed equivalent diameter for coatings with poly-dispersed particles having ordered arrangements,

$$d_{eq} = \sum_{i=1}^{4} n_i d_i \tag{3.19}$$

Figure 3.11a shows our critical pressure predictions obtained for a series of arbitrarily chosen granular coatings with different SVFs and YLCAs comprised of particles with diameters of $d_1 = 100$ μm, $d_2 = 57$ μm, $d_3 = 40$ μm, and $d_4 = 31$ μm.

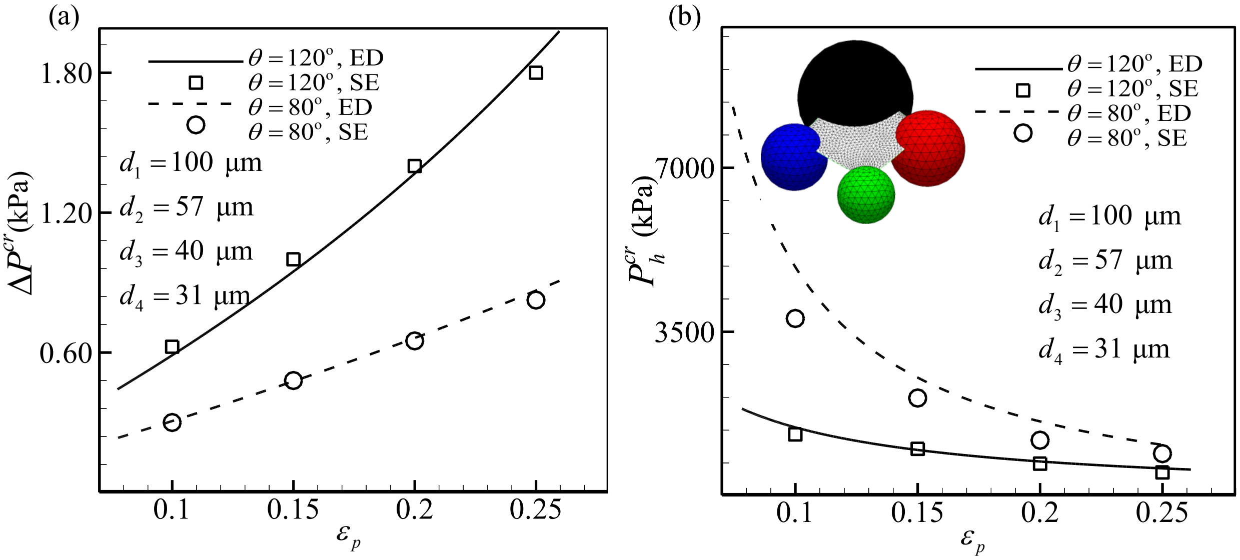

Fig. 3.11 CCP (a) and CHP (b) predictions from FB and SE calculations for poly-dispersed coatings with ordered particle arrangements having different SVFs and YLCAs.

It can be seen that, CCP increases with SVF and YLCA, as expected. The CHP, on the other hand, varies with SVF and YLCA very differently as shown in Fig. 3.11b (see Chapter 2 for more information). The predictions of SE simulations are also added to both Fig. 3.11a and 3.11b for comparison. Good agreement between the two calculation methods is evident.

3.3.2 Bi-Dispersed and Poly-Dispersed Coatings with Random Particle Distributions

In this section, we examine the effectiveness of our equivalent mono-dispersed particle diameter method in representing coatings having particles with random spatial distributions. For the clarity of the presentation, we start with coatings comprised of randomly distributed bi-dispersed particles and then move on to the more general case of poly-dispersed particles. In generating the virtual coatings with random particle distributions, we considered an $8d_1 \times 8d_1$ domain with periodic boundary condition and enforced a minimum distance of $d_1/16$ between the particles to prevent them from touching one another (see Chapter 2 for more detailed information). These virtual coatings were generated using an in-house MATLAB program and exported to SE.

It is important to note that we have assumed here that surfaces with bi-dispersed (or poly-dispersed) particles will exhibit a single failure pressure that can be equated to that of an equivalent surface with mono-dispersed particles. This assumption is justified for when the surface on which the particle coating is deposited is hydrophilic. Therefore, if water comes in contact with the hydrophilic underlying surface, it will follow the surface and practically wets the entire coating. This is not necessarily the case with the underlying surface being hydrophobic. In the latter case, a bi-dispersed (poly-dispersed) coating will exhibit a poly-dispersed transition from Cassie to Wenzel state (i.e., AWI will collapse at lower pressures where the particles are farther apart and/or more wettable, and particles that are closer together and more hydrophobic will delay penetration).

As described in Chapter 2, for a submerged coating with randomly distributed particles, the failure takes place where the particles are locally farther away from one another (35). The CCP of such a coating can be calculated using our ED analytical method but with the help of a Voronoi diagram. We therefore refer to this method as VED method. As explained before, CCP was found to increase with SVF as more particles contribute to the capillary pressure of a coating at a higher SVF. On the contrary, the CCP appeared to decrease with increasing the particle diameter when the SVF was kept constant (see Fig. 2.7 and related discussion in chapter 2).

We also observed that CCP decreases with increasing the coarse-to-fine particle diameter ratio η from 1.75 to 2.5 (we increased the coarse-to-fine particle diameter ratio while maintaining both the SVF and number fraction of coarse particles constant). Increasing η increases the presence of coarse particles, and so it weakens the capillary pressure of the coating. For the same reason, CCP also decreases with increasing the number fraction of the coarse particles n_1 (the results of these calculations are not shown for the sake of brevity). It is worth mentioning that the date generated here for coatings with fixed number fractions can be presented in terms of particle's mass fraction, if needed for practical applications.

The CCP values and the volume under the AWI were used in Eq. (3.3) and (3.4) to predict CHP. To do this analytically, one can calculate the volume under the AWI across the entire coating by knowing the CCP and applying that pressure to the mono-dispersed equivalent of the bi-dispersed coating at hand. This allows us to find a representative mono-dispersed IA for the system and thereby the volume under the AWI. It was found that CHP decreases with SVF increasing, due to the decrease in the compression forces (the changes in the capillary forces are comparatively negligible). Similarly, CHP decreases when n_1 increases (see Fig. 3.9 for related information). The results of our simple analytical method were found to be in good relative agreement with those of the numerical calculation of the SE code leading to an average error of less than 35% (the actual data are not shown for the sake of brevity).

The effect of increasing the coarse-to-fine particle diameter on CHP is somewhat different than that on CCP. In fact, CHP increases with increasing coarse-to-fine particle diameter ratio. This is because the capillary pressure of the coating with $\eta = 2.5$ is smaller than that of the coating with $\eta = 1.75$ and therefore at the critical point, the AWI penetrates deeper into the pores of the coating with $\eta = 2.5$, and so generates a greater air compression (i.e., a higher CHP). We also predicted the wetted area and the slip length of these coatings under different hydrostatic pressures (see Figs. 3.12a and 3.12b). As expected, the wetted area increases, and so the slip length decreases, with increasing the hydrostatic pressure. Interestingly, it can be seen that the wetted area decreases with increasing η. Figure 3.12c shows the AWI shape and position for coatings with different coarse-to-fine particle diameter ratios but a constant coarse number fraction of n_1=0.5 at a hydrostatic pressure of $P_h = 80$ kPa. For better comparison, we have also reported the changes of the volume of the entrapped air $\frac{V}{V_\infty}$ in each case. For the same reason, the coating with $\eta = 2.5$ can withstand a higher hydrostatic pressure (i.e., has a higher CHP).

Finally, we consider a more general case in which both the YLCA and particle diameters change from one particle to another. We consider arbitrary coatings with four different particle diameters of $d_1 = 100$ µm, $d_2 = 57$ µm, $d_3 = 40$ µm, and $d_4 = 31$ µm with different YLCA of $\theta_1 = 120^\circ, \theta_2 = 100^\circ, \theta_3 = 80^\circ$ and $\theta_4 = 60^\circ$.

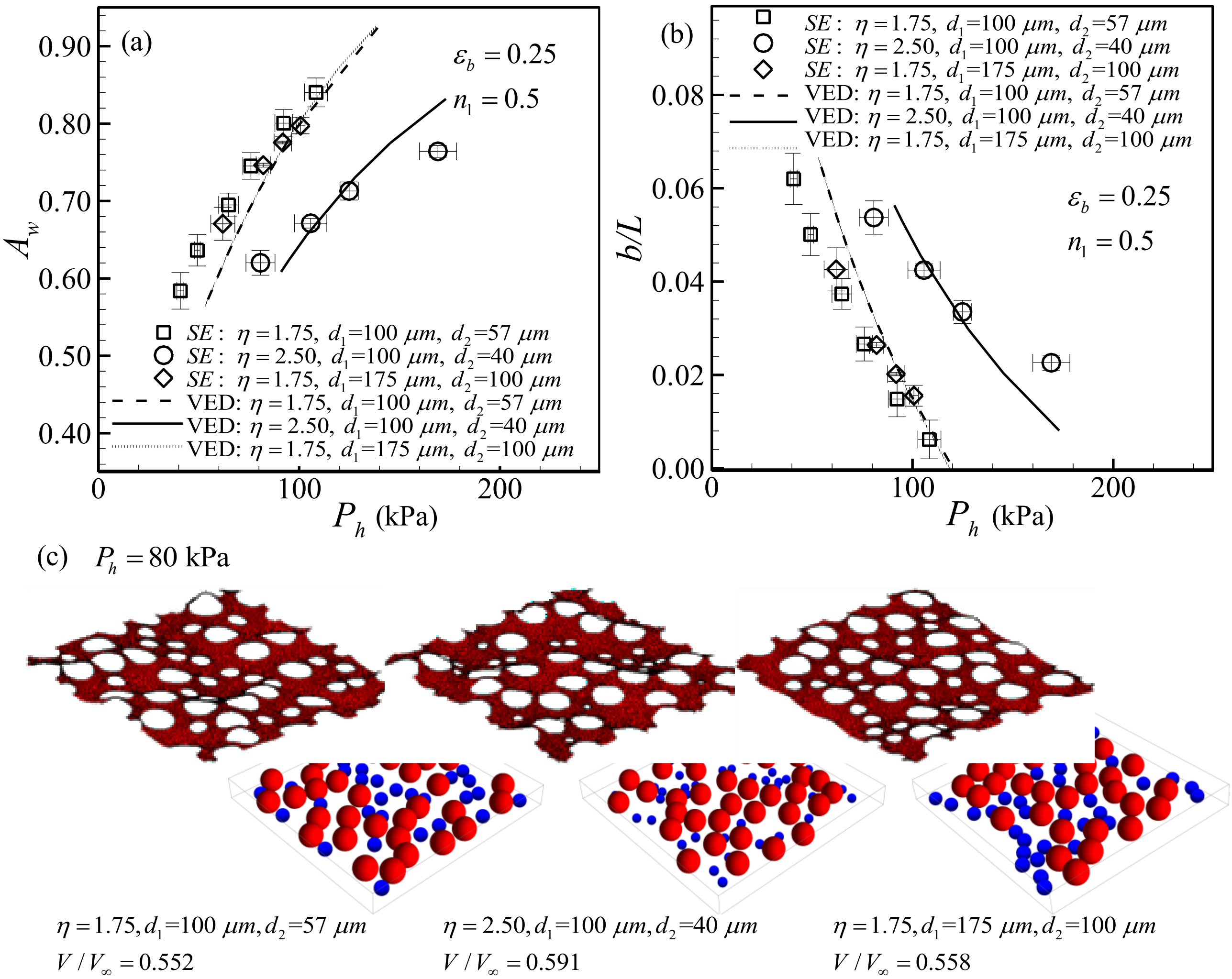

Fig. 3.12 Wetted area (a) and dimensionless slip length (b) versus hydrostatic pressure obtained from VED and SE calculations for bi-dispersed coatings with random particle distributions having ε_b=0.25, $n_1 = 0.5$, $d_1 = 100$ μm or 175 μm, and $\eta = 1.75$ or 2.5 in Regime II. AWI examples over these coatings are shown in (c) at a hydrostatic pressure of $P_h = 80$ kPa.

We use the equivalent particle diameter of Eq. (3.12) along with the general form of equivalent contact angle of chapter 2 (35):

$$\begin{cases} d_{eq} = \frac{2\pi d_i + \sum_{j=1}^{k} \beta_{ji} d_j}{k\pi} \\ \cos\theta_{eq} = \frac{2\pi cos\theta_i + \sum_{j=1}^{k} \beta_{ji} cos\theta_j}{k\pi} \end{cases} \tag{3.20}$$

Figures 3.13a and 3.13b report CCP and CHP for these coatings obtained from our VED method and the SE simulations, respectively.

Very good agreement between the SE simulations and our VED analytical calculations is evident in Fig. 3.13a and 3.13b. Figures 3.13c and 3.13d show the wetted area and the slip length of the above-mentioned coatings under different hydrostatic pressures for an SVF of 0.20, respectively.

As expected, the wetted area increases with hydrostatic pressure, as the AWI penetrates further down into the pores between the particles. It can also be seen that wetted area decreases with increasing the YLCA. Figure 3.13d shows the slip length versus SVF. As expected, slip length decreases with increasing the hydrostatic pressure.

Once again, note that we have assumed that the surface on which the particle coating is deposited is hydrophilic. Therefore, if water comes in contact with the hydrophilic underlying surface, it will follow the surface and practically wets the entire coating. This is not necessarily the case with hydrophobic underlying surfaces.

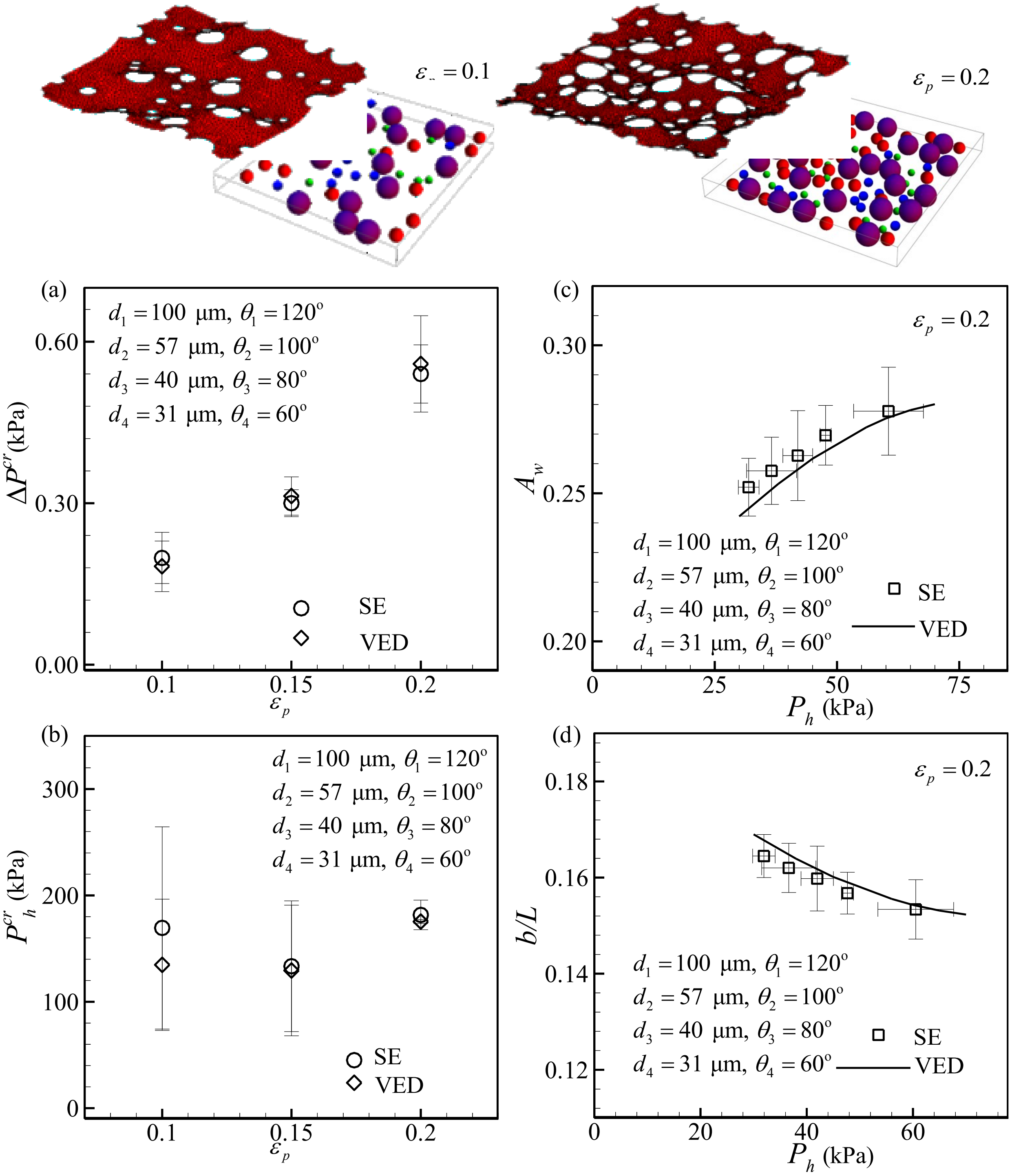

Fig. 3.13 Our CCP and CHP predictions are presented in (a) and (b) along with the SE results for poly-dispersed coatings with randomly distributed particles, respectively. The coatings consist of particles with diameters and YLCAs of $d_1 = 100\ \mu\text{m}, \theta_1 = 120^{\text{o}}, d_2 = 57\ \mu\text{m}, \theta_2 = 100^{\text{o}}, d_3 = 40\ \mu\text{m}, \theta_3 = 80^{\text{o}}, d_4 = 31\ \mu\text{m}$, and $\theta_4 = 60^{\text{o}}$. Wetted area and dimensionless slip length are reported for poly-dispersed coatings with $\varepsilon_p = 0.2$ in (c) and (d), respectively.

3.4 Summary

This section summarizes the methodology that we have developed for predicting the critical pressure and wetted area of poly-dispersed granular coatings with randomly distributed particles having different diameters of d_i, YLCAs of θ_i, and number fractions of n_i in a flowchart (see Fig. 3.14). This flowchart shows how a mono-dispersed equivalent coating having d_{eq} and θ_{eq} can virtually be produced and used to estimate the behavior of the original poly-dispersed coating.

In order to calculate d_{eq} and θ_{eq} for a poly-dispersed coating a Voronoi diagram should be generated. The Voronoi cell with the maximum area and its neighboring particles are then marked. The center-to-center distance between these k neighboring particles, L_{lj}, are then obtained from the Voronoi diagram. If at the given pressure the AWI comes into contact with all these k particles, by using Eq. 3.20 the Voronoi cell can be converted into a square unit cell with mono-dispersed particles with a diameter of d_{eq} and an YLCA of θ_{eq}. However, if only some of these k particles come into contact with the AWI, then the untouched particles should be removed from this calculation.

For any two particles on the Voronoi cell with center-to-center distance L_{lj} the height of the AWI z_1 over particles with a diameter of d_l can be found using Eq. 3.17. If $z_1 > d_j$, it means that the AWI is not in touch with this particle, therefore, the particle with diameter d_j should be removed from the calculation. After excluding all the dry particles (i.e., those not in contact with the AWI) from the calculations, d_{eq} and θ_{eq} can be calculated using Eq. 3.20. This can then be used to find α (Eq. 3.2), wetted area (Eq. 3.5), volume under the AWI (Ref. (35)) and the critical hydrostatic pressure (Eq. 3.3).

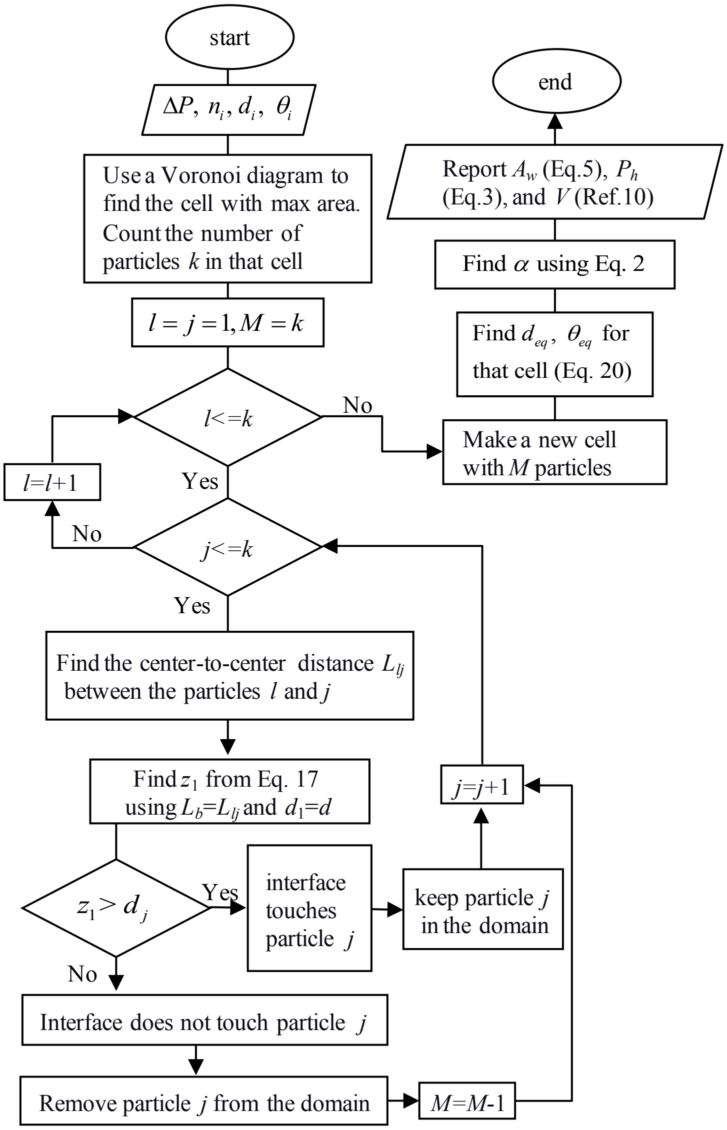

Fig. 3.14 Flowchart for calculating critical pressure and wetted area for a coating comprised of poly-dispersed randomly distributed particles of different diameters and YLCAs.

3.4 Conclusions

This chapter builds on the foundation that was developed in the first part of this two-part publication, but also extends our previous formulations to become applicable to superhydrophobic coatings of arbitrary particle size and contact angle distributions. In this chapter, we first studied simulated coatings with mono-dispersed particles to conclude that critical capillary pressure increases with increasing SVF. We also showed that unlike capillary pressure, wetted area is independent of particle diameter. We then investigated the effects of bi-dispersed and poly-dispersed diameter distributions on coatings' critical pressure and wetted area. We developed a mono-dispersed equivalent diameter definition that can be used to predict the critical pressure and wetted area of coatings with such particle size or contact angle distributions. The formulation developed here can be applied to coatings with random or ordered spatial particle distributions. At every step, we examined the accuracy of our analytical formulations with the more sophisticated and accurate numerical simulations conducted using the Surface Evolver code.

Chapter 4. Wetting Resistance of Superhydrophobic Fibrous Coatings with Layered Fibers

4.1 Introduction

superhydrophobicity —a phenomenon which may arise from combining hydrophobicity with roughness (59–62) have been used to reduce the drag force on an object submerged in moving water (10,12,14,15,22). The reason for that is SHP surface can entrap the air in the surface-pores, which is in contact with water, thereby reducing the contact area between water and the solid surface. Depending on the microscale geometry of the surface (i.e., roughness) and the hydrostatic/hydrodynamic pressure field, the air–water interface (AWI) may significantly ingress into the pores of the surface. The AWI may stay intact or even become impaled by the peaks of the surface. When the AWI is impaled, even when there is still air in the pores, an SHP surface may no longer provide a reduced solid–water contact area (referred to here as the wetted area), and hence, offers no drag reduction (68–71). In fact, it is quite possible that such a surface increases the drag force in certain hydrodynamic conditions as discussed in previous chapters.

Fabricating micro- or nano-roughness to generate SHP surfaces is a costly process, and applying them to geometries with arbitrary curvatures is very difficult. An alternative is to achieve the desired roughness by applying a hydrophobic material to the surface in the form of electrospun nanofibers (23,93–95) or apply a coating on the surface of a fibrous material (96–98). It has been shown that the conventional electrospinning process can be modified to produce coatings with some additional control over the orientation of the fibers and their spacing (e.g., (99–104).

It is worth mentioning that the methodology presented here can also be used in applications involving oil–water separation (105–109), water transport in fuel cells (110–113), waterproof barriers for underwater devices (114), and self-cleaning (e.g., (1,115)) among many others.

In the remainder of this chapter, we will first establish the method we use to simulate the fiber and also define criteria for critical pressure (Section 4.2). We will then explain the results of our simulation for orthogonal fibrous coating, oriented fibrous coating and wire screen coating in Section 4.3. Finally, we state our conclusions in Section 4.4.

4.2 Modeling Air-Water Interface on Fibrous Coating

In this section we present a numerical simulation conducted via Surface Evolver (SE) code to find the 3D shape of air-water interface, slip length and critical pressure. The SE code is able to solve for the minimum-energy shape of an interface between two immiscible fluids. The general form of the energy equation being integrated in the code can be expressed as (3):

$$E = p \iiint dv + \iint \sigma dA_{LG} - \sum \sigma cos\theta_i \iint dA_i \tag{4.1}$$

where p is pressure difference across the interface which is being integrated over volume element dV. A_{LG} represents the liquid-gas area. The summation refers to the energy contributed by the wetted area of each fiber associated with the interface. To ensure proper calculation of the fibers' energy contribution, the integrand dA_i must be derived for each fiber and applied explicitly in the code.

The reduction in the skin-friction drag is often described by slip length (22). After finding the 3D shape of the interface, solid-liquid area can be easily found and used to calculate the slip length as a function of pressure. An expression for slip length over SHP monofilament woven screens is suggested in ref. (1) as:

$$b = \frac{L_S}{3\pi} ln \left(\frac{2(1+\sqrt{1-A_W})}{\pi \, A_W} \right) \tag{4.2}$$

where A_w is dimensionless wetted area (ratio of curved solid-liquid area to the projected area). Note that Eq. 4.2 was originally developed for planar structures, i.e., A_w never exceeds 1. Nonetheless, in the lack of a better alternative, we apply this formula as a means of studying the effects of pressure on slip length, but only as long as $A_w \leq 1$.

At higher pressure air-water interface penetrates more into the pore between the fibers. At critical pressure the interface cannot tolerate the elevated the pressure and breaks through the fibers. This pressure is known as critical pressure. Analytically predicting critical pressure is only possible for a coating with fibers being highly oriented in a certain direction as will be discussed next.

For two parallel fibers the capillary pressure can be derived from the balance of forces acting on the AWI between the fibers (116),

$$p \quad = -\frac{2\sigma \sin(\theta+\alpha)}{l - d \sin\alpha} \tag{4.3}$$

where the center-to-center distance l is related to the coating's SVFε,

$$l = \frac{\pi d}{4\varepsilon} \tag{4.4}$$

The critical capillary pressure p^{cr} can then be obtained by differentiating Eq. 4.3 with respect to α, setting it equal to zero. Thus, critical capillary pressure across a set of parallel fibers, expressed in terms of SVF and critical immersion angle α^{cr}, can be written as (117,118)

$$p^{cr} = -\frac{2\varepsilon}{d}\frac{\sigma \sin(\theta+\alpha^{cr})}{\pi-4\varepsilon \sin\alpha^{cr}} \tag{4.5}$$

It is worthy to note that as will be shown later our study indicates that an AWI that straddles across two or more layers of fibers most often does not reach such a mechanical breaking point before it deflects laterally so as to meet itself under the fibers (across the symmetry boundaries). At this point, the AWI would probably coalesce with itself and break away from the first layer of fibers, nullifying the SHP characteristics of the coating by submerging the first layer. In such conditions, the capillary pressure right before the AWI coalesces with itself is taken in this work as the critical pressure. Another alternative for critical pressure can also be defined when the distance between fibers are large if the air-water interface touches the substrate before reaching the critical pressure.

4.3 Results and Discussion

4.3.1 Coatings with Orthagonal Fiber Distributions

While a fibrous coating generally consists of many layers, we only considered the first four layers of staggered fibers in our study. This is because, according to our preliminary calculations, for the given range of SVFs considered here, an AWI cannot penetrate into the coating more deeply than four layers before the surface transition to the Wenzel state. Our model represents a cell from a coating comprised of four orthogonally layered fibers. l represents the center-to-center spacing between adjacent fibers in the same layer. The layers have a staggered pattern, in order to better characterize the spaces through which an AWI would penetrate into the coating. The domain has symmetry boundary conditions around the outer fibers.

Figures 4.1a–4.1e show AWI examples obtained from our SE calculations for a coating with an SVF of 10% and a fiber diameter of 10 μm at different pressures. The red and blue fibers have a

Young–Laplace contact angle (YLCA) of 130° and 100°, respectively. The initial setup has the AWI in contact only with fibers on first layer. As pressure increases the AWI penetrates deeper into the pore space between the fibers and wets fibers of the lower layers. As can be seen in Fig. 4.4e, for a given pressure of 4.60 kPa, the AWI has deflected sufficiently to come into contact with the fourth fiber layer without breaking off from the first layer. Figure 4.4f shows the same AWI but from a view that better illustrates the failure condition.

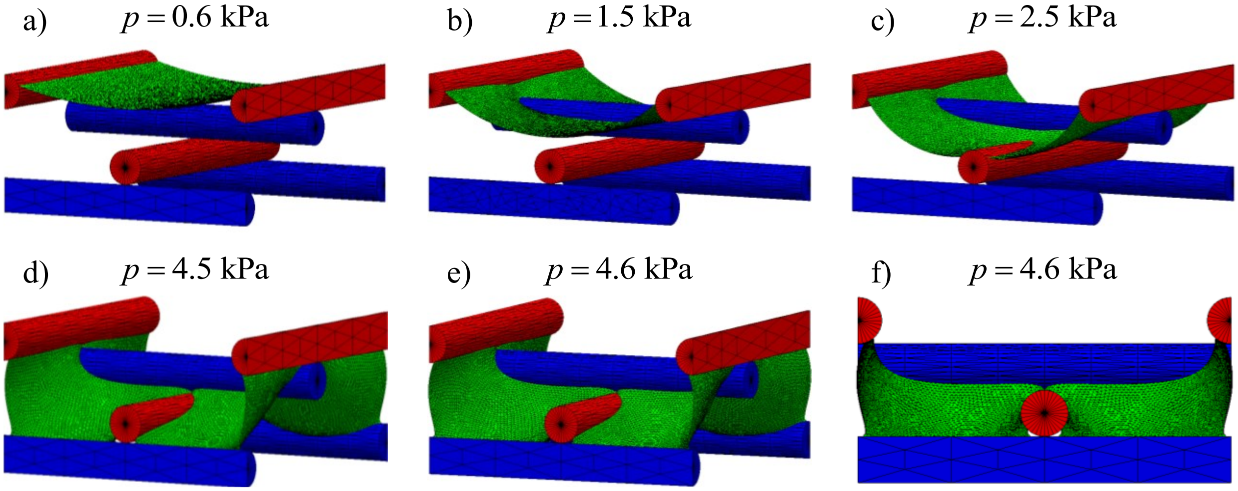

Fig. 4.1 Sample simulation domain after refining mesh density and solving for the minimum energy shape and wetted area calculated by SE at different capillary pressures (a–e). The AWI is at its critical pressure when $p = 4.6$ kPa. This critical AWI is shown in (e) and (f) from two different viewpoints. Note that the AWI is approaching the symmetry boundary in (f).

Figure 4.2a shows critical capillary pressure and wetted area values for coatings comprised 10-μm fibers and a YLCA of 120°. Note that Aw = 1 is the surface area of the substrate as if the coatings were not applied. As shown graphically in the insets of Fig. 4.2a, at low SVFs the AWI is in contact with four fiber-layers at the moment of failure (when the AWI swells laterally to cross the symmetry boundary). At higher SVFs however, the failure occurs when the AWI is in contact with three fiber-layers only, and that is the reason why there is a slight change in the slope of the wetted in Fig. 4.2a for SVFs greater than about 10%. Note in this figure that, critical pressure rises in a relatively linear fashion as SVF increases. This linear rise is in spite of the number of layers in contact with the AWI. It can be seen that, while a less porous SHP coating has a higher critical pressure for a given fiber size and YLCA, this effect comes at the expense of increased wetted area, i.e., potentially more friction with water.

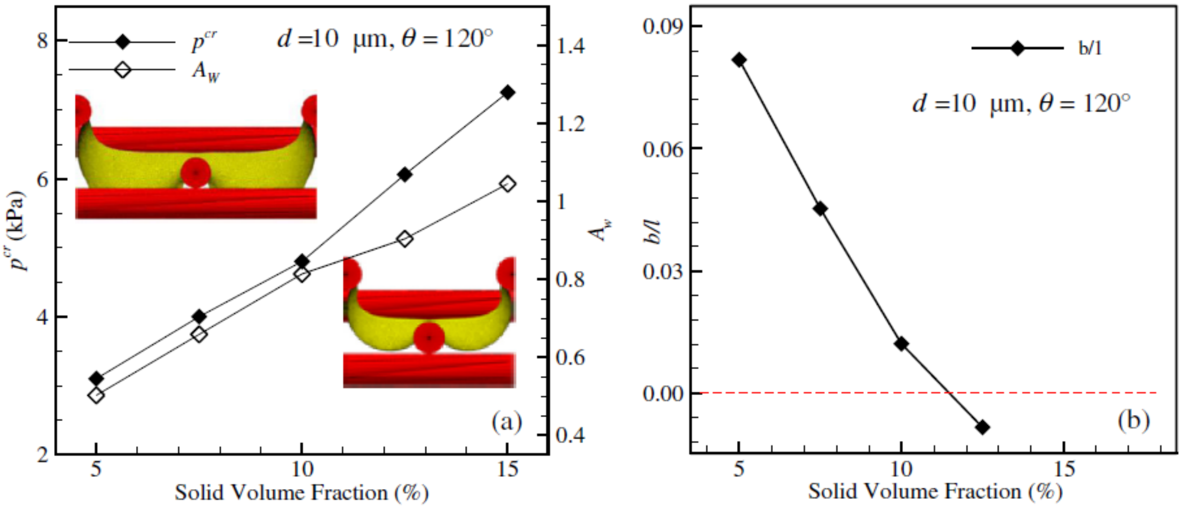

Fig. 4.2 (a) Critical pressure and wetted area fraction as a function of SVF for fibers with equal spacing on all layers. Top inset: AWI is four layers deep before meeting symmetry boundary. Bottom inset: AWI is only three layers deep before meeting symmetry boundary. (b) Dimensionless slip length as a function of SVF at the critical pressure for fibrous coatings with a fiber diameter of 10 μm and an YLCA of 120°.

Figure 4.2b shows the dimensionless slip length as a function of SVF for the same coatings. It can be seen slip length decreases with increasing the coating's SVF. As expected, slip length is smaller for coatings with larger wetted area. Note that Eq. 4.2 is only valid for when $A_w < 1$.

We also examine the performance of orthogonally laid SHP fibrous coatings when alternating layers are comprised of fibers with different diameters. Figure 4.3 shows an AWI example in which fiber layers alternate in size for each layer. For such coatings, SVF must be defined over two layers (one fine fiber layer and one coarse). The ordered nature of such structures allows one to observe that the center-to-center spacing between the coarse and fine fibers l_c and l_f in a unit cell can be related to their corresponding number densities in the whole coating as to $\frac{l_f}{l_c} = \frac{n_c}{n_f}$. Where n_c and n_f are respective number fractions for coarse and fine fibers (e.g., for n_c= 0.1, 10% of all fibers in an area of the coating are coarse fibers).

a)

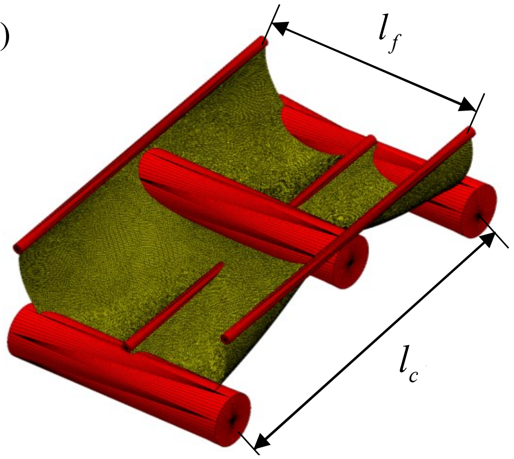

Fig. 4.3 Sample domain for a coating with bimodal fiber diameter distribution. Structure has an SVF of 10%, fine and coarse fiber diameters of 10 and 50 μm respectively, and a coarse fiber number fraction n_c of 0.4.Coating has an SVF of 10%, fine and coarse fiber diameters of 10 and 50 μm respectively, and a coarse fiber number fraction nc of 0.1.

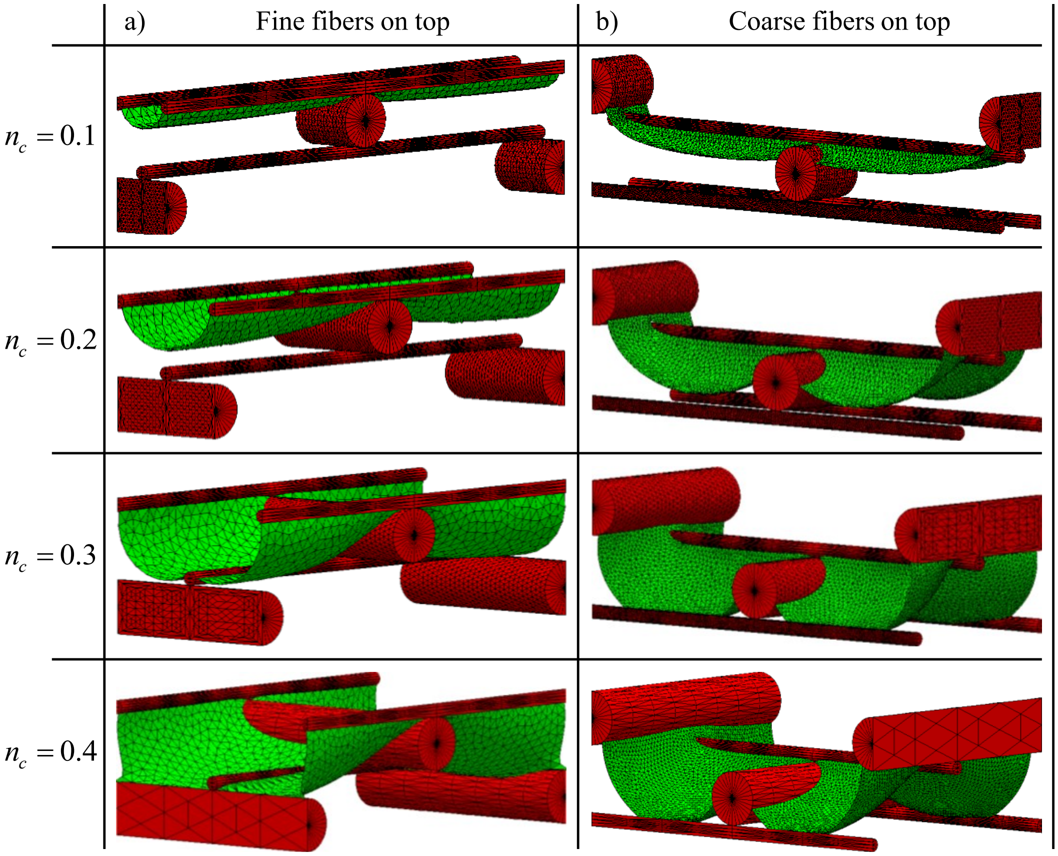

Fig. 4.4 Meniscus configuration at critical pressure for various bimodal coatings varying in coarse fiber number fraction n_c. Coatings have an SVF of 10%, fine and coarse fiber diameters of 10 µm and 40 µm, and an YLCA of 120°.

Figure 4.4a (fine fibers on top) and Fig. 4.4b (coarse fibers on top) show examples of the AWI over bimodal coatings with a coarse-to-fine fiber diameter ratio of R_{cf} = 4 and different coarse fiber number fractions at the moment of failure. It can be seen in Fig. 4.4a that the AWI is in contact with two layers of fibers when $n_c = 0.1$ and 0.2, but comes into contact with the third and fourth layers for $n_c \geq 0.3$. For coatings with the coarse fibers on top (Fig. 4.4b), the AWI remains in contact with three or four layers unless n_c is very close to one (greater than at least $n_c = 0.9$, not shown).

Figures 4.5a–4.5f show the critical pressure, wetted area, and slip length for bimodal coatings with different coarse fiber number fractions and coarse-to-fine fiber diameter ratios. Fine fiber diameter, SVF, and YLCA are all held at 10 µm, 10%, and 120°, respectively. Figs. 4.5a, 4.5b, and 4.5c present the results for when the first layer is made of fine fibers, and Figs. 4.5d, 4.5e, and 4.5f show the results with the coarse fibers on top. For better comparison between the critical pressure of bimodal and unimodal coatings, the critical pressure of the unimodal coating comprised of fibers with a diameter of 10 µm and the same YLCA and SVF (i.e., p^{cr} ≅ 4.8 kPa) is shown in Fig. 4.5a and 4.5d with red dashed line. It can be seen that adding larger fibers (either by increasing R_{cf} or n_c) to a coating comprised of finer fibers results in a decrease in the coatings resistance against elevated pressures. This conclusion is in agreement with our previous observation reported in (116). Figures 4.5b and 4.5e show the corresponding wetted area Aw for each of the coatings shown in Fig. 4.5a and 4.5d (note that the area of the coating's unit cell (i.e., $l_f l_c$) increases with n_c). Recall that for a unimodal coating with an SVF of 10%, fiber diameter of 10 µm, and an YLCA of 120°, a critical wetted area fraction of $A_w \cong 0.8$was reported. This value is shown in Figs. 4.5b and 4.5e for comparison. It can be seen that, adding larger fibers (either by increasing R_{cf}or n_c) to a coating comprised of finer fibers affects the coatings' wetted area fraction in a somewhat more complicated manner.

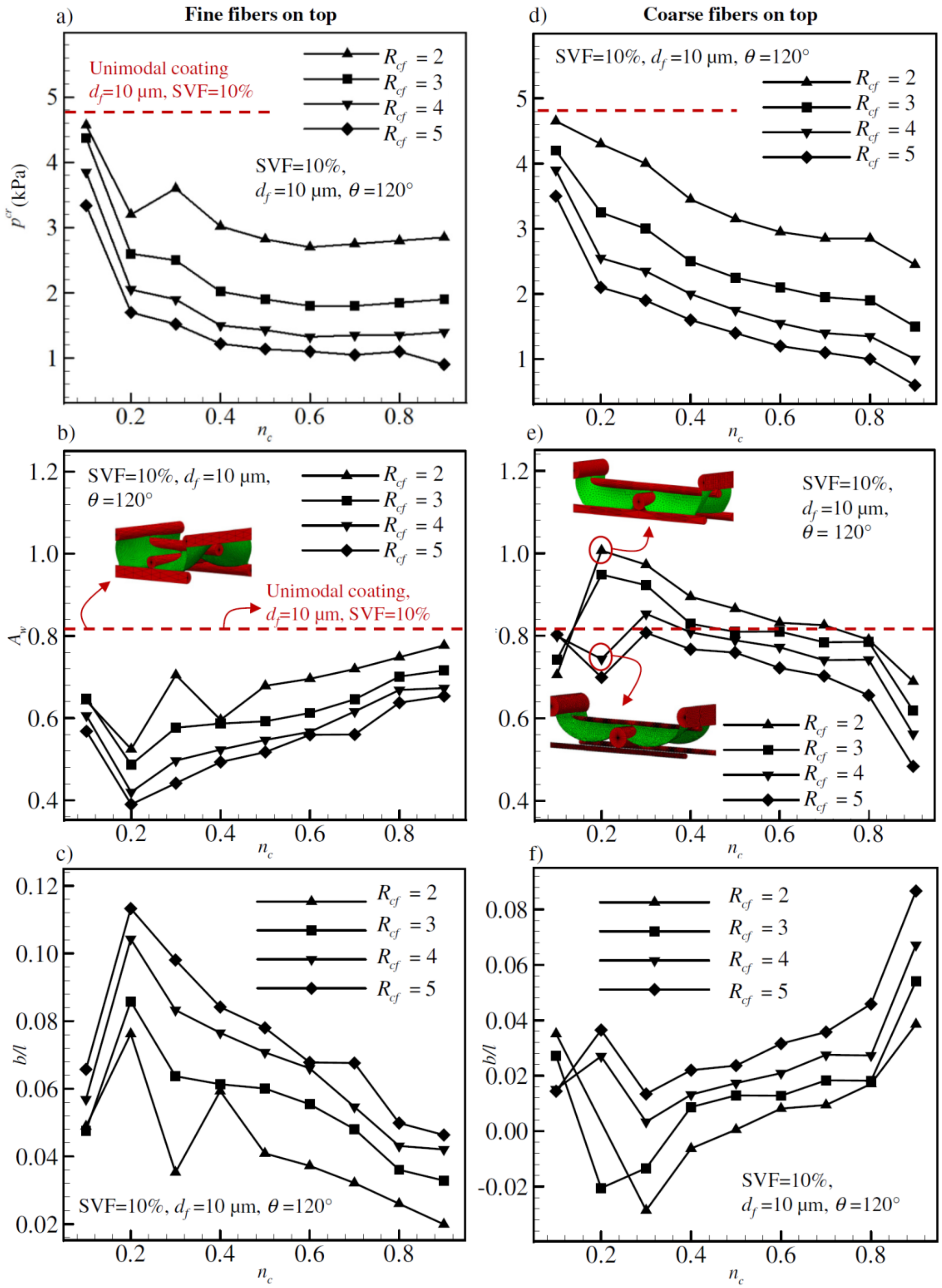

Fig. 4.5 Critical pressure, wetted area fraction, and slip length as a function of coarse fiber number fraction nc for bimodal fibrous coatings varying in fiber size ratio Rcf from 2 to 5 are shown in (a),(b), and (c) for when fine fibers are on the top layer, and (d), (e), and (f) for when coarse fibers are on the top layer, respectively. Other properties shared by all coatings are shown in the figures.

For coatings with the top layer comprised of finer fibers, the critical wetted area is significantly smaller at low coarse fiber number fractions but it increases with n_c as can be seen in Fig. 4.5b. For coatings with the coarse fibers on top, the critical wetted area fraction generally decreases with n_c. Exceptions to this trend are coatings for which the AWI transitions from wetting three layers to wetting four layers when the coarse number fraction is increases (see the AWIs shown in Fig. 4.5b and the inset images in Fig. 4.5e). From these results, one can generally conclude that adding larger fibers to a unimodal coating comprised of small fibers can adversely affect the coating's critical pressure but improve its critical wetted area fraction if the coarse fibers are not added to the first layer. It is worth mentioning that while h^{cr}decreases with increasingR_{cf} Aw is fixed across all applicable scales. Thus, p^{cr} can be raised by using smaller fibers, but Aw will be preserved. The slip length results shown in Fig. 4.5c and Fig. 4.5f correspond to coatings with their first layer on top made of fine and coarse fibers, respectively. It can be seen that slip length is bigger at lower $n_c$values for coatings with the top layer comprised of the finer fibers. On the other hand, for coatings with the coarse fibers on top, dimensionless slip length generally increases with n_c. As explained before, exceptions to these trends are when the AWI transitions from wetting three layers to wetting four layers, as the coarse number fraction is increased.

4.3.2 Coatings with Oriented Fiber Distributions

A fibrous coating generally consists of several layers of fibers on top of each other as discussed before. These fibers generally have random in-plane orientation but they can be made with orthogonal, or slanted orientation respect to another. In this subsection we have a brief look at critical pressure of the coating comprised of fibers with orientation angle γ. It is worthy to note that $\gamma = 0^{\circ}$ will provide the orthogonal coating discussed in previous section.

To model the air-water interface on orientated fibers symmetry boundary condition cannot be used anymore. Therefore, we used periodic boundary condition for these simulation. Here again our simulation results show that the air-water interface fails by touching the neighbouring cell and only four layers of fibers (or less) gets wet at the time of failure.

Figure 4.6 shows the 3D shape of interface achieved by SE simulation for different orientation angle at critical pressure. The air-water interface is shown with green color. Color white marks the interface touches the neighbouring cell.

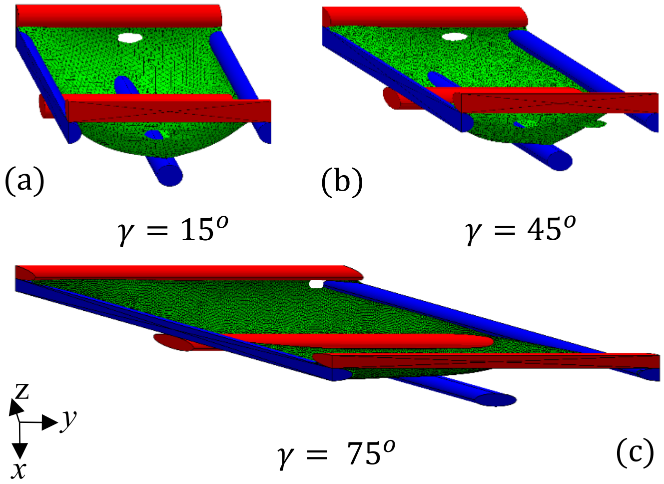

Fig. 4.6 Four layers of fibers with orientation angle of (a) $= 15^{\circ}$, (b) $\gamma = 45^{\circ}$ and (c) $\gamma = 75^{\circ}$.

It can be seeb that as γ increses the white area (weak part of the interface) moves toward the corner of the cell. Our simulation shows that as γ increases critical pressure decreases. The reason for that is as γ increases the diagonal distances between the fibers, therefore fibers can provide less support for the interface.

4.3.3 Wire Screen Coating

Woven screens enhanced with functional surface treatments/coatings have recently be considered as a cost-effective alternative for producing a SHP porous surface in many applications including but not limited to drag reduction, oil–water separation, self-cleaning and anti-icing, and device manufacturing among many others. Similar approach for obtaining an accurate estimate of a screen's critical pressure and wetted area can be used to calculate the drag reduction benefit (slip length) of such surfaces.

Figures 4.7a–4.7d show the simulated AWI over a wire screen under different hydrostatic pressures. The wires have an YLCA of $\theta = 123^\circ$, a spacing of $s_w = 458\ \mu\text{m}$, and a diameter of $d_w = 254\ \mu\text{m}$. At low pressures, the meniscus merely touches the surface of the wires, but it penetrates deeper into the spacing between the wires as the pressure increases. The sagging pressure P_{sag} is defined here as the pressure at which the AWI touches the flat substrate underneath the wire screen (Fig. 4.7c). The breakthrough pressure P_{brk} on the other hand, is defined here as the highest pressure that the AWI can tolerate before the AWI break up allowing water to flow through the screens (the maximum capillary pressure) as shown in Fig. 4.7d.

Note that the dimensions presented here is very different from previous chapters because we used the dimensions which are commercially available.

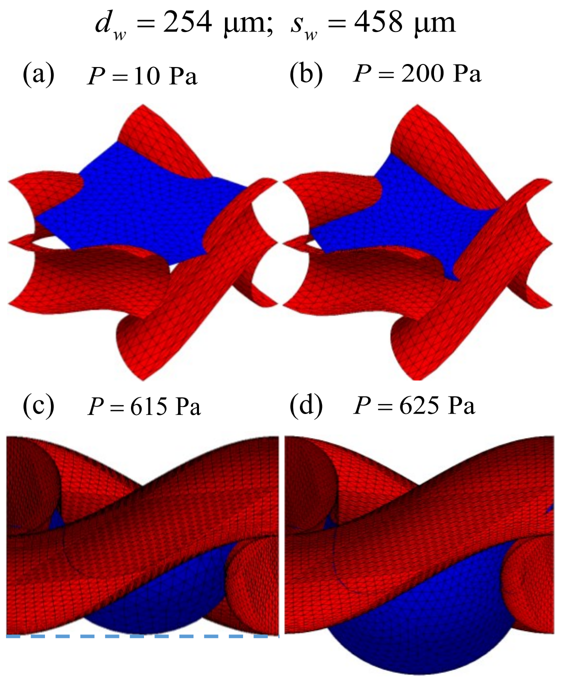

Fig. 4.7: Sample simulation results showing the AWI under different hydrostatic pressures in (a) and (b). Failure due to AWI sagging is shown in (c). Failure due to AWI breakup at the breakthrough pressure is shown in (d). Here $d_w = 254$ μm and $s_w = 458$ μm.

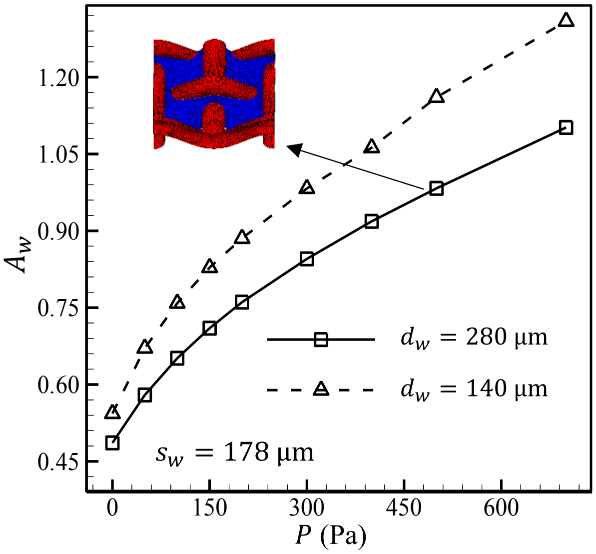

Fig. 4.8: Effects of hydrostatic pressure on wetted area.

Figure 4.8 shows the effects of pressure on wetted area of wire screens with different geometries. The data are generated for constant wire diameter spacing. As expected, wetted area increases with pressure. More interestingly, at a constant pressure (say, $P = 150 \text{ Pa}$), wetted area fraction is found to be larger for screens with smaller wire diameters.

4.4 Conclusions

Our results show that, for a constant fiber diameter as SVF increases both critical pressure and wetted area increase. We also showed that bimodality in fiber size has positive impact on the performance of orthogonal coatings. We also showed that changing the orientation of the fibers from orthogonal to other angles weakens the coating. We also showed that the method presented in this chapter can be used to predict the critical pressure and wetted area of a wire screens. We showed that for a constant wire spacing wetted area is higher for smaller wire diameter.

Chapter 5. On the Apparent Contact Angle and Detachment Force of Droplets on Rough Fibers

5.1 Introduction

Understanding the interactions between a droplet and a fiber is of great importance to many applications. These applications include, but are not limited to, droplet filtration/separation, spray coating, electronic cooling, health and safety, fog harvesting, protective clothing, and medicine (46–48,50,119,120) . A simple manifestation of this effect in nature is the dew formation on spider webs or cactus spines, where life relies on the interactions between a droplet and a fiber in arid climate. Droplet–fiber interactions have been studied in many pioneering studies, and it has been shown that the apparent contact angle (ACA) θ_{app} of a droplet with a fiber can be quite different from the Young–Laplace Contact Angle (YLCA) obtained for a small droplet of the same liquid deposited on a flat surface made from the same material (46–48,50,119,120). Depending on fiber diameter, fiber surface energy, droplet volume, and droplet surface tension, two different conformations have been observed for a droplet deposited on a fiber. The first conformation, the barrel shape, tends to occur for larger droplets (relative to fiber), or for when the YLCA is relatively small. The second conformation, the clamshell, is mostly observed with small droplets, or when the YLCA is relatively high. In the former conformation, the droplet wets the fiber symmetrically while in the latter, the fiber is wetted on one side only. There are also droplet–fiber systems where both of these conformations can be observed (47,49–51,120–123). Roughness has been shown to affect the wettability of a surface. Wenzel proposed a relationship between YLCA θ_{YL} and a droplet's ACA of on a rough flat surface as $\cos\theta_{app} = r\ cos\theta_{YL}$ where r is the ratio of the actual to the projected area of the rough surface (32). However, due to a variety of factors, the measured contact angles may significantly differ from the predictions of this simple relationship, and in fact, predicting a droplet ACA on a rough surface has remained an active area of research for the past decades (see e.g., (59,124–129)). The knowledge gap is even wider when it comes to droplet contact angle on rough fibers (see e.g., (58,119,130–132)), and this has been the motivation for undertaking the work presented here.

The remainder of this chapter is structured as follows. First, we introduce our rough fiber equation and discuss the numerical modeling approach used to simulate the 3-D shape of a droplet on such a fiber (Sec. 5.2). We then present a validation study where we compare the predictions of our numerical simulations with the experiment for a few simple configurations in Sec. 5.3. Our investigations of the effects of surface roughness, fiber diameter, and droplet volume on the shape and ACAs of a droplet deposited on a rough fiber are reported in Sec. 5.4. In this section, we also study the transverse forces required to detach a droplet from a rough fiber for different droplet–fiber configurations. Finally, the conclusions drawn from the work are given in Sec. 5.5.

5.2 Numerical Simulation

The surface energy minimization method implemented in the Surface Evolver (SE) finite element code is used to simulate the 3-D shape of a droplet deposited on a rough fiber. SE has been shown to be accurate in predicting the air–water interface stability (see e.g., (35,36,117)). In this section, we first present the equations for producing a fiber having an arbitrary 3-D roughness, and then derive an equation for the energy of a droplet deposited on such a fiber. Although real roughness is in random shape and arrangement it is impossible to draw universal conclusion from random roughness. Therefore, to investigate the effect of fiber roughness on droplet shape and detachment force we considered a sinusoidal roughness. Consider a fiber in the x-direction with a sinusoidal roughness in the axial and preferential directions, described as

$$R(x,\alpha) - r_f\left[1 + a\sin(\frac{2\pi}{\lambda r_f}x)\sin(\omega\alpha)\right] = 0 \tag{5.1}$$

where r_f is the smooth fiber radius, $R(x,\alpha) = \sqrt{y^2 + z^2}$ is the local radius of the rough fiber at any point, and $\alpha = Arctan\frac{z}{y}$ is angular position. In this equation, a is roughness amplitude, λ is roughness wavelength and $\omega = \frac{2\pi}{\lambda}$ is the angular frequency of the roughness peaks (see Fig. 5.1a). For the sake of convenience we define dimensionless roughness amplitude as $= \frac{a}{r_f}$. SE is used in this study to obtain the equilibrium 3-D shape of a droplet deposited on a rough fiber by minimizing the total energy of the droplet–fiber system. For a single-droplet–single-fiber system, the total free energy E can be written as

$$E = \sigma_{LG}A_{LG} - \sigma_{LG}\int_{A_{SL}} cos\theta_{YL}dA + \int \rho hgdV \tag{5.2}$$

where σ_{LG} is the surface tension of the liquid and A_{LG} and A_{SL} are liquid-gas area and solid-liquid area respectively. Here, h represents the vectorial change in the droplet's centroid position due to body forces (zero in the absence of external forces), g stands for the body force per unit mass, ρ is density of the liquid and dA and dV are area and volume elements respectively .

Our simulations start by placing a droplet with an arbitrary shape, but a fixed volume V, over the fiber and allowing it to evolve to reach an equilibrium shape and position while maintaining a fixed YLCA at the three-phase contact line. To ensure that the results presented here are independent of the choice of the mesh-size considered for the simulations, we made sure that the mesh on the contact line is dense enough to capture the curvature of the fiber (i.e., $\frac{\lambda}{12}$).

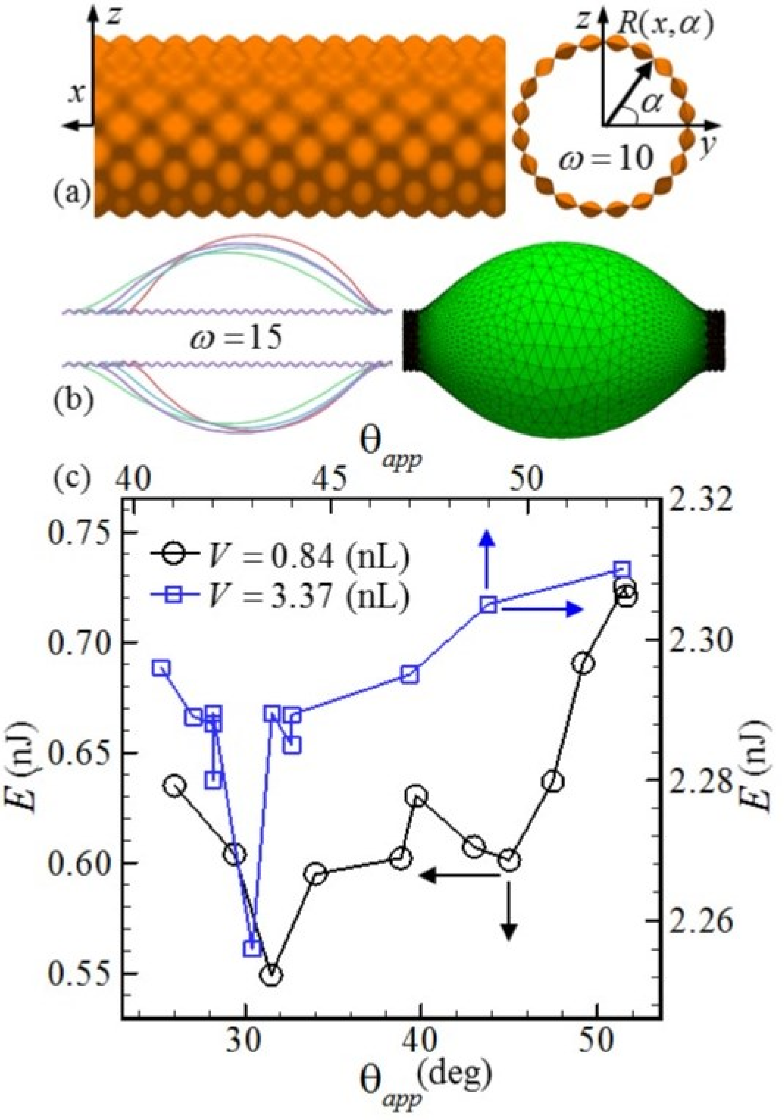

Fig. 5.1 Side and cross-sectional views of our virtual rough fiber is shown in (a). An example droplet shape on a rough fiber with $r_f = 15$ µm, $\theta_{YL} = 30^{\circ}$ and $\omega = 15$ is shown in (b) along with overlaid images of droplet profiles corresponding to different local minimum energies (droplet volume is V =0.84 nL). Droplet

surface energy is plotted versus apparent contact angle in (c) for droplets with volume of V =0.84 nL (black symbols) and V =3.37 nL (blue symbols).

We also calculated the mean curvature of the droplet at each point on the droplet surface (same at all points) for a few cases, and used it in Laplace equation to obtain the droplet pressure. This pressure was then compared with that calculated by SE and very good agreement was observed in all cases.

Figure 5.1b shows an example of our simulation results obtained for a fiber with a radius of $r_f =$ 15 µm, droplet volume of V =0.84 nL, $\theta_{YL} = 30°$, and $\omega = 15$ with the gravitational force per unit mass given as g_z =9.8 N/kg. As was extensively discussed in the literature, there are infinite number of ACAs (each corresponding to a local minimum energy) that a droplet can exhibit depending on the position of its contact line on a surface (59,124–129). Figure 5.1b shows some of the possible shapes that a droplet can retain on a fiber. Figure 5.1c shows the energy of the droplet as a function of ACA for b =0.1 and V =0.84 nL and 3.37 nL. The ACA corresponding to the global minimum energy is then taken as the ACA (32° and 42° for V =0.84 nL and 3.37 nL, respectively, for the case shown in Fig. 5.1). In the remainder of this chapter, we only report the ACA corresponding to the droplet's global minimum energy for each droplet–fiber combination. In the absence of a universally accepted method for measuring droplet contact angle on a fiber, we used the so-called inflection point method to read the contact angles from droplet images (48). It is worthy to note that when the fiber is smooth for some volumes there are maximum two local minimum energy shape i.e., barrel shape and clamshell droplets.

5.3 Experiment

A series of experiments has been conducted for validation purposes, and are reported throughout the chapter whenever possible (for smooth fibers only). The experiments were conducted using smooth Polypropylene (PP) fibers supplied by Minifibers Inc. Two different liquids were tested to obtain a wider range of droplet contact angles. Propylene Glycol (PG) was obtained from Fisher scientific, and Ultra-Low Sulfur Diesel (ULSD) was purchased locally. Surface tension, density, and contact angle with PP are $28\ \mathrm{nN/m}$, $830\ \mathrm{g/L}$ and $10°$ for ULSD and $32.5\ \mathrm{nN/m}$, $980\ \mathrm{g/L}$, and $22°$ for PG, respectively. Note that the contact angle reported here is the contact angle measured on flat surface of similar material.

The same experimental set up as Reference (133) were used for the experiment. The size of the droplets deposited on the fibers was controlled using the syringe approach (133,134). In this method, two additional fibers with the same material as the test fiber were used. The first fiber was partially inserted into the needle of the syringe while the second fiber was curled to form a loop and brought into contact with the tip of the needle. When the syringe plunger is pushed, a droplet with a known volume is formed and was transferred to the looped fiber. When the droplet is trapped inside the loop, it can then be easily transferred to the test fiber upon contact. While this method allows placing small droplets on a fiber fairly accurately, it is still possible to leave a small droplet at the needle's tip or the auxiliary fibers. The droplets were imaged using an Olympus DP25 camera (a 5-mega pixel digital color microscope camera). The droplets' volume were estimated by using a micro-syringe in the experiments and also by weighing the droplet. Since none of these methods is accurate enough for very small droplets, we also used an image-based method for axisymmetric droplets. In this method, the digitized image of the droplet is used to produce a mathematical fit to the upper half of its profile. This mathematical function is then used to obtain the droplet's volume via a simple integration in the axisymmetric domain (135). To make sure that the experiment was repeatable the experiment were done three times, however it was impossible to get the exact amount of volume each time, but the volumes were in close neighborhood of the volume represented here.

5.4 Results and Discussion

In this section, we first investigate the 3-D shape of a droplet deposited on a roughened fiber, and then, we study the forces required to detach the droplet from the fiber in the transverse direction.

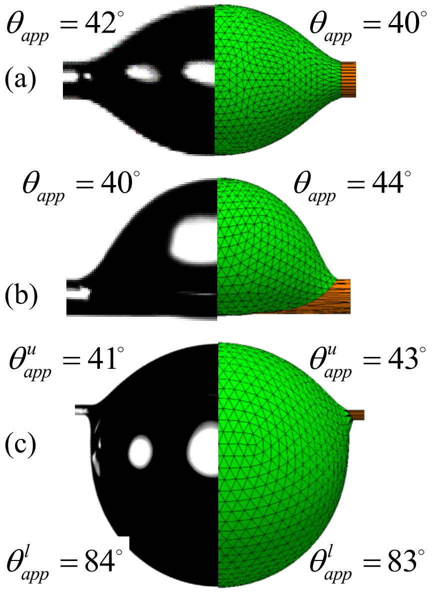

Fig. 5.2 One-on-one comparison between droplet shape and apparent contact angles on a smooth fiber with $r_f = 15$ μm obtained from experiment and numerical simulation for an ULSD droplet with V =1.35 nL and $\theta_{YL} \simeq 10^\circ$ in (a), a PG droplet with V =1.54 nL and $\theta_{YL} = 22^\circ$ in (b), and an ULSD droplet with V =0.215 μL and $\theta_{YL} \simeq 10^\circ$in (c).

5.4.1 Droplet Equilibrium Shape on a Rough Fiber

Generally speaking, the possible droplet shapes on a fiber are the barrel (symmetric and asymmetric) and clamshell shapes. These configurations have been discussed in the form of phase diagrams in many previous studies for droplets on smooth fibers (see e.g., (49)). We start this subsection by first presenting a comparison between experimental and computational data obtained for an ULSD or PG droplet shape on a supposedly smooth Polypropylene fiber in terms of its volume for the purpose of examining the accuracy of our numerical simulations. We then move on to produce a phase diagram for droplet shape on a rough fiber.

Figure 5.2a shows ULSD droplets with volumes of V =1.35 nL, deposited on a PP smooth fiber next to its computational counterpart. The YLCA for ULSD with a flat PP surface was measured to be $\theta_{YL} = 10°$. The ACAs measured from the imaged and simulated droplets are presented in the figure and are in good agreement with one another. Figure 5.2b compares a real and virtual PG clamshell droplets having a volume ratio of V =1.54 nL on a PP fiber with a YLCA of $\theta_{YL} = 22^{\circ}$. The experimental and numerical contact angle values were observed to be 40° and 44°, respectively. Similar comparison is given in Fig. 5.2c for an ULSD droplet with V =0.215 μL. When the droplet volume is large, the gravity affects the shape of the droplet and apparent contact angles at the upper side of the droplet is different from the lower part. The upper and lower ACAs θ_{app}^{u} and θ_{app}^{l} are measured from the experimental images to be 41° and 84°, respectively, which are close to their numerical counterparts of $\theta_{app}^{u} = 43^{\circ}$and $\theta_{app}^{l} = 83^{\circ}$. Note that similar agreement between contact angle values obtained from experiment and numerical simulation has been observed for many other droplet volumes, but not reported here for the sake of brevity.

Increasing the volume of a droplet causes a symmetric barrel-shaped droplet to start becoming asymmetric with respect to the fiber axis due to gravitational effects. To quantify this here, we define an asymmetry factor ε to represent the ratio of the distance between the fiber axis and the upper side of the droplet h_1 and lower h_2 one i.e., $\varepsilon = h_1/h_2$. Figure 5.3a shows the asymmetry factor versus droplet volume for a ULSD droplet deposited on a PP smooth fiber ($\theta_{YL} \approx 10°$) with a radius of $r_f = 15$ µm. In this chapter, we arbitrarily choose an asymmetry factor of ε =0.85 as the lower limit for a barrel shaped droplet to be referred to as symmetric. As can be seen in this figure, experimental and numerical results are in good general agreement with one another. The slight mismatch between the experimental and numerical results seems to originate from 1) the assumption of $\theta_{YL} \approx 10°$ for ULSD with PP surface, and 2) the difficulties in measuring the volume of a clamshell droplet on a fiber accurately.

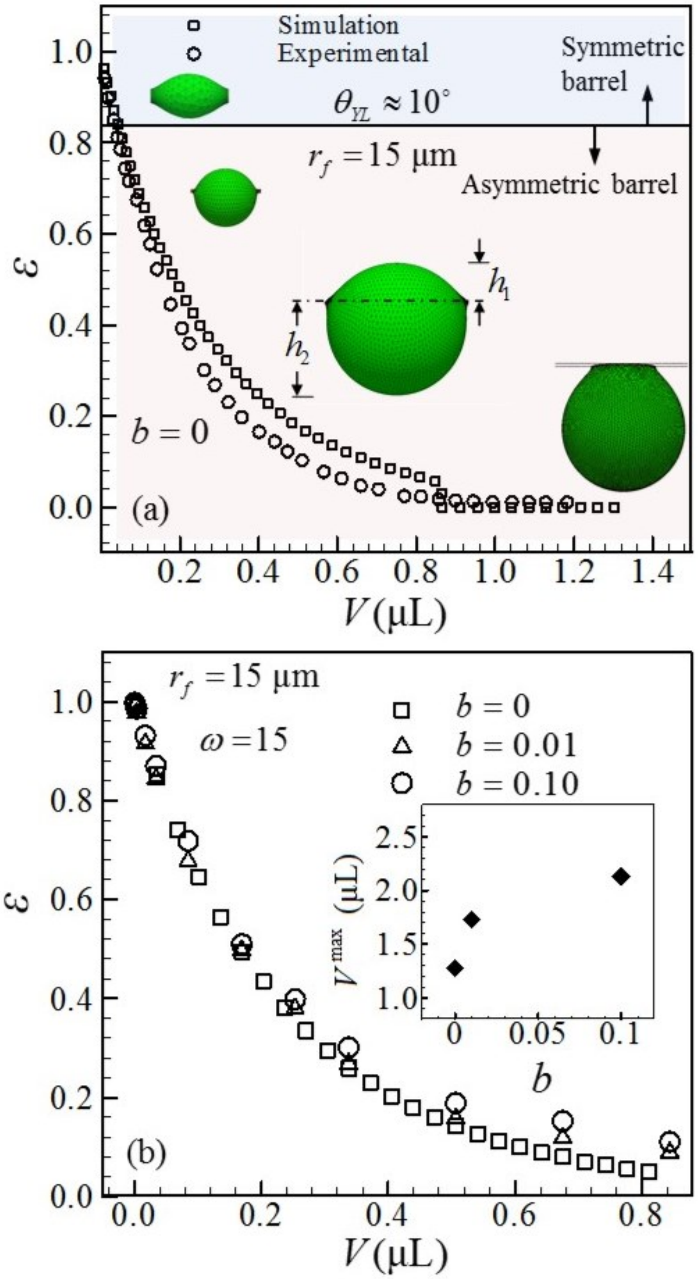

Fig. 5.3 Asymmetry factors from experiment and numerical simulation are shown versus droplet volume in (a) for ULSD droplets on a smooth PP fiber ($\theta_{YL} \simeq 10^{\circ}$, $r_f = 15$ μm). Asymmetry factor is shown in (b) for droplets on rough fibers with a radius of $r_f = 15$ μm and an YLCA of $\theta_{YL} = 30^{\circ}$ but three different roughness amplitudes of b =0, 0.01, and 0.10. The inset figure shows the maximum droplet volume attainable on the same fibers but with different roughness amplitudes.

The sudden decrease (from $\varepsilon \approx 0.1$ to $\varepsilon = 0$) in the data obtained from simulations at a droplet volume of about $V = 0.83$ µL indicates that the asymmetric barrel-shaped droplet has transformed to a clamshell droplet. Figure 5.3b shows the effects of fiber roughness on droplet shape obtained for a fiber with a diameter of $r_f = 15$ µm, a roughness frequency of $\omega = 15$ and YLCA of $\theta_{YL} = 30^\circ$ but different fiber roughness amplitudes of $b = 0$, 0.01 and 0.1. These results indicate that for rougher fibers, the transition from a symmetric barrel shape to an asymmetric barrel shape takes place at a larger droplet volume. In other words, the barrel shape droplet tends to remain symmetric when the fiber is rougher. Interestingly, the largest droplet (maximum volume) that can remain attached to a fiber before falling under gravity increases when the fiber roughness increases (see the inset in Fig. 5.3b). These results are in consistent with Wenzel equation –roughness makes a philic surface more philic-.

Figure 5.4 shows a phase diagram obtained numerically for possible configurations of a droplet on a rough fiber. Here, we considered a fiber with a radius of $r_f = 15\mu m$, a YLCA of $\theta_{YL} = 30^\circ$, and a roughness frequency of $\omega = 15$. In this figure, the squares, triangles, and circles represent the conditions where the possible droplet configurations are symmetric barrel shape, coexistence of symmetric barrel shape and clamshell, and coexistence of asymmetric barrel and clamshell droplets, respectively. Symmetric barrel seems to be the dominant droplet shape when the droplet volume is small or when the fiber roughness amplitude is high. With increasing the droplet volume or decreasing the roughness amplitude (on a relative basis), clamshell shape also becomes a possibility. To quantify the degree of asymmetry in barrel-shaped droplets, the asymmetry factor ε (not applicable to clamshell droplets) is obtained and is presented in Fig. 5.4. It can be seen that

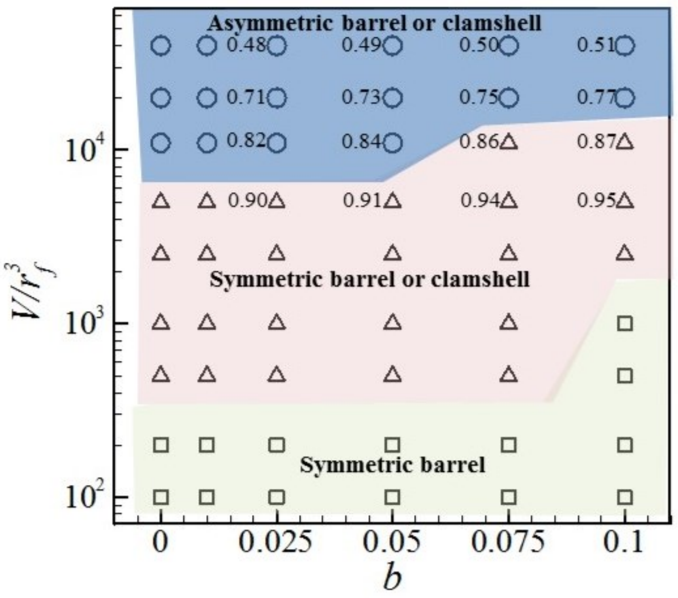

Fig. 5.4 A phase diagram showing different possible conformations for a droplet on a rough fiber. Square, delta, and circle represent symmetric barrel drop, coexistence of symmetric barrel and clamshell droplets, and coexistence of asymmetric barrel and clamshell droplets, respectively. Here, $r_f = 15$ μm, $\omega = 15$ and $\theta_{YL} = 30°$. The asymmetry factor is given next to some of the symbols for comparison.

ε increases with increasing fiber roughness b indicating that a droplet can better retain its symmetric barrel shape on a fiber when the fiber is rough.

5.4.2 Apparent Contact Angle of a droplet on a Rough Fiber

In this subsection, In this subsection, we investigate numerically how droplet ACA on a fiber varies with fiber roughness. Figure 5.5a shows how varying b from 0.01 to 0.1 affects a droplet's ACA on a fiber. It can be seen that ACA decreases with increasing the amplitude of surface roughness for both droplet volumes considered, although the effect seems to be stronger for the smaller droplet. Note also that droplet ACA increases with increasing droplet volume. Droplets forming a clamshell shape are studied in Fig. 5.5b. It can be seen that ACA for a clamshell droplet decreases with increasing fiber roughness. Similar to the results given in Fig. 5.5a, the rate of decrease in ACA is lower for the larger droplet.

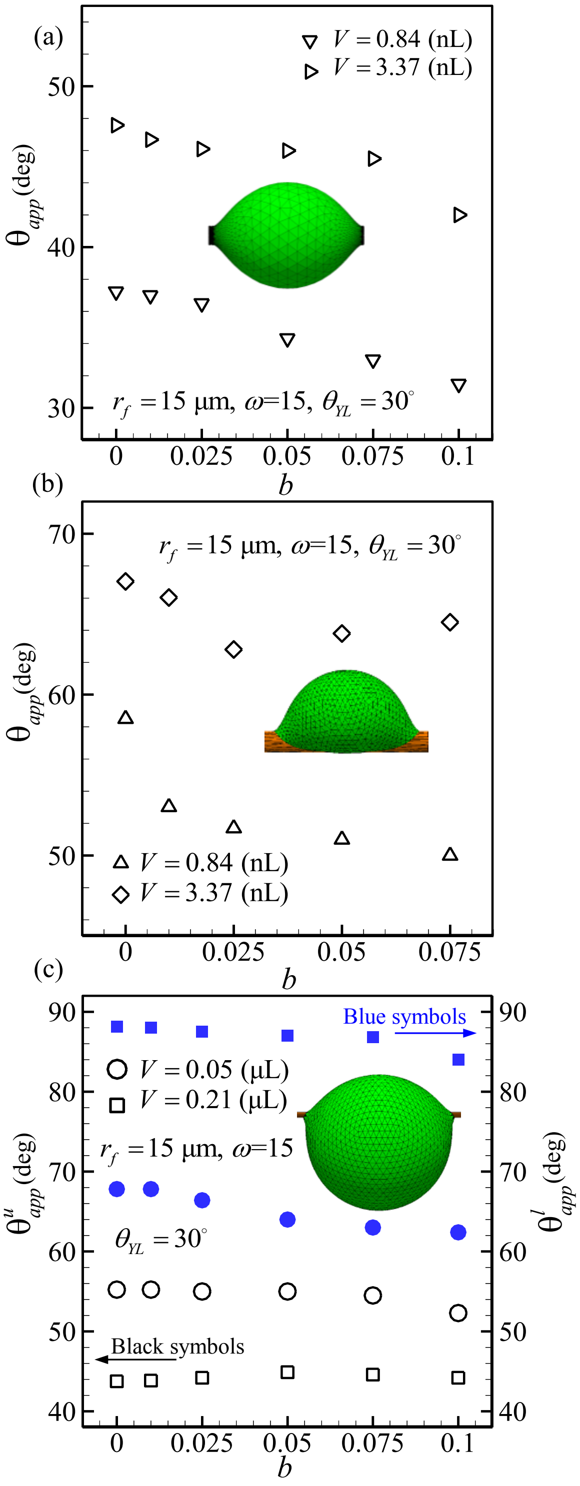

Fig. 5.5 Apparent contact angle is shown versus fiber roughness amplitude for examples of symmetric barrel shaped droplets in (a), clamshell droplets in (b), and asymmetric barrel shaped droplets in (c). For the clamshell droplets both upper (black hollow symbols) and lower (blue filled symbols) apparent contact angles are reported. Here, $r_f = 15\mu\text{m}$, $\omega = 15$, and $\theta_{YL} = 30°$. This figure is intended for color reproduction on the Web and in print.

Figure 5.5b also shows that ACA increases with increasing volume of the droplet on a given fiber. Furthermore, comparing the results given in Fig. 5.5b to those in Fig. 5.5a, one can see that the ACA is higher for clamshell droplets. Figure 5.5c shows that two ACAs can be defined for asymmetric droplets as discussed before: an upper ACA θ_{app}^{u} and a lower ACA θ_{app}^{l} . This figure shows the upper and lower ACAs for two droplets with different volumes versus fiber roughness amplitude. It can be seen that θ_{app}^{l} (blue symbols) slightly decreases with increasing fiber roughness, as increasing fiber roughness works against droplet shape becoming asymmetric. The effect of roughness on θ_{app}^{u} however, seems to be negligible.

To investigate how surface roughness frequency ω can affect a droplet's ACA on a fiber, we considered a barrel shape droplet with a volume ratio of V =3.37 nL in Fig. 5.6.

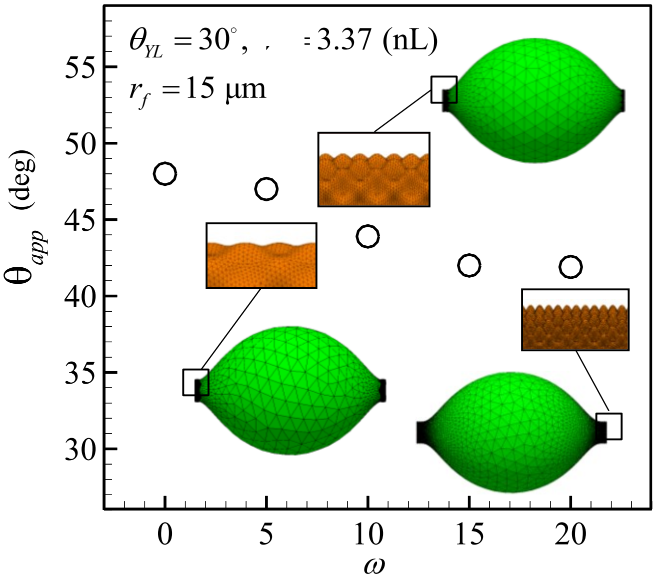

Fig. 5.6 Effects of roughness frequency on apparent contact angle is shown using a barrel shaped droplet with a volume of V =3.37 nL on a rough fiber with a radius of $r_f = 15$μm and a YLCA of $\theta_{YL} = 30°$.

This figure shows the most stable ACA (corresponding to droplets with the global minimum energy) as a function of fiber roughness frequency ω. It can be seen that ACA decreases as ω increases, but the change in ACA tends to become negligible at higher roughness frequencies. This observation is consistent with that reported in (59,124) for the effects of frequency of variation of a surface chemical heterogeneity (or droplet volume relative to heterogeneity length scale) on ACA. Although, Cassie equation is not correct for rough fiber, our simulation shows that at higher frequency the most stable shape of the droplet is independent of roughness frequency. Our numerical simulations indicate that roughness amplitude has generally a greater effect on a droplet ACA than roughness frequency for the range of the dimensions studied in this chapter.

5.4.3 Detachment Force of a Droplet from a Rough Fiber

Our study in this section is aimed at numerically predicting the force required to detach a droplet from a fiber in the direction normal to the fiber axis (see e.g., (54,133,136)). To do this, we applied an external body force on the droplet and obtained an equilibrium shape for the droplet under the imposed external force. We then increased the force incrementally with an arbitrary increment of $\Delta g_z = 9.8$ N/kg (one gravity) until no stable shape could be obtained for the droplet on the fiber. The largest body force under which a stable droplet shape could be obtained plus an increment of Δg_z was then taken as the force required to detach the droplet from the fiber. It should be noted that for the YLCA range considered in our study, it is quite possible for a detaching droplet to break up into a large portion leaving the fiber and a small portion remaining on the fiber (leaving a residue behind on the fiber). With the current simulation method, one cannot simulate the dynamics of droplet detachment (or break up) or the droplet volume after the detachment. The simulated detachment forces in this work correspond to the maximum body forces for which an equilibrium shape was obtained for a droplet on a fiber plus an increment of Δg_z.

Figure 5.7 shows the force required to detach a droplet from a fiber versus droplet volume for different surface roughness amplitudes. The inset in Fig. 5.7 shows a droplet with a volume of V =0.84 nL under different body forces. It can be seen that the droplet's original symmetric barrel shape transforms first to an asymmetric profile and then to a clamshell configuration upon increasing the body force. The droplet eventually detaches from the fiber with an elongated clamshell shape. The simulation results given in Fig. 5.7 indicate that detachment force per unit mass increases with increasing fiber roughness. It can also be seen that detachment force per unit mass is less when the droplet is large, as expected. It is worthy to note that here at first no external force has been added to the droplet i.e., no gravity effect.

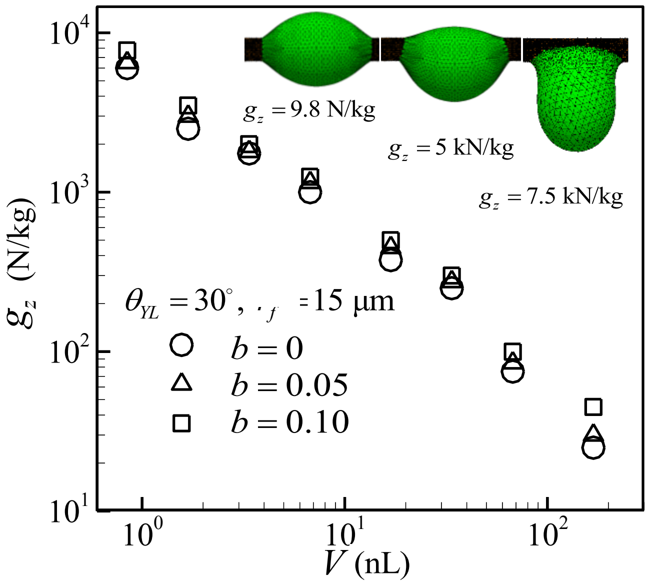

Fig. 5.7 The force per unit mass required to detach droplets with different volumes from a rough fiber with a radius of r_f = 15µm and a roughness frequency of $\omega = 15$, but different roughness amplitudes ranging from $b = 0$ to $b = 0.1$. The inset shows the equilibrium shape under an increasing external body force perpendicular to the fiber axis for a droplet with a volume ratio of $\frac{V}{r_f^3} = 250$ on a fiber with r_f = 15µm and $b = 0.1$.

5.5 Conclusions

The wetting behavior of a droplet deposited on a rough fiber is investigated in this chapter. The results of our study is condensed into a phase diagram that, unlike those reported previously (49), includes the effects of fiber roughness on droplet configurations. Our results indicate that the occurrence of different droplet shape configurations on a fiber (symmetric barrel, clamshell, and asymmetric barrel) depends on fiber roughness, droplet volume, and fiber radius. In particular, it was shown that roughness increases the tendency of a droplet to remain in the symmetric barrel shape configuration as droplet volume is increased. Following the established knowledge for a droplet on a flat surface comprised of 2-D roughness or chemical heterogeneity (126), we quantified the effects of surface roughness on the most stable apparent contact angle (corresponding to droplet's global minimum energy) attainable for a droplet deposited on a fiber with 3-D roughness. It was found that apparent contact angle decreases with fiber roughness, however the effect becomes less significant by increasing the droplet volume relative to roughness amplitude or frequency (126,129).

We also calculated the force per unit mass required to detach a droplet from a rough fiber, and showed that this force increases with increasing fiber roughness or decreasing droplet volume.

Chapter 6. Novel Approach to Measure Droplet Detachment Force from Fibers

6.1 Introduction

Understanding the underlying physics of droplet movement inside fibrous media is a challenging problem of crucial importance to many engineering applications such as liquid–liquid separation, liquid–gas filtration, textiles, microfluidics, water transport in fuel cells, and even water harvesting, to name a few (105,137–142). A simple manifestation of the role of droplet–fiber interactions in nature is the dew formation on spider webs or cactus spines where life in arid climate relies on the capillarity of fibrous structures (130,143). Early studies on the interactions between a droplet and a single fiber have mostly been focused on predicting the equilibrium shape of a droplet (47–49,51,120,123,144). A few studies have also been dedicated to measuring the force needed to move a droplet along a fiber (e.g., (52,53,55,130,145–147)), detach it from the fiber in the perpendicular direction (e.g., (54,122,134,148), see also (121,149)), or detach it from two intersecting fibers (e.g., (133,150–152)). In most of these studies, droplet motion along or away from the fiber(s) has been caused by an air flow, surface wetting heterogeneity, or an external mechanical device like a modified cantilever tip of an atomic force microscope (AFM). The experimental method developed in the work presented here on the other hand circumvents many complications that arise from the use of air or an external device to detach or move a droplet. For instance, when air is used as the driving mechanism to detach a droplet from a fiber, the resulting force can become somewhat dependent on the aerodynamic field around the droplet–fiber assembly (e.g., laminar vs. turbulent, dependent on the flow orientation with respect to fibers) as well as the geometry of the test chamber used for the experiment (53,54,133,134). Likewise, bringing an AFM cantilever tip (even treated with a phobic coating) into contact with the droplet, while being an ingenious approach, may change the original problem of a droplet interacting with a fiber to a new problem of a droplet interacting with a fiber and a cantilever tip (and its associated droplet shape changes) (55,148). The use of AFM microscope for such measurements also comes with additional limitations with regards to imaging the droplet during the experiment, and of course the cost of modifying the cantilever tip, and the inconvenience of working with a sophisticated instrument design for measuring atomic force rather than moving a droplet on a fiber. The method developed in this chapter is based on using ferrofluid droplets in a magnetic field. It is quite easy to implement and is very flexible with regards to varying the direction in which the force measurement is being conducted. Nevertheless, like most other experimental methods, the method proposed here has some limitations as will be discussed later in this chapter.

The remainder of this chapter is structured as follows. First, our experimental setup and the method to measuring the force required to detach a droplet from intersecting fibers are discussed in Sec. 6.2. Our numerical simulations conducted using the finite element Surface Evolver code are described in Sec. 6.3. Our experimental and computational results obtained for detachment of a droplet from a single fiber or from two intersecting fibers are presented in Sec. 6.4 and are discussed in relation to previously reported investigations. This is followed by our conclusions given in Sec. 6.5.

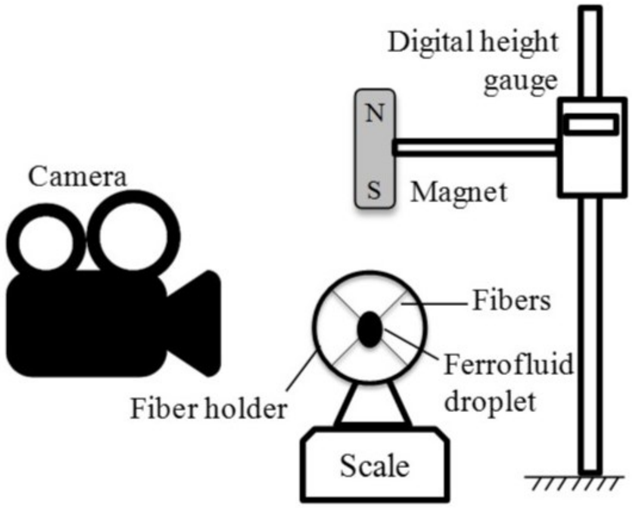

Fig. 6.1 The experimental setup comprised of a 3-D printed fiber holder placed on a sensitive scale and a permanent magnet mounted on a digital height gauge. As can be seen in the SEM image, the fiber used in the experiment seems appears to be smooth.

6.2 Experimental Setup

Our experimental setup is shown in Fig. 6.1. Two pieces of Trilene XL smooth casting fishing line with a diameter of 215 μm were mounted on a holder designed to control the relative angle between the fibers. The holder was placed on a Mettler Toledo AG104 balance with accuracy of 0.1 mg. A New Era NE-300 syringe pump with an infusion rate ranging from 0.73 $\mu\mathrm{L/hr}$ to 1200 $\mu\mathrm{L/hr}$ was used to produce a droplet with the desired volume. The droplets were placed directly on the fiber crossover, and the balance was zeroed after depositing the droplet. The fluid used in the experiment was a water-based ferrofluid (EMG508, Ferrotech, USA) with about 1% $\mathrm{Fe_3O_4}$ nanoparticles (volumetric) and a density of ρ=1.05$\mathrm{g/cm^3}$ at 25℃. Droplet evaporation was minimized by using the draft shields of the balance (no measureable change in droplet weight was observed in the 15-20 seconds duration of each experiment).

A Nickel-plated axially-magnetized cylindrical permanent magnet with a diameter of 4.7 mm and a length of 51 mm (purchased from K&J magnetics) was used to exert external force on the droplets. The magnet was installed on a Mitutoyo Electronic Height Gauges (series 570) and was move toward or away from the droplet during the experiment. Attention was paid to move the magnet normal to the plane of the fibers and align its center with the fiber crossover. The droplets were imaged using a Nikon D3100 camera with an AF-S micro Nikkor 105 mm lens connected to a PC to save the images. The magnet was incrementally moved toward the droplet until the droplet was detached from the fibers. As the magnet pulls the droplet upward, the scale shows negative values on the account of droplet experiencing an additional force (magnetic force) in the direction opposite to the gravity (droplet becomes lighter). At the moment of droplet detachment from the fibers, the scale reading reaches a peak value that is taken here as the force required to detach the droplet. To reduce the error associated with the experiment (either operator or instrument error), each experiment was repeated five times.

6.3 Modeling Droplet Detachment

In this section, we present the numerical method that was used to predict the shape of a droplet and also the force required to detach it from a fiber crossover. For the sake of simplicity, we only consider droplets which wrap around both fibers at their crossover (clam-shell configuration is not considered here). The fibers make an angle α_i with the y-axis where $i = 1$ and 2 refer to the first and second fibers, respectively. Assuming the fibers to be cylindrical, they can each be described mathematically as (see Fig. 6.2),

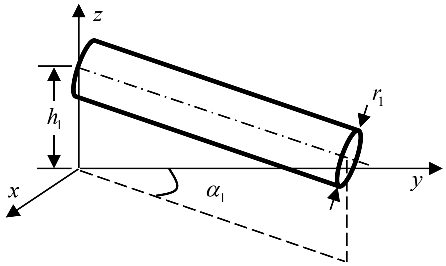

Fig. 6.2 Schematic view of the fiber described in Eq. 6.1.

$$(z - h_i)^2 + (-x \sin \alpha_i + y \cos \alpha_i)^2 = r_i^2 \tag{6.1}$$

where r_i is the radius of the i^{th} fiber. The Surface Evolver (SE) finite element code is used in this chapter to simulate the interactions of a droplet with the fibers (38). SE minimizes the total energy of a droplet-fiber system at its equilibrium state using the gradient decent method (39,47,51,120,153,154). For a droplet deposited on fibers, the total free energy E can be written as

$$E = \sigma_{LG} A_{LG} - \sigma_{LG} \int_{A_{SL}} cos\theta_{YL} dA + \int \rho g h dV \tag{6.2}$$

in which A, σ, θ_{YL} and V are the area, surface tension, Young–Laplace contact angle (YLCA) and volume respectively. The subscript LG and SL denote liquid–gas and solid–liquid interaction, respectively. In this equation, g represents external body force per unit mass, h denotes the vectorial change in droplet's centroid position due to the external body force, and ρ is density of the liquid (35,36,117). Our simulations start by placing a barrel-shaped droplet with a fixed volume at the intersection point of two fibers and evolve to reach equilibrium shape and position. After reaching the equilibrium state (shape and position), an external force (in a desired direction) is exerted on the droplet and its magnitude is increased gradually until the droplet is about to detach from the fibers.

6.4 Results and Discussion

In this section, we study the force required to detach a droplet from a fiber or the intersection point of two crossing fibers. As the surface tension of the water-based ferrofluid used in our experiments was not reported by the manufacturer, we measured it to be 0.0649 ∓ 0.0011 N/m via the pendant droplet method using Drop Shape Analyzer DSA25E. Since the fiber used in our experiment was a commercial fishing line (treated with manufacturer's surface treatment/spin-finish), an additional experiment was needed to find the YLCA of the ferrofluid on the fiber. To do so, two ferrofluid droplets with different volumes of $V = 1.0$ and 0.5 μL, was placed on a single fiber and their shapes were compared to those obtained from SE simulations conducted with different YLCAs but matching droplet volumes. It was found that an YLCA of $\theta_{YL} = 50^\circ$ results in a virtual droplet with a shape that matches the droplet shape from experiment. To do this, droplet images from simulations and experiments were imported to GetData Graph Digitizer software and their profiles were extracted and compared (see Fig. 6.3).

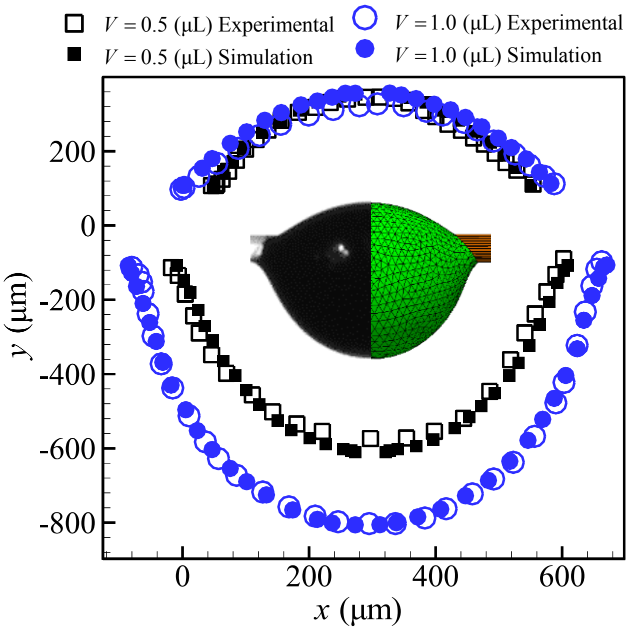

Fig. 6.3 Droplet profiles from simulation and experiment for two different volumes of 0.5 (inset figure) and 1 μL.

6.4.1 Out-of-Plane Detachment Force

We start this section by studying the force needed to detach a droplet from a single fiber. Figure 6.4a shows the shape of a 1.5 μL droplet on a fiber with a diameter of 215 μm and an YLCA of $\theta_{YL} = 50^{\circ}$ obtained from numerical simulation and experiment. The body force here increases from a downward force of 9.8 $\mathrm{N/kg}$ (gravitational force) to an upward force of about 55 $\mathrm{N/kg}$. It can be seen that droplet shape changes as force increases and relatively good agreement can be observed between the predictions of numerical simulation and experimental images. It is important to note that the droplet shape obtained from our SE simulations should not be expected to perfectly match the droplet shape observed in our experiment with a ferrofluid and a magnet. This is because the $\mathrm{Fe_3O_4}$ nanoparticles inside a ferrofluid droplet tend to migrate toward the magnet creating a non-homogenous particle spatial distribution inside the droplet that tends to stretch the droplet profile to a somewhat conical shape (155–158). In contrast, the droplets in our SE simulations treated as a homogenous fluid exposed to a uniform body force like gravity. Despite the acknowledged differences between the nature of droplet shape deformation in the simulations and experiments, the predicted and measured detachment forces (the main objective of the current study) are in good relative agreement (see Fig. 6.4b). The only noticeable discrepancy between the predicted and measured detachment forces is for the case of droplets with a volume of 0.5 μL (about 25%), which we believe it is due to experimental errors involved in capturing the moment of detachment when the droplet is very small (see the percent relative error e in the inset figure). Overall, it can be seen from Fig. 6.4b that, detachment force per unit mass of droplet decreases with increasing the droplet volume.

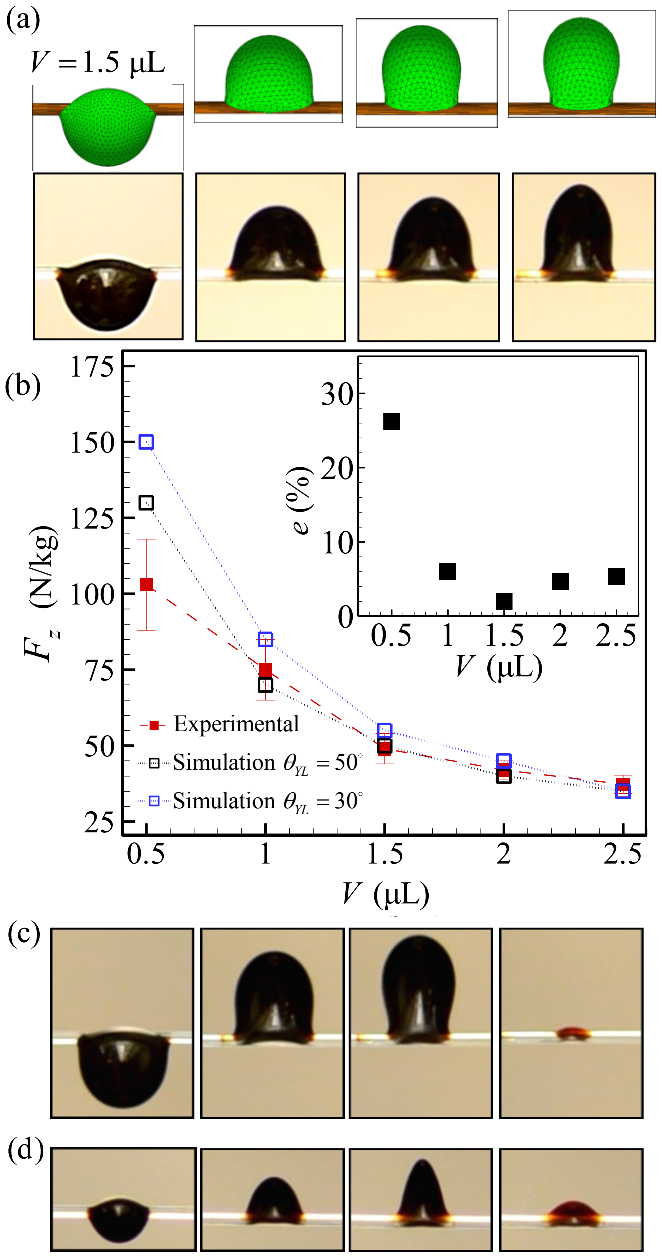

Fig. 6.4 Droplet shapes for different body forces of g = -9.8, 30, 50, and 55 N/kg (from left to right) are obtained via numerical simulation (top) and experiment (bottom) and are shown in (a). Detachment force obtained from experiment and numerical simulation for a single fiber is shown in (b). Droplet shape change in response to magnetic force is shown in (c) and (d) for droplets with a volume of 2.5 μL and 0.5 μL, respectively. The images on the left are taken in the absence of magnetic force (i.e., g = -9.8 N/kg), images on the right show the droplet residual on the fibers after detachment. $\theta_{YL} = 50^\circ$.

It is worth mentioning that for a droplet moving perpendicular to the axis of a single fiber, we did not observe a behavior that could be considered a hysteresis effect (contact angle hysteresis is generally observed and reported for droplet motion along a surface, or along the fiber axis, in our case). This is probably because the forces required for moving a droplet perpendicular to a fiber is much larger than those needed to move the same droplet along the same fiber masking any contact angle hysteresis effect. Nevertheless, to check how a lower contact angle mighty affect our detachment force predictions, we considered a contact angle of 30° degrees (instead of $\theta_{YL} = 50^{\circ}$) and repeated our simulations. As can be seen in Fig. 6.4b, the results obtained with a lower contact angle are still in reasonable agreement with the experimental data, although they indicate that when the fiber becomes more hydrophilic, detaching a droplet from it becomes somewhat harder.

Figures 6.4c and 6.4d show the process of droplet detachment from a single fiber for two droplets with volumes of 2.5 µL and 0.5 µL, respectively. These figures show that a larger percentage of the droplet volume may remain on the fiber after detachment (i.e., a larger residue) when the droplet is smaller. It can also be seen that formation of a conical droplet shape is more probable when the droplet is smaller. The latter is due to the fact that a stronger force per unit mass is needed to detach a smaller droplet and so the magnet has to come very close to the droplet for detachment to occur (i.e., stronger magnetic field gradient acting on the $\mathrm{Fe_3O_4}$ particles).

Figure 6.5a shows a ferrofluid droplet with a volume of 2 µL deposited on intersecting fibers with relative angles of 45 and 90 degrees. SE simulation results are also added to this figure for comparison. The droplets shown in the top row are imaged from top and are taken in the absence of the magnetic force (downward gravity is the only external force). The droplets in the bottom row are imaged from an isometric view and are exposed to upward magnetic force. The minimum force required to detach the droplet from the fiber intersections with different angles is measured for droplets with different volumes and reported in Fig. 6.5b. Predictions of SE simulations are also added to this figure for comparison. Reasonable agreement can be seen between the experimental (red solid symbols) and numerical (black hollow symbols) data.

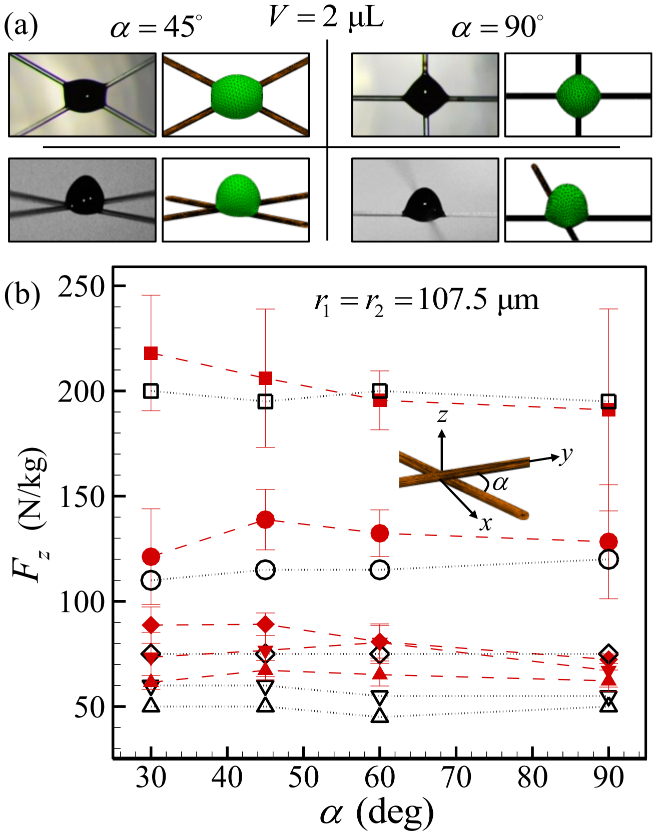

Fig. 6.5 Droplet shape from top (top row) and side (bottom row) views for $\alpha = 45^{\circ}$ and 90° is given in (a). The images in the top row are taken in the absence of magnetic force (i.e., g = -9.8 N/kg) while the images in the bottom row show the droplet influenced by an out-of-plane magnetic force before detachment. Out-of-plane detachment force is shown in (b) as a function of the relative angle between the fibers. Experimental and computational data are shown with red and black symbols, respectively. Square, circle, diamond, gradient, and delta represent droplet volumes of 0.5 μL, 1 μL, 1.5 μL, 2.0 μL, and 2.5 μL, respectively. $\theta_{YL} = 50^{\circ}$.

While the predictions and measurements are in good general agreement, occasional discrepancies of about 15% can be seen for some droplet volume or fiber relative angles, which is believed to be due chiefly to the error in reading the scale at the exact moment of droplet detachment during the experiment. It should also be noted that SE only can predict the equilibrium shape of a droplet. Therefore, the predictions given in this figure are the maximum force for which an equilibrium droplet shape was achieved as the body force was increased incrementally. Obviously increasing the body force with a very small increment increases the accuracy of the predictions but at the expense of CPU time. One should also consider the aforementioned change in the spatial distribution of $\mathrm{Fe_3O_4}$ nanoparticles inside a droplet as another source of error in the experiment as it can affect the shape of the droplet and so the capillary forces holding the droplet on the fiber. Furthermore, Fe_3O_4 distribution within the droplet can be non-uniform and not necessarily mapping the shape of the droplet when the droplet is influenced by a magnet. Predicting the distribution of the within the droplet and their impact on droplet shape is a coupled magnetics-body force-fluid problem, which is beyond the scope of this chapter. In fact, in addition to measuring the magnetic force using our test setup, we also predicted the magnetic force acting on the droplets by measuring the magnetic field and using this information in analytical formulations written for magnetic force (see the Supplementary Materials). The predictions however were about an order of magnitude smaller than expected due perhaps to the above-mentioned intertwined factors.

The results presented in Fig. 6.5b indicate that the in-plane relative angle between the fibers has no significant impact on the out-of-plane force required to detach the droplet from the intersection. This figure also shows that the detachment force per unit mass decreases with increasing the droplet volume. Moreover, comparing the detachment forces given in Fig. 6.5b with those in Fig.

6.4b, it can be seen that the force needed to detach a droplet from two intersecting fibers is higher than that from a single fiber as was observed previously in (151).

6.4.2 In-Plane Detachment Force

In this section, we study the forces required to detach a droplet from intersecting fibers in a given direction lying in the plane of the fibers. We start by considering the case where the external force bisects the fibers' relative angle (symmetric with respect to the fibers). We then move on to the more general case where the external force makes an angle φ with one of the fibers and ψ with the other, while the fibers relative angle is kept constant, i.e., $\varphi + \psi = \alpha$. Figure 6.6a shows side views of a ferrofluid droplet with a volume of 1 μL deposited on intersecting vertical fibers with relative angles of α = 60 and 150 degrees, respectively. SE simulation results are also added to this figure for comparison. The droplets on the top row are taken in the absence of magnetic force (downward gravity is the only external force) while the droplets in the bottom row are exposed to an upward magnetic force. Figure 6.6b shows the detachment force obtained from experiment (red solid symbols) and simulation (black hollow symbols), for different relative fiber angles and droplet volumes. It can be seen that, detachment force increases with increasing the relative angle between the fibers, especially when the droplet is small. This is because at smaller relative angles, the droplet tends to detach from the intersection point to move on to one the fibers before complete detachment takes place. Note that increasing the volume of the droplet does not significantly increase the droplet's contact line (and so the capillary forces), and therefore, the importance of fibers and their orientation becomes less significant when the droplet is larger (detachment force decreases with increasing droplet volume).

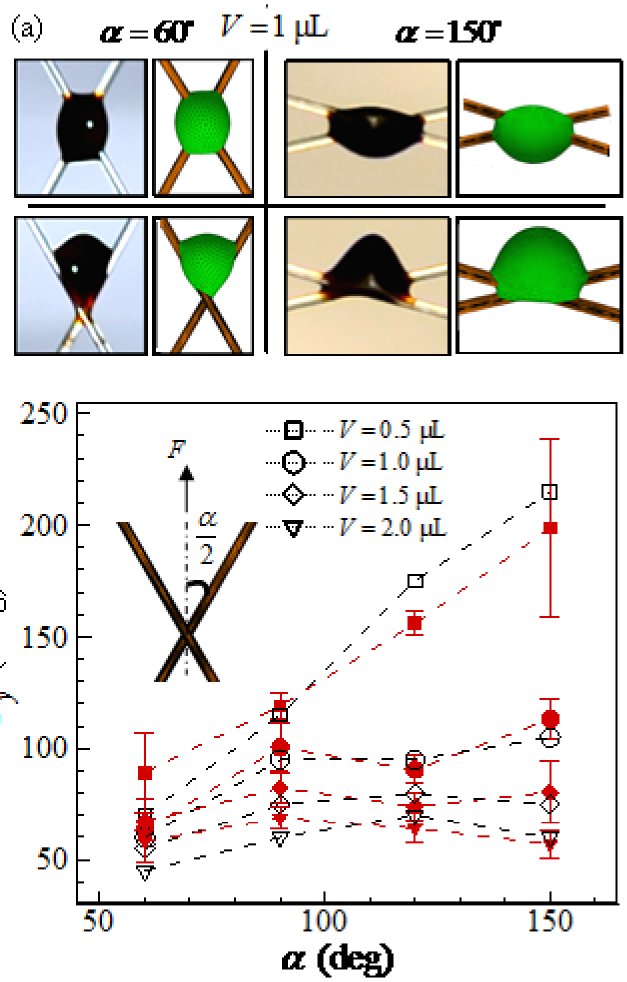

Fig. 6.6 Droplet shape from side view is given in (a) for $\alpha = 60^{\circ}$ and 150°. The images in the top row are taken in the absence of magnetic force (i.e., *g* = -9.8 N/kg) while the images in the bottom row show the droplets influenced by an in-plane magnetic force in the upward direction (direction bisecting the relative angle between the fibers) before detachment. In-plane detachment force is shown in (b) as a function of the relative angle between the fibers. Experimental and computational data are shown with red and black symbols, respectively. $\theta_{YL} = 50^{\circ}$.

Figure 6.7a shows side views of a ferrofluid droplet with a volume of 1 μL on intersecting vertical fibers with a relative angle of α = 90 degrees. The droplets on the top row are taken in the absence of magnetic force (downward gravity is the only external force) while the droplets in the bottom row are exposed to an upward magnetic force in directions $\varphi = 20^{\circ}$ and 40 with respect to one of the fibers. SE simulation results are also added to this figure for comparison. It can be seen that droplet shape is not symmetrical for $\varphi = 20^{\circ}$but it becomes more symmetric as φ tends to 45°(bisector). As mentioned earlier, simulated droplet shapes should not be expected to perfectly match those obtained from experiment due to migration of $\mathrm{Fe_3O_4}$ nanoparticles inside the droplet. Figure 6.7b shows the detachment force for different φ angles for the case of α = 90 degrees. It can be seen that detachment force increases with increasing φ until it reaches a maximum at $\varphi =$ ψ =$\alpha/2$ (bisector). Note that the force required to detach a droplet with a force in the direction φ is the same as that in the direction $\alpha - \varphi$. Figure 6.7c shows the droplet detachment force for when the relative angle between the fibers is of α = 150 degrees. It can again be seen that the force required to detach the droplet increases with increasing φ until it reaches a maximum at $\varphi = \psi$ =$\alpha/2$. Interestingly, at $\varphi = \psi$ =$\alpha/2$ the force is significantly higher than the other values. This is because the droplet tends to move to one of the fibers before detaching from the assembly, and this is easier when φ is smaller (i.e., direction of the force is close to the fiber direction). On the other hand, as the force direction becomes closer to the direction of the bisector, it becomes harder for the droplet to move on to one of the fibers and detach.

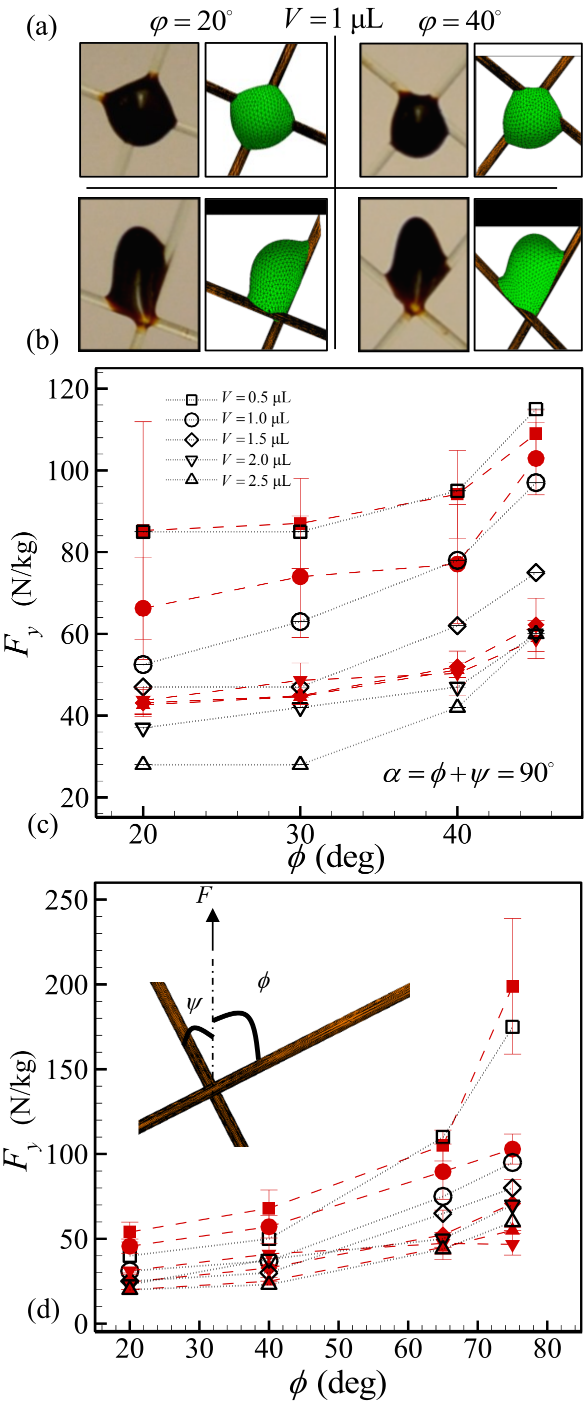

Fig. 6.7 Droplet shape from side view is given in (a) for $\alpha = 90^\circ$. The images in the top row are taken in the absence of magnetic force (i.e., g = -9.8 N/kg) while the images in the bottom row show the droplets influenced by an in-plane magnetic force in the upward direction with $\phi = 20^\circ$ and 40° before detachment. In-plane detachment force is shown in (b) and (c) as a function of ϕ for $\phi + \psi = 90^\circ$and $+\psi = 150^\circ$, respectively. Experimental and computational data are shown with red and black symbols, respectively. $\theta_{YL} = 50^\circ$.

6.4.3 Size Dependence and Industrial Applications

An important application of the study conducted here is droplet filtration from air using a fibrous media (among many other applications). The fibers used in a filter are generally one or two orders of magnitudes smaller in diameter than the fishing line used in our experiment. However, the outcomes of our study can be scaled to droplet-fiber system much smaller than those considered here. Consider a barrel-shaped droplet on a fiber. In the absence of external forces, droplets with the same volume to fiber radius cubed ratio attain the same geometric profile on a fiber[10]. In the presence of external forces (e.g., a magnetic force), Bond number $Bo = \frac{\rho\, g\, r^2}{\sigma}$ (ratio of the external body forces acting on a droplet to the forces generated due capillarity) defines the shape of a droplet on a fiber (159). For a constant Bond number and a constant volume to fiber radius cubed ratio, decreasing the fiber radius from a coarse radius r_c to a fine radius r_f, increases the force per mass required to detach the droplet g by a factor of $\left(\frac{r_c}{r_f}\right)^2$. In other words, the detachment forces reported in this chapter for a large droplet on a large fiber can be post-processed to predict the forces required to detach a small droplet on a small fiber. To confirm this, detachment force for droplets with volumes of 0.05, 0.1, 0.15, 0.2 and 0.25nL deposited on a fiber with a radius of $\mathrm{r_f} =$ 5 µm is predicted using numerical simulation, and compared with that obtained by scaling the results of an identical but larger system (droplet volumes of 0.5,1, 1.5, 2 and 2.5µL on a fiber with a radius of $r_c = 107.5\ \mu m$) by a factor $\left(\frac{r_c}{r_f}\right)^2 = 462.25$ (see Fig. 6.8). Similar scaling properties were observed for a droplet with a clamshell profile on a fiber or intersecting fibers, e.g., near the detachment moment (not shown for the sake of brevity).

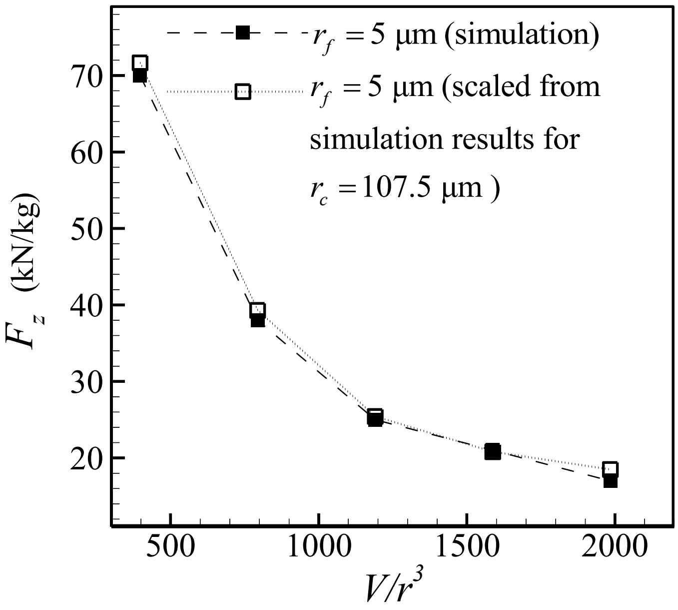

Fig. 6.8 Force per mass required to detach a droplet from a single fiber. The filled symbols show the data obtained from simulating droplets on a fiber with a radius of $r_f = 5$ μm. The hollow symbols represent data produced by scaling the data given in Fig. 6.4b for droplets (with the same volume to fiber radius cubed ratios) on a fiber with a radius of $r_c = 107.5$ μm.

6.5 Conclusions

A novel technique is developed in this work to measure the force required to detach a droplet from a fiber or from a fiber assembly. The method relies on the use of ferrofluid droplets in a magnetic field in a setup placed on a sensitive scale. The proposed method eliminates the need for using air or an external object to move or detach the droplet from the fiber(s), and therefore it allows one to study the capillarity of the droplet–fiber system in a more isolated environment.

The results of our study indicate that the force per unit mass required to detach a droplet from a single fiber is higher when the droplet is small, and it decreases by decreasing the volume of the droplet. Studying intersecting fibers with different relative angle with respect to one another, it was found that the relative angle between the fibers has negligible effect on the force required to detach the droplet in the out-of-plane direction. This angle however, can greatly influence the detachment force in the in-plane direction; increasing the relative angle between the fibers increases the droplet detachment force in the in-plane direction especially for smaller droplets. It was also found that it is harder to detach a droplet from intersecting fibers when the force is applied in the direction of the bisector of the angle between the fibers. Our experimental study was accompanied by numerical simulations conducted using the Surface Evolver CFD code. Good general agreement has been observed between the experimental and computational results.

Chapter 7. Modeling Droplet Equilibrium Shape on Fibers with Trilobal Cross-section

7.1 Introduction

Understanding and controlling droplet movement inside fibrous media is important in predicting the performance of various engineering mechanisms such as liquid–liquid separation, liquid–gas filtration, textiles fabrication, water transport in fuel cells, and water harvesting (137). Early studies on droplet-fiber interactions were focused on obtaining droplet profile and finding a relationship between Young-Laplace contact angle (YLCA) and apparent contact angle (ACA) for barrel shape droplets (axi-symmetric droplet) (48,144). Droplet conformations also attracted a lot of investigation; barrel shape droplet usually form at smaller YLCA and higher droplet volume while clamshell droplet (droplet sits only on one side of the fiber) forms at larger YLCA and smaller volume (160). However, both barrel shape and clamshell droplets may coexist depending on YLCA, surface tension, fiber diameter and droplet volumes (49). More recent studies are focused on finding the force required to move a droplet along a smooth fiber, detach it from smooth or rough fibers and detach it from two intersecting smooth fibers (52–55,130,134,145,151).

Although circular fiber is the most common shape manufactured by synthetic fiber producers, other shapes such as elliptical, lobed, and wedge-shaped cross-sections, are beginning to emerge for a variety of reasons—performance, bulkiness, tactility, processing, etc. (161,162). Filters made from these various fibers may be configured as pads, pleated papers, bonded webs, nettings, or composites (163–167). The only research on droplet-fiber interaction on non-circular fibers considers wedge-shaped cross-sections (119) but does not explain the effect of the shape of the fiber –e.g., number and size of the wedges- or volume of the droplets on fibers' wettability explicitly. Our objective in this work is to highlight the importance of a fiber's cross-sectional shape on ACA and droplet detachment force from the fibers. We predicted the 3D shape of the droplet and ACA of a droplet on a trilobal fiber. We also calculated the force required to detach the droplet from a trilobal fiber for different lobe height and fiber orientation.

The remainder of this chapter is structured as follows. First, we introduce the numerical modeling approach conducted to simulate the 3D shape of the droplet on trilobal fiber in Sec. 7.2. Our investigations of the effects of lobe height and droplet volume on the shape and ACA(s) of droplet deposited on a trilobal fiber are reported Sec. 7.3. In this section, we also study the force required to detach a droplet from a trilobal fiber for different droplet sizes. Finally, the conclusions drawn from the work are given in Sec. 7.4.

7.2 Modeling Droplet Detachment from aTrilobal Fiber

The numerical simulations presented in this paper are conducted via Surface Evolver (SE) code. SE is a finite element code which minimizes the energy of surfaces formed by surface tension and other energies subjected to various constraints (38). SE is used in this study to obtain the equilibrium 3-D shape of a droplet deposited on a trilobal fiber. Consider a fiber with its centerline placed on the *y*-axis having a radius that is described by a sinusoidal wave, as shown in Fig. 7.1,

$$R(\alpha) = r[1 + a\ \sin(\omega\alpha + \varphi)] \tag{7.1}$$

where R is the circular radius of the fiber, $R(\alpha) = \sqrt{x^2 + z^2}$ is the local radius of the trilobal fiber at any point, $\alpha = Arctan\frac{x}{z}$ is angular position, and φ is azimuthal orientation with respect to x-

axis -perpendicular to gravity direction**.** The number of lobes is given with ω, which in the case of a trilobal fiber is set equal to 3. The parameter a in Equation 1 controls the lobes' height as can be seen with an example in Figure 7.1b for a trilobal geometry with $r = 15$ μm and $\varphi = 90^{\circ}$, but a varying from 0 to 0.4.

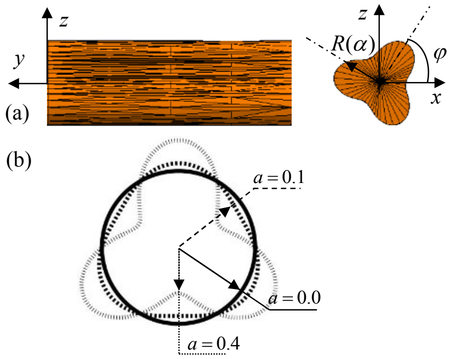

Fig. 7.1 (a): Side-view and cross-sectional view of a trilobal fiber. (b): Overlap of cross-sectional view of the fibers with different lobe height.

For a single-droplet–single-fiber system, the total free energy can be written as

$$E = \sigma A_{LG} - \sigma \int_{A_{SL}} cos\theta_{YL} dA + \int \rho hg dV \tag{7.2}$$

where σ is the surface tension and the subscripts LG and SL stand for liquid–gas and solid–liquid interfaces respectively. In this equation, h represents the vectorial change in the droplet's centroid position in response to a body force (zero in the absence of external forces). A, g, ρ, and V stand for area, body force per unit mass, liquid density, and the volume of the droplet, respectively. To find the equilibrium shape of a droplet on a fiber, an arbitrary initial shape with constant volume

V is considered for the droplet, and its shape is allowed to evolve as the systems' free energy is being minimized iteratively. The input to the simulations is YLCA at the three-phase contact line as well as the surface tension and density of the liquid (in addition to droplet volume).

To ensure the that the curvature of the lobes (i.e., $\frac{r}{2\omega}$) is accurately captured in the simulations, the mesh density was increased by a power of 2 near the tip of the lobes. We also calculated the mean curvature of the droplet at each point H on the droplet surface to make sure that the simulation results satisfy the Laplace equation $P = \sigma H$ (i.e., the pressure P obtained from the Laplace equation matching that obtained from SE simulations).

7.3 Results and Discussion

In this section, we present how lobe height may affect the shape and apparent contact angle of a droplet on a trilobal fiber ACA and the force required to detach the droplet. Here, we used Ultra-Low Sulfur Diesel (ULSD) with a surface tension of $28\ \mathrm{nN/m}$ and a density of $870\ \mathrm{g/L}$. We consider a fiber with a YLCA of $\theta_{YL} = 30^{\circ}$ and a radius of $r = 15$ µm.

7.3.1 Droplet Equilibrium Shape and Apparent Contact Angle

As explained before, the barrel and clamshell conformations are the two primary shapes expected from droplets deposited on a fiber. Under the influence of gravity however, a symmetric barrel-shaped droplet will become asymmetric with increasing the droplet volume.

We start this section by studying the effects of lobe height on a droplet's ACA. As expected, ACA varies around the perimeter of a trilobal fiber (see Fig. 7.2a). Figure 7.2a also shows possible planes that can go through the cross-section of the fiber to define ACA. Here planes of $z = 0$, $z =$

$x\tan\alpha$ and $x = 0$ is shown as examples. Before measuring ACA for each of these planes it is worthy to note that each of these plane cuts the droplet in upper and lower part; which results in two separate ACA: $\theta_{app}^{u}$and θ_{app}^{l} as shown in Fig 7.2b. We studied the variation of the ACA along the perimeter of trilobal fibers with lobe heights $a = 0.4$ having identical $r = 15$ µm, $\theta_{YL} = 30^{\circ}$, φ=90° and $V = 0.84$ nL. We found that that although $\theta_{app}^{u}$and θ_{app}^{l} are not equal, the change in $\theta_{app}^{u}$and θ_{app}^{l} is negligible. For this case ACA is $28^{\circ} \pm 1.85^{\circ}$. Hereon we only will present ACA of $x = 0$ plane because with the gravity being in the negative z-direction, one can expect the major ACA variations to take place in this plane when the droplet volume increases.

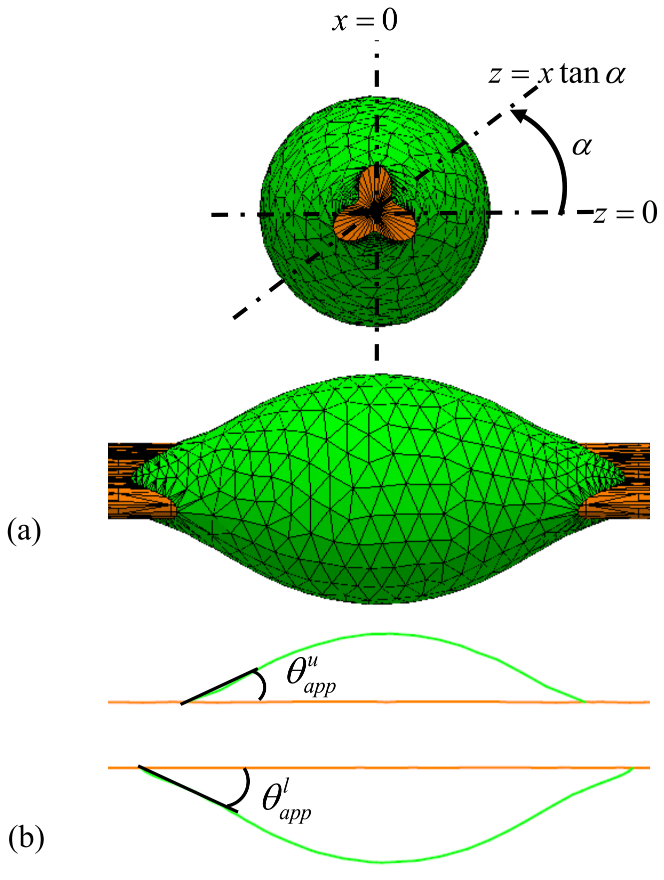

Fig. 7.2 (a): Different plane going through the droplet. (b): upper and lower apparent contact angle obtained by plane of $x = 0$.

Figure 7.3a shows that as lobe height increases ACA decreases. This finding is consistent with Wenzel's finding: roughness makes a philic surface more philic. This figure also shows the small effect due to change in φ. It is worthy to note that for the range of the volume used in this figure the droplet is barrel shape and the difference in ACA due to φ is because of the difference in fiber axial intersection shape with the plane $x = 0$.

To explain why ACA increases with increase in lobe height we report three-phase contact line and solid liquid area. For the sake of convenience we define non-dimensionalized contact length L and wetted area A_w as the ratio of the same parameter of a trilobal fiber to that of circular fiber. Figure 7.3b shows the change in L and A_w as a function of lobe height. As can be seen in this figure both L and A_w increase as lobe height increases. The increase in A_w can explain the increase in ACA in terms of Wenzel equation.

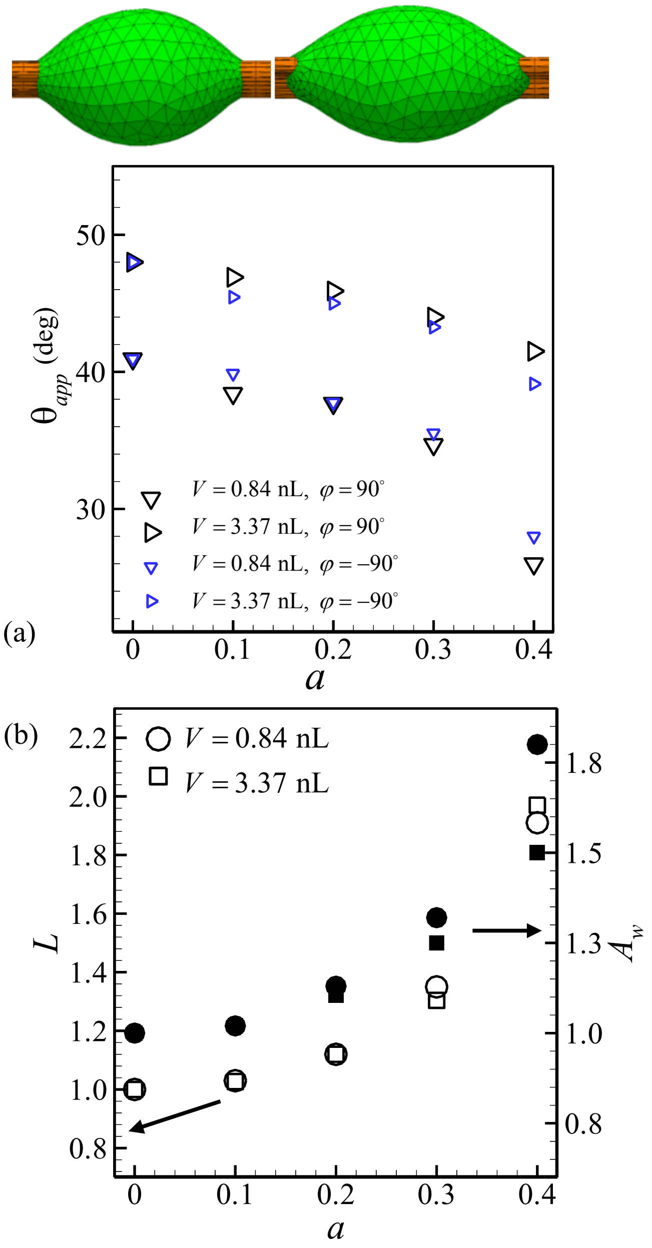

Fig. 7.3 (a): Apparent contact angle is shown versus fiber lobe height for droplets for barrel shape droplet with $\varphi = 90°$ (black symbols) and $\varphi = -90°$(blue symbols). (b): The change in contact line and wetted area of the droplet as a function of lobe height is shown. Here $V = 0.84$ nL and 3.37 nL, $r = 15\mu\text{m}$ and $\theta_{YL} = 30°$.

Figure 7.4a shows the shape of the droplet with $V = 0.84$ nL on a trilobal fiber for $\varphi = 90^{\circ}$ (upper) and $\varphi = -90^{\circ}$ (lower). It can be seen that the position of the droplet is greatly affected by φ which influences ACA with plane $x = 0$ significantly. The change in ACA as a function of lobe height are shown in Fig. 7.4b. This figure shows that as the lobe height increases ACA decreases. Here again, this finding is in agreement with Wenzel equation i.e., roughness makes a philic surface more philic. This figure also shows that the trend is the same for different φ. In addition, this figure shows that when volume of the droplet is higher the effect of lobe height becomes smaller. The reason for that can be explained in the relative size of lobe height to the droplet. When droplet has higher volume, the lobe height becomes comparatively smaller which has smaller effect in ACA.

Two ACA can be defined for an asymmetric droplet as well; upper and lower apparent contact angles θ_{app}^{u} and θ_{app}^{l}. Figure 7.4c shows the upper and lower apparent contact angles for droplets with volume of $V = 54$ nL and 216 nL hanging from fibers with different lobe heights. It can be seen that both θ_{app}^{l} (empty symbols) θ_{app}^{u} (filled symbols) are almost constant as lobe height increases. As explained before when droplet is large the lobe height becomes comparatively smaller which has smaller effect in ACA. The effect of φ has also shown in this figure (blue) and found to be trivial because the size of the droplet is much larger than the fiber so that the fiber shape cannot affect the droplet shape.

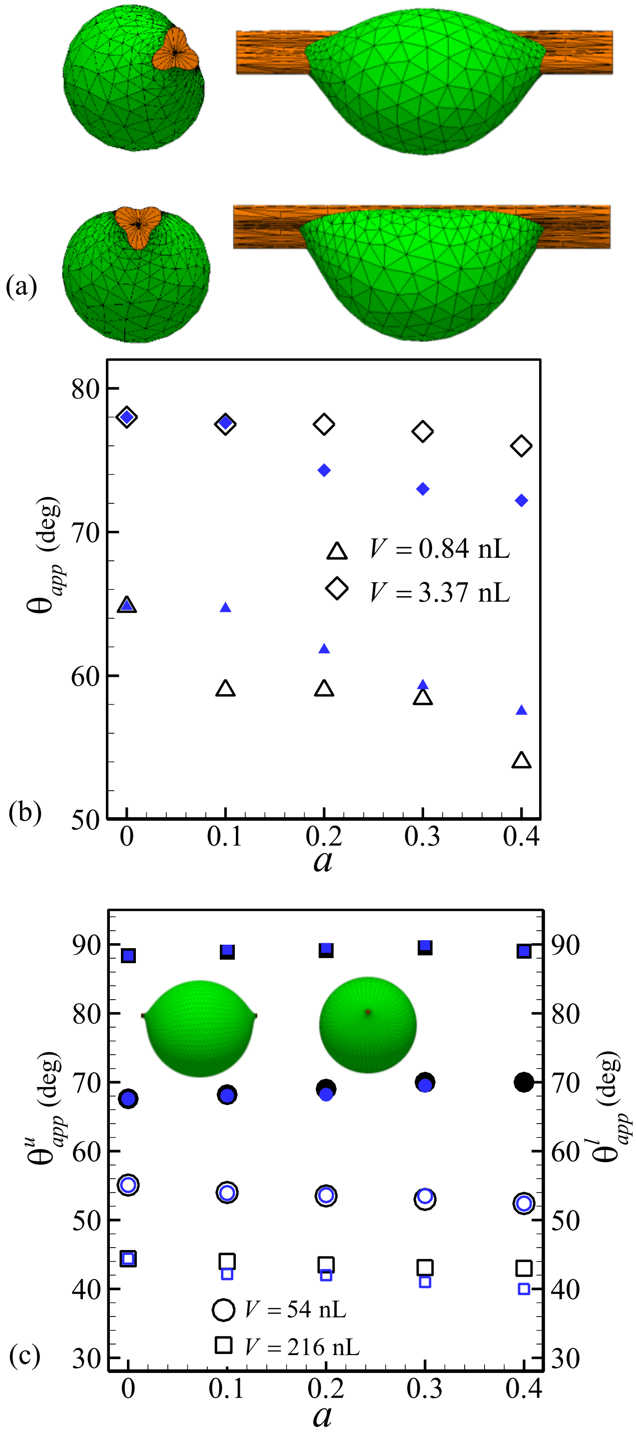

Fig. 7.4 (a): The shape of a clamshell droplet with $V = 0.84$ nL on a trilobal fiber with $a = 0.3$ is shown for two different φ. (b): Apparent contact angle is shown versus fiber lobe height for droplets with $= 0.84$ nL and 3.37 nL for clamshell droplet. (c): Upper (hollow symbols) and lower (filled symbols) apparent contact angles are shown versus fiber lobe height for droplets with $V = 54$ nL (circle) and $V = 216$ nL (square). Here $\varphi = 90°$ (black symbols) $\varphi = -90°$(blue symbols), $r = 15$µm and $\theta_{YL} = 30°$.

7.3.2 Droplet Detachment Force

In this section, we calculated the force required to detach the droplet. It is worthy to note that our numerical method is only able to simulate the equilibrium shape. Therefore we reported the maximum force at which the droplet can be found in equilibrium state as the force required to detach the droplet.

Figure 7.5a shows the force per mass required to detach a droplet from a trilobal fiber for different volumes. It can be seenthat as the volume increases the force per mass required to detach the droplet decreases. This figure also shows the effect of lobe height and φ on detachment force. For a constant volume and $\varphi = -90^{\circ}$ as lobe height increases detachment force also increases. However, this effect will gets smaller as volume increases because the relative size of the lobe height to the size of the droplet become insignificant at higher volume. On the other hand for $\varphi = 90^{\circ}$, the force required to detach the droplet is not significantly different from smooth fiber even at smaller volume. Therefore, one can conclude that detachment force is a strong function of φ at small volumes but as volume of the droplet increases the effect of lobe height and φ becomes less significant. Figure 7.5b and 7.5c shows clamshell droplets with $V = 0.84$ nL on a fiber with $\varphi = 90^{\circ}$ and $\varphi = -90^{\circ}$respectively. It can be seen that for $\varphi = 90^{\circ}$ the droplet is at the side of the fiber at gravitational force but at higher force before the detachment it moves bellow the fiber and becomes symmetric with respect to z-zxis. Comparing fig. 7.5a and 7.5b shows that the solid-liquid area of $\varphi = -90^{\circ}$is higher so as the detachment force. This explains why at smaller volume Fig. 7.5a shows higher detachment force for $\varphi = -90^{\circ}$.

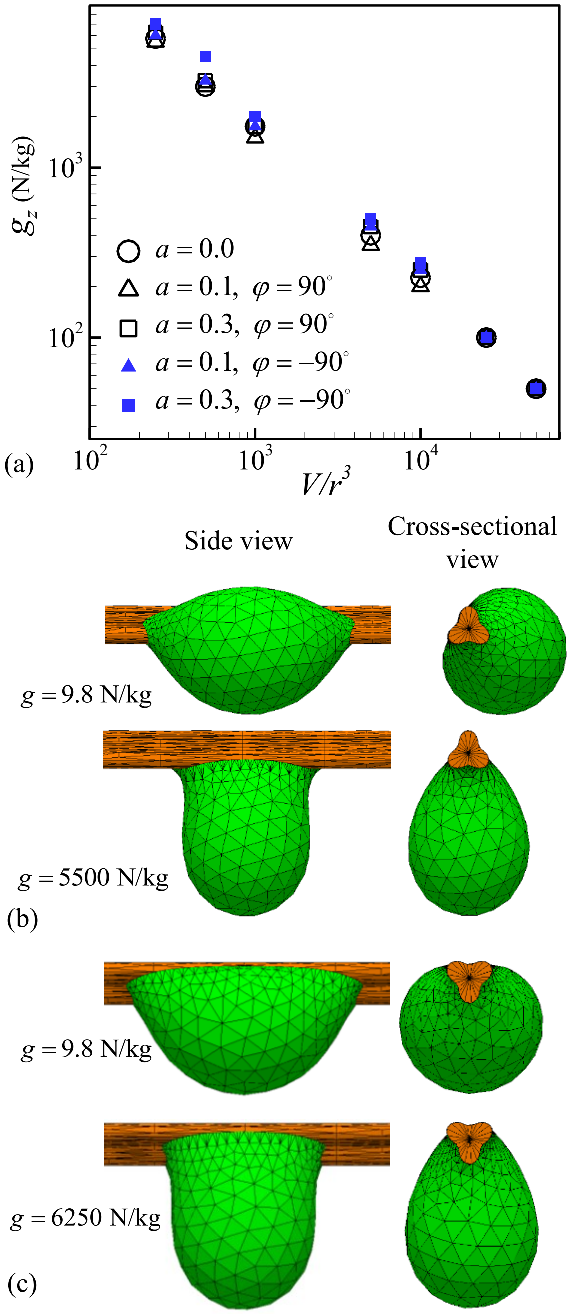

Fig 7.5 (a):The maximum force per unit mass required to detach droplets with different volumes from a fiber with $r = 15\mu\text{m}$ but different lob heights ranging from $a = 0$ to $a = 0.3$ are given for an YLCA of $\theta_{YL} = 30°$ for $\varphi = 90°$ (black symbols) and $\varphi = -90°$(blue symbols). The shape of a $V = 0.84$ nL droplets under gravity and maximum force before detachment is shown for (b) $\varphi = 90°$ and (c) $\varphi = -90°$.

7.3.3 Spreading Droplet

Carroll reports that for a wedge-shaped cross-section with semi-angle α (see Fig. 7.6a), the droplet tends to spread axially over the cylinder surface if $\theta_{YL} < 90 - \gamma$ [23]. We conducted some simulation to find the validity of this assumption for trilobal fiber. For a trilobal fiber with $a = 0.4$ we can assume $\gamma = 60^{\circ}$ (Fig. 7.6b). In the previous sections we used $\theta_{YL} = 30^{\circ}$ and showed that droplets with such YLCA exist on a trilobal fiber. On the other hand for a trilobal fiber with $a = 0.1$ we can estimate $\gamma = 90^{\circ}$ (Fig. 7.6c) therefore all the droplets should be stable. This is also in agreement with our simulation results. It is worthy to mention that we were not able to conduct the simulation for $\theta_{YL} = 30^{\circ}$ and $a = 0.5$ because as Fig. 7.6d shows γ ia about 45° and the droplet spreads on the fiber.

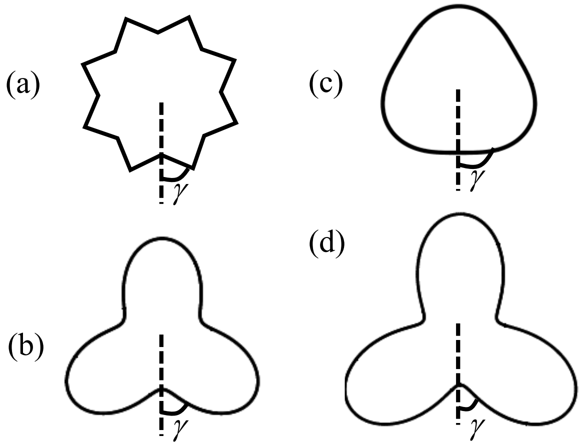

Fig. 7.6 semi-angle α is shown for (a): wedge-shaped cross-section and trilobal fiber with (b) $a = 0.4$, (c) $a = 0.1$ and (d) $a = 0.5$.

7.3.4 Effect of Gravity on the Shape of Droplet

Asymmetric factor ε is defined as the criteria of transition between symmetric barrel shape and asymmetric one. Asymmetric factor can be calculated by the ratio of the upper part of the droplet h_1 to the lower part h_2 (see inset of Fig. 7.7) ranging from 1 (completely barrel shape) to 0 (completely asymmetric). Here we arbitrarily categorized a droplet as a barrel shape droplet when $\varepsilon \geq 0.85$ and as an asymmetric droplet when $\varepsilon < 0.85$. The change in ε under the gravity effect for different volume of a droplet on a trilobal fiber with different lobe height and φ is shown in Fig. 7.7. It can be seen that as volume of the droplet increases ε decreases, however increasing lobe height delays that. This figure also shows that the effect of φ orientation is negligible on ε except for very small volumes. At smaller volume for $\varphi = -90^{\circ}$ the effect of lobe height in ε is smaller comparing to $\varphi = 90^{\circ}$.

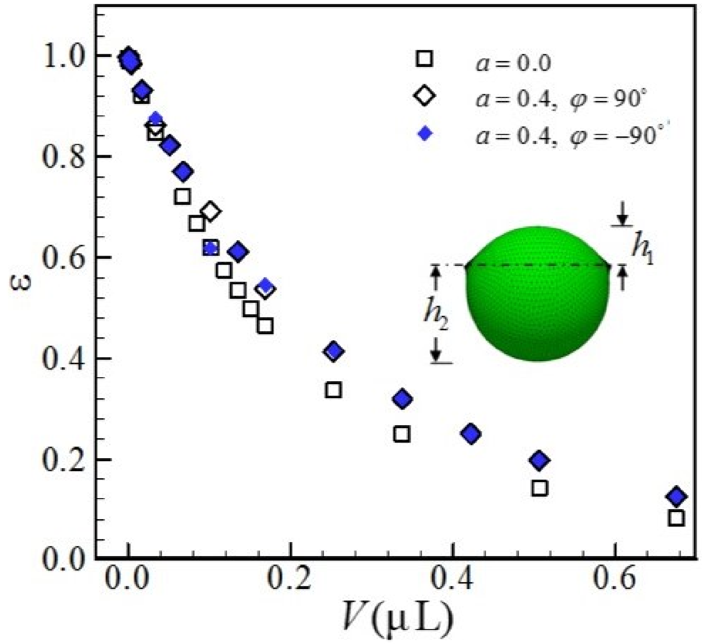

Fig 7.7 The asymmetry factor is obtained for droplets deposited on a trilobal fiber with a radius of $r = 15$ μm, and YLCAs of $\theta_{YL} = 30^{\circ}$ for two different lobe heights of a =0 (squares), and 0.4 (diamonds) for $\varphi = 90^{\circ}$ (black) and $\varphi = -90^{\circ}$ (blue).

7.4 Conclusions

A Droplet apparent contact angle on a trilobal fiber was studied for the first time and found to be a function of droplet volume, lobe height and lobe direction. We showed that when volume of the droplet is small ACA decreases as lobe amplitude increases but when the droplet volume is large the lobe amplitude does not significantly affect ACA. In addition, the lobe direction has a great effect on ACA especially for clamshell droplets. We also showed that lobe direction can effect the position of the clamshell droplet and that is why it affects ACA of clamshell droplet significantly. The detachment force from a trilobal fiber is also calculated and it was shown that the lobe amplitude and lobe direction has significant role in detachment force when droplet volume is small. However, the effect of lobe direction and lobe amplitude becomes negligible on detachment force when droplet volume is high.

Chapter 8. Overall Conclusion

The main goal of this thesis is to predict the interaction between liquid and curved surfaces. We first presented analytical and numerical methods to estimate the air-water interface stability over fibrous and also granular superhydrophobic coatings under elevated pressures and the efficiency of such surfaces in drag reduction for underwater applications. Then the wetting behavior of a droplet deposited on a fibrous media and the force required to detach the droplet from such media are investigated. A novel technique based on using ferrofluid in a magnetic field is also designed to measure force required to detach a droplet from fiber(s).

The proposed numerical and analytical models give us the ability to predict the performance of surfaces comprised of fibers/particles with dissimilar size and wettabilities. We also developed a mono-dispersed equivalent diameter definition that can be used to predict the critical pressure and wetted area of coatings with dissimilar particle size and wettability distributions. The formulation developed here can be applied to coatings with random or ordered spatial particle distributions. Our results showed that critical pressure –air-water interface stability– improves with increasing solid volume fraction, but there is a limitation on this due to increase in wetted area for higher solid volume fractions, which causes significant slip length reduction.

The wetting behavior of a droplet deposited on a rough fiber or a trilobal fiber is also investigated numerically. Our results indicate that increasing fiber roughness or lobe height increases the wettability of droplet so the occurrence of different droplet shape configurations on a fiber (symmetric barrel, clamshell, and asymmetric barrel) depends on fiber roughness or lobe height, droplet volume, and fiber radius. In particular, it was shown that when roughness or lobe height increases so as the tendency of a droplet to remain in the symmetric barrel shape configuration at higher droplet volume. We also found that the effect of fiber roughness or lobe height becomes less significant on large droplet volume relative to roughness amplitude or frequency.

A novel technique is also developed to measure the force required to detach a droplet from a fiber or from a fiber assembly. The method relies on the use of ferrofluid droplets in a magnetic field in a setup placed on a sensitive scale. The proposed method eliminates the need for using air or an external object to move or detach the droplet from the fiber(s), and therefore it allows one to study the capillarity of the droplet–fiber system in a more isolated environment. The results of our study indicate that the force per unit mass required to detach a droplet from a single fiber is higher when the droplet is small, and it decreases by decreasing the volume of the droplet. Studying intersecting fibers with different relative angle with respect to one another, it was found that the relative angle between the fibers has negligible effect on the force required to detach the droplet in the out-of-plane direction. This angle however, can greatly influence the detachment force in the in-plane direction; increasing the relative angle between the fibers increases the droplet detachment force in the in-plane direction especially for smaller droplets. It was also found that it is harder to detach a droplet from intersecting fibers when the force is applied in the direction of the bisector of the angle between the fibers. Our experimental study was accompanied by numerical simulations. Good general agreement has been observed between the experimental and computational results.

Chapter 9. References

1. Srinivasan S, Choi W, Park K-C, Chhatre SS, Cohen RE, McKinley GH. Drag reduction for viscous laminar flow on spray-coated non-wetting surfaces. Soft Matter. 2013;9(24):5691–702.

2. Butt H-J, Semprebon C, Papadopoulos P, Vollmer D, Brinkmann M, Ciccotti M. Design principles for superamphiphobic surfaces. Soft Matter. 2013;9(2):418–28.

3. de Gennes P-G, Brochard-Wyart F, Quéré D. Capillarity and Wetting Phenomena. Springer New York; 2004.

4. Allen RF, Benson PR. Rolling drops on an inclined plane. J Colloid Interface Sci. 1975 Feb 1;50(2):250–3.

5. Richard D, Quéré D. Viscous drops rolling on a tilted non-wettable solid. EPL Europhys Lett. 1999;48(3):286.

6. Mahadevan L, Pomeau Y. Rolling droplets. Phys Fluids. 1999;11(9):2449–53.

7. DING H, GILANI MNH, SPELT PDM. Sliding, pinch-off and detachment of a droplet on a wall in shear flow. J Fluid Mech. 2AD 2010;644:217–44.

8. Semprebon C, Brinkmann M. On the onset of motion of sliding drops. Soft Matter. 2014;10(18):3325–34.

9. Young T. An Essay on the Cohesion of Fluids. Philos Trans R Soc Lond. 1805;95:65–87.

10. Ou J, Rothstein JP. Direct velocity measurements of the flow past drag-reducing ultrahydrophobic surfaces. Phys Fluids. 2005;17(10).

11. Tuteja A, Choi W, Mabry JM, McKinley GH, Cohen RE. Robust omniphobic surfaces. Proc Natl Acad Sci. 2008 Nov 25;105(47):18200–5.

12. McHale G, Shirtcliffe NJ, Evans CR, Newton MI. Terminal velocity and drag reduction measurements on superhydrophobic spheres. Appl Phys Lett. 2009;94(6).

13. Extrand CW. Repellency of the Lotus Leaf: Resistance to Water Intrusion under Hydrostatic Pressure. Langmuir. 2011 Jun 7;27(11):6920–5.

14. Samaha MA, Vahedi Tafreshi H, Gad-el-Hak M. Modeling drag reduction and meniscus stability of superhydrophobic surfaces comprised of random roughness. Phys Fluids. 2011;23(1).

15. Dong H, Cheng M, Zhang Y, Wei H, Shi F. Extraordinary drag-reducing effect of a superhydrophobic coating on a macroscopic model ship at high speed. J Mater Chem A. 2013;1(19):5886–91.

16. Extrand CW. Criteria for Ultralyophobic Surfaces. Langmuir. 2004 Jun 1;20(12):5013–8.

17. Samaha MA, Tafreshi HV, Gad-el-Hak M. Influence of Flow on Longevity of Superhydrophobic Coatings. Langmuir. 2012 Jun 26;28(25):9759–66.

18. Hemeda AA, Gad-el-Hak M, Tafreshi HV. Effects of hierarchical features on longevity of submerged superhydrophobic surfaces with parallel grooves. Phys Fluids [Internet]. 2014;26(8). Available from: http://scitation.aip.org/content/aip/journal/pof2/26/8/10.1063/1.4891363

19. Hemeda AA, Tafreshi HV. General Formulations for Predicting Longevity of Submerged Superhydrophobic Surfaces Composed of Pores or Posts. Langmuir. 2014 Sep 2;30(34):10317–27.

20. Esmeryan KD, Castano CE, Bressler AH, Abolghasemibizaki M, Mohammadi R. Rapid synthesis of inherently robust and stable superhydrophobic carbon soot coatings. Appl Surf Sci. 2016 Apr 30;369:341–7.

21. Shirtcliffe NJ, McHale G, Newton MI, Chabrol G, Perry CC. Dual-Scale Roughness Produces Unusually Water-Repellent Surfaces. Adv Mater. 2004 Nov 4;16(21):1929–32.

22. Lee C, Choi C-H, Kim C-J "CJ." Structured Surfaces for a Giant Liquid Slip. Phys Rev Lett. 2008 Aug 5;101(6):64501.

23. Ma M, Hill RM, Rutledge GC. A Review of Recent Results on Superhydrophobic Materials Based on Micro- and Nanofibers. J Adhes Sci Technol. 2008 Jan 1;22(15):1799–817.

24. Emami B, Bucher TM, Tafreshi HV, Pestov D, Gad-el-Hak M, Tepper GC. Simulation of meniscus stability in superhydrophobic granular surfaces under hydrostatic pressures. Colloids Surf Physicochem Eng Asp. 2011 Jul 20;385(1–3):95–103.

25. Samaha MA, Ochanda FO, Tafreshi HV, Tepper GC, Gad-el-Hak M. In situ, noninvasive characterization of superhydrophobic coatings. Rev Sci Instrum. 2011;82(4).

26. Samaha MA, Vahedi Tafreshi H, Gad-el-Hak M. Effects of hydrostatic pressure on the drag reduction of submerged aerogel-particle coatings. Colloids Surf Physicochem Eng Asp. 2012 Apr 5;399:62–70.

27. Emami B, Tafreshi HV, Gad-el-Hak M, Tepper GC. Effect of fiber orientation on shape and stability of air–water interface on submerged superhydrophobic electrospun thin coatings. J Appl Phys. 2012;111(6).

28. Hemeda AA, Vahedi Tafreshi H. Instantaneous slip length in superhydrophobic microchannels having grooves with curved or dissimilar walls. Phys Fluids [Internet]. 2015;27(10). Available from: http://scitation.aip.org/content/aip/journal/pof2/27/10/10.1063/1.4931588

29. Hemeda AA, Tafreshi HV. Liquid–Infused Surfaces with Trapped Air (LISTA) for Drag Force Reduction. Langmuir. 2016 Mar 29;32(12):2955–62.

30. Venkateshan DG, Amrei M., Hemeda AA, Cullingsworth Z, Corbett J, Vahedi Tafreshi H. Failure pressures and drag reduction benefits of superhydrophobic wire screens. Colloids Surf Physicochem Eng Asp. 2016 Dec 20;511:247–54.

31. Hemeda AA, Tafreshi HV. Pressure-Enhanced Slip Length using LISTA Surfaces. J Appl Phys. 2016;

32. Wenzel RN. RESISTANCE OF SOLID SURFACES TO WETTING BY WATER. Ind Eng Chem. 1936 Aug 1;28(8):988–94.

33. Cassie ABD, Baxter S. Wettability of porous surfaces. Trans Faraday Soc. 1944;40(0):546–51.

34. Emami B, Hemeda AA, Amrei MM, Luzar A, Gad-el-Hak M, Vahedi Tafreshi H. Predicting longevity of submerged superhydrophobic surfaces with parallel grooves. Phys Fluids. 2013;25(6).

35. Amrei MM, Tafreshi HV. Effects of hydrostatic pressure on wetted area of submerged superhydrophobic granular coatings. Part 1: mono-dispersed coatings. Colloids Surf Physicochem Eng Asp. 2015 Jan 20;465:87–98.

36. Amrei MM, Tafreshi HV. Effects of pressure on wetted area of submerged superhydrophobic granular coatings. Part II: poly-dispersed coatings. Colloids Surf Physicochem Eng Asp. 2015 Sep 20;481:547–60.

37. Poetes R, Holtzmann K, Franze K, Steiner U. Metastable Underwater Superhydrophobicity. Phys Rev Lett. 2010 Oct;105(16):166104.

38. Brakke KA. Surface evolver Manual. 2.24. Mathematics Department, Susquehanna Univerisity, Selinsgrove, PA; 1994.

39. Brakke KA. The Surface Evolver. Exp Math. 1992 Jan 1;1(2):141–65.

40. Kaul S, Saxena RC, Kumar A, Negi MS, Bhatnagar AK, Goyal HB, et al. Corrosion behavior of biodiesel from seed oils of Indian origin on diesel engine parts. Fuel Process Technol. 2007 Mar;88(3):303–7.

41. Charvet A, Gonthier Y, Bernis A, Gonze E. Filtration of liquid aerosols with a horizontal fibrous filter. 11th Congr Fr Chem Eng Soc. 2008 Jun;86(6):569–76.

42. Šikalo Š, Wilhelm H-D, Roisman IV, Jakirlić S, Tropea C. Dynamic contact angle of spreading droplets: Experiments and simulations. Phys Fluids [Internet]. 2005;17(6). Available from: http://scitation.aip.org/content/aip/journal/pof2/17/6/10.1063/1.1928828

43. Yarin AL. DROP IMPACT DYNAMICS: Splashing, Spreading, Receding, Bouncing…. Annu Rev Fluid Mech. 2005 Dec 16;38(1):159–92.

44. Jung YC, Bhushan B. Wetting Behavior of Water and Oil Droplets in Three-Phase Interfaces for Hydrophobicity/philicity and Oleophobicity/philicity. Langmuir. 2009 Dec 15;25(24):14165–73.

45. Aziz H, Amrei MM, Dotivala A, Tang C, Tafreshi HV. Modeling Cassie droplets on superhydrophobic coatings with orthogonal fibrous structures. Colloids Surf Physicochem Eng Asp. 2017 Jan 1;512:61–70.

46. Carroll BJ. Equilibrium conformations of liquid drops on thin cylinders under forces of capillarity. A theory for the roll-up process. Langmuir. 1986 Mar 1;2(2):248–50.

47. McHale G, Newton M. Global geometry and the equilibrium shapes of liquid drops on fibers. Colloids Surf Physicochem Eng Asp. 2002 Jul 9;206(1–3):79–86.

48. Rebouillat S, Letellier B, Steffenino B. Wettability of single fibres – beyond the contact angle approach. Int J Adhes Adhes. 1999 Aug 1;19(4):303–14.

49. Chou T-H, Hong S-J, Liang Y-E, Tsao H-K, Sheng Y-J. Equilibrium Phase Diagram of Drop-on-Fiber: Coexistent States and Gravity Effect. Langmuir. 2011 Apr 5;27(7):3685–92.

50. Kumar A, Hartland S. Measurement of contact angles from the shape of a drop on a vertical fiber. J Colloid Interface Sci. 1990 May 1;136(2):455–69.

51. Mei M, Fan J, Shou D. The gravitational effect on the geometric profiles of droplets on horizontal fibers. Soft Matter. 2013;9(43):10324–34.

52. Yarin AL, Liu W, Reneker DH. Motion of droplets along thin fibers with temperature gradient. J Appl Phys. 2002;91(7):4751–60.

53. Dawar S, Chase GG. Drag correlation for axial motion of drops on fibers. Sep Purif Technol. 2008 Apr 1;60(1):6–13.

54. Sahu RP, Sinha-Ray S, Yarin AL, Pourdeyhimi B. Blowing drops off a filament. Soft Matter. 2013;9(26):6053–71.

55. Mead-Hunter R, Mullins BJ, Becker T, Braddock RD. Evaluation of the Force Required to Move a Coalesced Liquid Droplet along a Fiber. Langmuir. 2011 Jan 4;27(1):227–32.

56. Dawar S, Chase GG. Correlations for transverse motion of liquid drops on fibers. Sep Purif Technol. 2010 May 11;72(3):282–7.

57. Mullins BJ, Braddock RD, Agranovski IE. Modelling droplet motion and interfacial tension in filters collecting liquid aerosols. Sel Pap Comb IMACS World Congr MSSANZ 18th Bienn Conf Model Simul Cairns Aust 13-17 July 2009. 2011 Mar;81(7):1257–71.

58. Funk CS, Winzer B, Peukert W. Correlation between shape, evaporation mode and mobility of small water droplets on nanorough fibres. J Colloid Interface Sci. 2014 Mar 1;417:171–9.

59. Quéré D. Wetting and Roughness. Annu Rev Mater Res. 2008 Jul 8;38(1):71–99.

60. Rothstein JP. Slip on Superhydrophobic Surfaces. Annu Rev Fluid Mech. 2009 Dec 21;42(1):89–109.

61. Shirtcliffe NJ, McHale G, Atherton S, Newton MI. An introduction to superhydrophobicity. Phys-Chem Flow Behav Droplet Based Syst. 2010 Dec 15;161(1–2):124–38.

62. Samaha MA, Tafreshi HV, Gad-el-Hak M. Superhydrophobic surfaces: From the lotus leaf to the submarine. Biomim Flow Control. 2012 Jan 1;340(1):18–34.

63. Papadopoulos P, Mammen L, Deng X, Vollmer D, Butt H-J. How superhydrophobicity breaks down. Proc Natl Acad Sci. 2013 Feb 26;110(9):3254–8.

64. Forsberg P, Nikolajeff F, Karlsson M. Cassie-Wenzel and Wenzel-Cassie transitions on immersed superhydrophobic surfaces under hydrostatic pressure. Soft Matter. 2011;7(1):104–9.

65. Rathgen H, Mugele F. Microscopic shape and contact angle measurement at a superhydrophobic surface. Faraday Discuss. 2010;146(0):49–56.

66. Bobji MS, Kumar SV, Asthana A, Govardhan RN. Underwater Sustainability of the "Cassie" State of Wetting. Langmuir. 2009 Oct 20;25(20):12120–6.

67. Lei L, Li H, Shi J, Chen Y. Diffraction Patterns of a Water-Submerged Superhydrophobic Grating under Pressure. Langmuir. 2010 Mar 2;26(5):3666–9.

68. Park H, Sun G, Kim C-J "CJ." Superhydrophobic turbulent drag reduction as a function of surface grating parameters. J Fluid Mech. 2014 005;747:722–34.

69. Steinberger A, Cottin-Bizonne C, Kleimann P, Charlaix E. High friction on a bubble mattress. Nat Mater. 2007 Sep;6(9):665–8.

70. Karatay E, Haase AS, Visser CW, Sun C, Lohse D, Tsai PA, et al. Control of slippage with tunable bubble mattresses. Proc Natl Acad Sci. 2013 May 21;110(21):8422–6.

71. Crowdy D. Slip length for longitudinal shear flow over a dilute periodic mattress of protruding bubbles. Phys Fluids. 2010;22(12).

72. Liu B, Lange FF. Pressure induced transition between superhydrophobic states: Configuration diagrams and effect of surface feature size. J Colloid Interface Sci. 2006 Jun 15;298(2):899–909.

73. Emami B, Tafreshi HV, Gad-el-Hak M, Tepper GC. Predicting shape and stability of air–water interface on superhydrophobic surfaces with randomly distributed, dissimilar posts. Appl Phys Lett. 2011;98(20).

74. Emami B, Vahedi Tafreshi H, Gad-el-Hak M, Tepper GC. Predicting shape and stability of air–water interface on superhydrophobic surfaces comprised of pores with arbitrary shapes and depths. Appl Phys Lett. 2012;100(1).

75. Nosonovsky M. Multiscale Roughness and Stability of Superhydrophobic Biomimetic Interfaces. Langmuir. 2007 Mar 1;23(6):3157–61.

76. Extrand CW, Moon SI. Intrusion Pressure To Initiate Flow through Pores between Spheres. Langmuir. 2012 Feb 21;28(7):3503–9.

77. Badge I, Bhawalkar SP, Jia L, Dhinojwala A. Tuning surface wettability using single layered and hierarchically ordered arrays of spherical colloidal particles. Soft Matter. 2013;9(11):3032–40.

78. Morris GDM, Neethling SJ, Cilliers JJ. A Model for the Stability of Films Stabilized by Randomly Packed Spherical Particles. Langmuir. 2011 Sep 20;27(18):11475–80.

79. Morris GDM, Neethling SJ, Cilliers JJ. The stability of a thin liquid film supported by a double layer of spherical particles. Colloids Surf Physicochem Eng Asp. 2014 Feb 20;443:44–51.

80. Davis AMJ, Lauga E. The friction of a mesh-like super-hydrophobic surface. Phys Fluids. 2009;21(11).

81. LAUGA E, STONE HA. Effective slip in pressure-driven Stokes flow. J Fluid Mech. 2003 Jul 1;489:55–77.

82. Ng C-O, Wang CY. Apparent slip arising from Stokes shear flow over a bidimensional patterned surface. Microfluid Nanofluidics. 2010;8(3):361–71.

83. Zhou J, Asmolov ES, Schmid F, Vinogradova OI. Effective slippage on superhydrophobic trapezoidal grooves. J Chem Phys. 2013;139(17).

84. Wang LP, Teo CJ, Khoo BC. Effects of interface deformation on flow through microtubes containing superhydrophobic surfaces with longitudinal ribs and grooves. Microfluid Nanofluidics. 2014;16(1):225–36.

85. Vinogradova OI. Slippage of water over hydrophobic surfaces. Int J Miner Process. 1999 Apr;56(1–4):31–60.

86. Slobozhanin LA, Alexander JID, Collicott SH, Gonzalez SR. Capillary pressure of a liquid in a layer of close-packed uniform spheres. Phys Fluids. 2006;18(8).

87. Cho Y-S, Choi S-Y, Kim Y-K, Yi G-R. Bulk synthesis of ordered macroporous silica particles for superhydrophobic coatings. J Colloid Interface Sci. 2012 Nov 15;386(1):88–98.

88. Tenjimbayashi M, Shiratori S. Highly durable superhydrophobic coatings with gradient density by movable spray method. J Appl Phys. 2014;116(11).

89. Weng R, Zhang H, Liu X. Spray-coating process in preparing PTFE-PPS composite super-hydrophobic coating. AIP Adv. 2014;4(3).

90. Bhushan B, Jung YC, Koch K. Self-Cleaning Efficiency of Artificial Superhydrophobic Surfaces. Langmuir. 2009 Mar 3;25(5):3240–8.

91. Kwon DH, Huh HK, Lee SJ. Wetting state and maximum spreading factor of microdroplets impacting on superhydrophobic textured surfaces with anisotropic arrays of pillars. Exp Fluids. 2013;54(7):1576.

92. Hensel R, Finn A, Helbig R, Killge S, Braun H-G, Werner C. In Situ Experiments To Reveal the Role of Surface Feature Sidewalls in the Cassie–Wenzel Transition. Langmuir. 2014 Dec 23;30(50):15162–70.

93. Wu H, Zhang R, Sun Y, Lin D, Sun Z, Pan W, et al. Biomimetic nanofiber patterns with controlled wettability. Soft Matter. 2008;4(12):2429–33.

94. Shin B, Lee K-R, Moon M-W, Kim H-Y. Extreme water repellency of nanostructured low-surface-energy non-woven fabrics. Soft Matter. 2012;8(6):1817–23.

95. Nuraje N, Khan WS, Lei Y, Ceylan M, Asmatulu R. Superhydrophobic electrospun nanofibers. J Mater Chem A. 2013;1(6):1929–46.

96. Hsieh C-T, Wu F-L, Yang S-Y. Superhydrophobicity from composite nano/microstructures: Carbon fabrics coated with silica nanoparticles. Surf Coat Technol. 2008 Aug 15;202(24):6103–8.

97. Xu B, Cai Z, Wang W, Ge F. Preparation of superhydrophobic cotton fabrics based on SiO2 nanoparticles and ZnO nanorod arrays with subsequent hydrophobic modification. Surf Coat Technol. 2010 Jan 25;204(9–10):1556–61.

98. Zhao Y, Tang Y, Wang X, Lin T. Superhydrophobic cotton fabric fabricated by electrostatic assembly of silica nanoparticles and its remarkable buoyancy. Appl Surf Sci. 2010 Sep 1;256(22):6736–42.

99. Katta P, Alessandro M, Ramsier RD, Chase GG. Continuous Electrospinning of Aligned Polymer Nanofibers onto a Wire Drum Collector. Nano Lett. 2004 Nov 1;4(11):2215–8.

100. Sarkar S, Deevi S, Tepper G. Biased AC Electrospinning of Aligned Polymer Nanofibers. Macromol Rapid Commun. 2007;28(9):1034–1039.

101. Ochanda FO, Samaha MA, Tafreshi HV, Tepper GC, Gad-el-Hak M. Fabrication of superhydrophobic fiber coatings by DC-biased AC-electrospinning. J Appl Polym Sci. 2012;123(2):1112–1119.

102. Dalton PD, Vaquette C, Farrugia BL, Dargaville TR, Brown TD, Hutmacher DW. Electrospinning and additive manufacturing: converging technologies. Biomater Sci. 2013;1(2):171–85.

103. Ghochaghi N. Experimental Development of Advanced Air Filtration Media Based on Electrospun Polymer Fibers [Internet]. VCU; 2014. Available from: http://scholarscompass.vcu.edu/etd/3631/

104. Ghochaghi N, Taiwo A, Winkel M, Dodd B, Mossi K, Tepper G. Electrospun polystyrene coatings with tunable wettability. J Appl Polym Sci. 2015;132(10):n/a–n/a.

105. Patel SU, Chase GG. Separation of water droplets from water-in-diesel dispersion using superhydrophobic polypropylene fibrous membranes. Sep Purif Technol. 2014 Apr 15;126:62–8.

106. Patel SU, Patel SU, Chase GG. Electrospun Superhydrophobic Poly(vinylidene fluoride-co-hexafluoropropylene) Fibrous Membranes for the Separation of Dispersed Water from Ultralow Sulfur Diesel. Energy Fuels. 2013 May 16;27(5):2458–64.

107. Wang F, Yu S, Xue M, Ou J, Li W. A superhydrophobic and superoleophilic miniature mesh box for oil spill clean up. New J Chem. 2014;38(9):4388–93.

108. Tian D, Zhang X, Tian Y, Wu Y, Wang X, Zhai J, et al. Photo-induced water-oil separation based on switchable superhydrophobicity-superhydrophilicity and underwater superoleophobicity of the aligned ZnO nanorod array-coated mesh films. J Mater Chem. 2012;22(37):19652–7.

109. Song J, Huang S, Lu Y, Bu X, Mates JE, Ghosh A, et al. Self-Driven One-Step Oil Removal from Oil Spill on Water via Selective-Wettability Steel Mesh. ACS Appl Mater Interfaces. 2014 Nov 26;6(22):19858–65.

110. Litster S, Sinton D, Djilali N. Ex situ visualization of liquid water transport in PEM fuel cell gas diffusion layers. J Power Sources. 2006 Mar 9;154(1):95–105.

111. Zhou P, Wu CW. Liquid water transport mechanism in the gas diffusion layer. J Power Sources. 2010 Mar 1;195(5):1408–15.

112. Hao L, Cheng P. Lattice Boltzmann simulations of water transport in gas diffusion layer of a polymer electrolyte membrane fuel cell. J Power Sources. 2010 Jun 15;195(12):3870–81.

113. Caulk DA, Baker DR. Modeling Two-Phase Water Transport in Hydrophobic Diffusion Media for PEM Fuel Cells. J Electrochem Soc. 2011 Apr 1;158(4):B384–93.

114. Young-Min Shin and Seung-Ki Lee and Joo-Yong Lee and Jun-Ho Kim and Jae-Hyoung Park and Chang-Hyeon Ji. Microfabricated environmental barrier using ZnO nanowire on metal mesh. J Micromechanics Microengineering. 2013;23(12):127001.

115. Yohe ST, Freedman JD, Falde EJ, Colson YL, Grinstaff MW. A Mechanistic Study of Wetting Superhydrophobic Porous 3D Meshes. Adv Funct Mater. 2013;23(29):3628–3637.

116. Bucher TM, Emami B, Tafreshi HV, Gad-el-Hak M, Tepper GC. Modeling resistance of nanofibrous superhydrophobic coatings to hydrostatic pressures: The role of microstructure. Phys Fluids. 2012;24(2).

117. Bucher TM, Amrei MM, Vahedi Tafreshi H. Wetting resistance of heterogeneous superhydrophobic coatings with orthogonally layered fibers. Surf Coat Technol. 2015 Sep 15;277:117–27.

118. Bucher TM, Vahedi Tafreshi H. Modeling air–water interface in disordered fibrous media with heterogeneous wettabilities. Colloids Surf Physicochem Eng Asp. 2014 Nov 5;461:323–35.

119. Carroll BJ. The equilibrium of liquid drops on smooth and rough circular cylinders. J Colloid Interface Sci. 1984 Jan 1;97(1):195–200.

120. Lyklema, J., Mchale, G., Newton, M. I., Carroll, B. J. Forme et stabilité de gouttelettes de liquide sur des fibres. Oil Gas Sci Technol - Rev IFP. 2001;56(1):47–54.

121. Lorenceau É, Clanet C, Quéré D. Capturing drops with a thin fiber. J Colloid Interface Sci. 2004 Nov 1;279(1):192–7.

122. Eral HB, de Ruiter J, de Ruiter R, Oh JM, Semprebon C, Brinkmann M, et al. Drops on functional fibers: from barrels to clamshells and back. Soft Matter. 2011;7(11):5138–43.

123. de Ruiter R, de Ruiter J, Eral HB, Semprebon C, Brinkmann M, Mugele F. Buoyant Droplets on Functional Fibers. Langmuir. 2012 Sep 18;28(37):13300–6.

124. Wolansky G, Marmur A. Apparent contact angles on rough surfaces: the Wenzel equation revisited. Colloids Surf Physicochem Eng Asp. 1999 Oct 15;156(1–3):381–8.

125. McHale G. Cassie and Wenzel: Were They Really So Wrong? Langmuir. 2007 Jul 1;23(15):8200–5.

126. Marmur A, Bittoun E. When Wenzel and Cassie Are Right: Reconciling Local and Global Considerations. Langmuir. 2009 Feb 3;25(3):1277–81.

127. Montes Ruiz-Cabello FJ, Rodríguez-Valverde MA, Marmur A, Cabrerizo-Vílchez MA. Comparison of Sessile Drop and Captive Bubble Methods on Rough Homogeneous Surfaces: A Numerical Study. Langmuir. 2011 Aug 2;27(15):9638–43.

128. Cox RG. The spreading of a liquid on a rough solid surface. J Fluid Mech. 1983 Jun 1;131:1–26.

129. David R, Neumann AW. Contact Angle Hysteresis on Randomly Rough Surfaces: A Computational Study. Langmuir. 2013 Apr 9;29(14):4551–8.

130. Zheng Y, Bai H, Huang Z, Tian X, Nie F-Q, Zhao Y, et al. Directional water collection on wetted spider silk. Nature. 2010 Feb 4;463(7281):640–3.

131. Gac JM, Gradoń L. Modeling of axial motion of small droplets deposited on smooth and rough fiber surfaces. Colloids Surf Physicochem Eng Asp. 2012 Nov 20;414:259–66.

132. Chen Y, Zheng Y. Bioinspired micro-/nanostructure fibers with a water collecting property. Nanoscale. 2014;6(14):7703–14.

133. Davoudi M, Fang J, Chase GG. Barrel shaped droplet movement at junctions of perpendicular fibers with different orientations to the air flow direction. Sep Purif Technol. 2016 Apr 13;162:1–5.

134. Fang J, Davoudi M, Chase GG. Drop movement along a fiber axis due to pressure driven air flow in a thin slit. Sep Purif Technol. 2015 Jan 22;140:77–83.

135. Chini SF, Amirfazli A. A method for measuring contact angle of asymmetric and symmetric drops. Colloids Surf Physicochem Eng Asp. 2011 Sep 5;388(1–3):29–37.

136. Dufour R, Dibao-Dina A, Harnois M, Tao X, Dufour C, Boukherroub R, et al. Electrowetting on functional fibers. Soft Matter. 2013;9(2):492–7.

137. Contal P, Simao J, Thomas D, Frising T, Callé S, Appert-Collin J., et al. Clogging of fibre filters by submicron droplets. Phenomena and influence of operating conditions. J Aerosol Sci. 2004 Mar;35(2):263–78.

138. Michielsen S, Lee HJ. Design of a Superhydrophobic Surface Using Woven Structures. Langmuir. 2007 May 1;23(11):6004–10.

139. Wurster S, Meyer J, Kolb HE, Kasper G. Bubbling vs. blow-off – On the relevant mechanism(s) of drop entrainment from oil mist filter media. Sep Purif Technol. 2015 Sep 25;152:70–9.

140. Gauthier E, Hellstern T, Kevrekidis IG, Benziger J. Drop Detachment and Motion on Fuel Cell Electrode Materials. ACS Appl Mater Interfaces. 2012 Feb 22;4(2):761–71.

141. Gilet T, Terwagne D, Vandewalle N. Digital microfluidics on a wire. Appl Phys Lett. 2009;95(1).

142. Ju J, Bai H, Zheng Y, Zhao T, Fang R, Jiang L. A multi-structural and multi-functional integrated fog collection system in cactus. Nat Commun. 2012 Dec 4;3:1247.

143. Bai H, Tian X, Zheng Y, Ju J, Zhao Y, Jiang L. Direction Controlled Driving of Tiny Water Drops on Bioinspired Artificial Spider Silks. Adv Mater. 2010;22(48):5521–5525.

144. Carroll B. The accurate measurement of contact angle, phase contact areas, drop volume, and Laplace excess pressure in drop-on-fiber systems. J Colloid Interface Sci. 1976 Dec 1;57(3):488–95.

145. Gilet T, Terwagne D, Vandewalle N. Droplets sliding on fibres. Eur Phys J E. 2010;31(3):253–62.

146. Bick A, Boulogne F, Sauret A, Stone HA. Tunable transport of drops on a vibrating inclined fiber. Appl Phys Lett. 2015;107(18).

147. Haefner S, Baumchen O, Jacobs K. Capillary droplet propulsion on a fibre. Soft Matter. 2015;11(35):6921–6.

148. Mullins BJ, Pfrang A, Braddock RD, Schimmel T, Kasper G. Detachment of liquid droplets from fibres—Experimental and theoretical evaluation of detachment force due to interfacial tension effects. J Colloid Interface Sci. 2007 Aug 15;312(2):333–40.

149. Dressaire E, Sauret A, Boulogne F, Stone HA. Drop impact on a flexible fiber. Soft Matter. 2016;12(1):200–8.

150. Sauret A, Bick AD, Duprat C, Stone HA. Wetting of crossed fibers: Multiple steady states and symmetry breaking. EPL Europhys Lett. 2014;105(5):56006.

151. Hotz CJ, Mead-Hunter R, Becker T, King AJC, Wurster S, Kasper G, et al. Detachment of droplets from cylinders in flow using an experimental analogue. J Fluid Mech. 2015 005;771:327–40.

152. Weyer F, Lismont M, Dreesen L, Vandewalle N. Compound droplet manipulations on fiber arrays. Soft Matter. 2015;11(36):7086–91.

153. Santos MJ, White JA. Theory and Simulation of Angular Hysteresis on Planar Surfaces. Langmuir. 2011 Dec 20;27(24):14868–75.

154. Promraksa A, Chen L-J. Modeling contact angle hysteresis of a liquid droplet sitting on a cosine wave-like pattern surface. J Colloid Interface Sci. 2012 Oct 15;384(1):172–81.

155. Nguyen N-T, Zhu G, Chua Y-C, Phan V-N, Tan S-H. Magnetowetting and Sliding Motion of a Sessile Ferrofluid Droplet in the Presence of a Permanent Magnet. Langmuir. 2010 Aug 3;26(15):12553–9.

156. Nguyen N-T. Deformation of Ferrofluid Marbles in the Presence of a Permanent Magnet. Langmuir. 2013 Nov 12;29(45):13982–9.

157. Manukyan S, Schneider M. Experimental Investigation of Wetting with Magnetic Fluids. Langmuir. 2016 May 24;32(20):5135–40.

158. Rigoni C, Pierno M, Mistura G, Talbot D, Massart R, Bacri J-C, et al. Static Magnetowetting of Ferrofluid Drops. Langmuir. 2016 Aug 2;32(30):7639–46.

159. Bormashenko EY. Wetting of Real Surfaces. De Gruyter; 2013. (De Gruyter Studies in Mathematical Physics).

160. Roe R-J. Wetting of fine wires and fibers by a liquid film. J Colloid Interface Sci. 1975 Jan 1;50(1):70–9.

161. Regan BD, Raynor PC. Single-Fiber Diffusion Efficiency for Elliptical Fibers. Aerosol Sci Technol. 2009 May 15;43(6):533–43.

162. Aneja AP, Renner M. Influence of the shape of fiber cross section on fabric surface characteristics. J Mater Sci. 2004 Jan 15;39(2):557–64.

163. Hutten IM. Handbook of Nonwoven Filter Media: Edition 2. 2007.

164. Fotovati S, Tafreshi HV, Pourdeyhimi B. Analytical expressions for predicting performance of aerosol filtration media made up of trilobal fibers. J Hazard Mater. 2011 Feb 28;186(2–3):1503–12.

165. Lamb GER, Costanza PA. Influences of Fiber Geometry on the Performance of Nonwoven Air Filters Part III : Cross-Sectional Shape. Text Res J. 1980;50:362–70.

166. Hosseini SA, Tafreshi HV. On the importance of fibers' cross-sectional shape for air filters operating in the slip flow regime. Powder Technol. 2011 Oct 25;212(3):425–31.

167. Dhaniyala S. An Asymmetrical, Three-Dimensional Model for Fibrous Filters. Aerosol Sci Technol. 1999 Apr 1;30(4):333–48.

168. Chikazumi S. Physics of Magnetism. John Wiley; 1964.

169. Osborn JA. Demagnetizing Factors of the General Ellipsoid. Phys Rev. 1945 Jun 1;67(11–12):351–7.

170. Bacri, J.C., Salin, D. Instability of ferrofluid magnetic drops under magnetic field. J Phys Lett. 1982;43(17):649–54.

Appendix A: Formulation for Magnetic Force Calculation

Magnetic force exerted on a droplet by a magnet F_m can be estimated from the distance between the droplet and the pole of the magnet, x. However, this method is only accurate for calculating the magnetic force exerted on a solid object whose shape and concentrations of magnetic material do not change during the experiment. The net body force acting on a droplet at the time of detachment (the body force required to overcome the capillary forces), can be expressed as,

$$F_D = F_m(x_D) - \rho V g \tag{A1}$$

where x_D is the distance between the droplet and magnet at the time of detachment. The magnetic force exerted on the droplet can be written as,

$$\overrightarrow{F_m} = V_p\left(\vec{M}.\nabla\vec{B} + \vec{B}.\nabla\vec{M}\right) \tag{A2}$$

in which V_p (cm^3) is the volume of the ferrofluid droplet, $\vec{M}$ (emu/cc) is the magnetic moment, and $\vec{B}$ (G) is magnetic flux density of the magnet. We used Lake Shore Model 475 Gaussmeter to measure the magnetic flux density as a function of distance from one of the poles of the magnet (see Fig. A1). The gradient of the magnetic field was then calculated from the data given in Fig. A1. Note that diameter of the magnet used in the experiment was much larger than the dimensions of the droplet, and so the magnetic field applied to the droplet was taken to be uniform in the lateral directions (normal to the direction of magnetic force).

Magnetic characterization of the ferrofluid was performed using the Quantum Design Versalab™ Vibrating Sample Magnetometer (VSM). A 0.1 mL droplet of the ferrofluid was deposited on to a substrate and placed in an oven to evaporate its water content. The dried Fe_3O_4/polymer mixture (mass of 9.3 mg) was then placed in a powder sample holder (P125E) and inserted into the VSM. To account for the variation in the ferromagnetic Fe_3O_4 nanoparticle volume fraction in the ferrofluid droplet [Manufacturer data sheet: Fe_3O_4 ~ 0.4 – 1.1% (by vol.), polymer ~ 0.5 – 1.5%], we plot a range for magnetization, *M*, for various volume fractions (See Fig. A2).

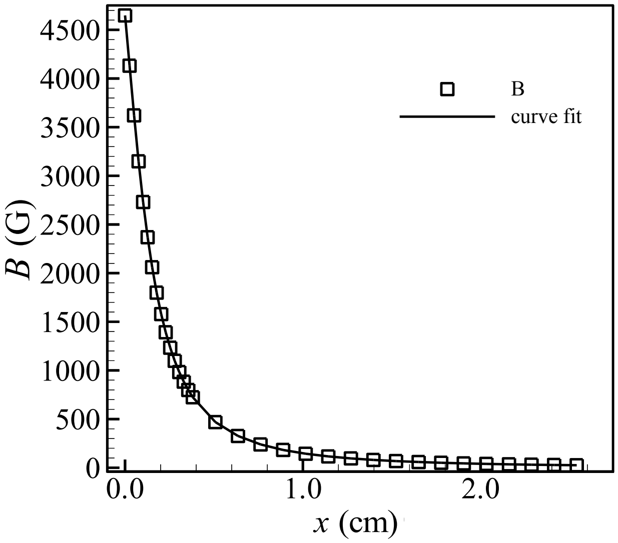

Figure A1: Magnetic flux density changes with distance to the magnet.

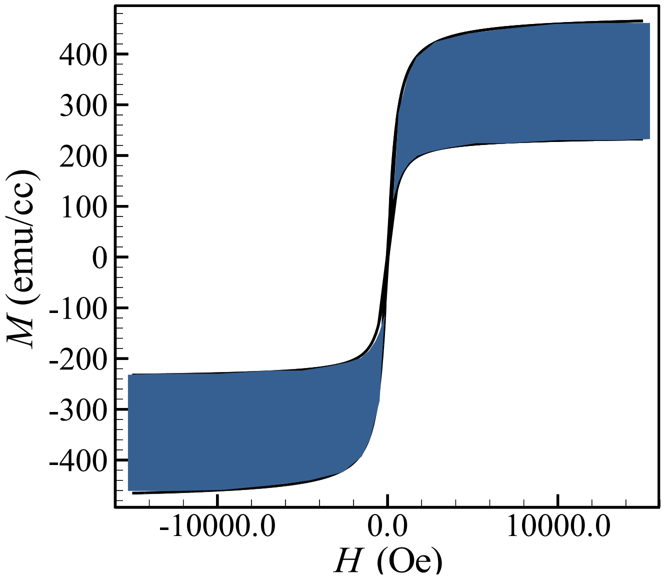

Figure A2: A range for M-H plot for the Fe3O4 powder.

Using $B = \mu H$ we can calculate H. Knowing $\vec{H}$ (applied magnetic field) one can calculate $\vec{M}$ from $\vec{M}$-$\vec{H}$ diagram. Consequently,

$$\overrightarrow{F_D} = V_p \left(\vec{M}.\nabla\vec{H} + \vec{H}.\nabla\vec{M}\right) - \rho V g \tag{A3}$$

It is worthy to mention that although a rangeis given for $\vec{M}$-$\vec{H}$ diagram due to the unavailability of volume fraction of magnetic particle, when calculating force this effect will be cancelled when multiplying by V_p. Note also that, we report force per unit mass, and so the force values were divided by ρV. Figure A3 compares the detachment forces obtained from our numerical simulations with those from Eq. A3 after demagnetization correction factor for *M-H* data and demagnetization correction factor for ferrofluid droplet shape are applied (see Appendix-A-1 and Appendix-A-2). Note that our numerical simulation results are in good quantitative agreement with our experimental (see Fig. 6.4b). As can be seen in Fig. A3, predictions of Eq. A3 are not in close agreement with the simulation results, although the show a correct trend for detachment force vs. droplet volume. As explained in chapter 6, to obtain accurate predictions from Eq. A3, one should incorporate the droplet shape change due to nanoparticle spatial distribution within the droplets. This however, is beyond the scope of chapter 6 as it involves solving a bi-directionally coupled magnetics, particle force and fluid problem. As explained in chapter 6, we decided to measure the detachment force directly by placing the test setup on a scale. After depositing the droplet on the setup we set the scale to zero to exclude the weight of the droplet. We then moved the magnet toward the droplet and read the scale until the droplet was detached. The reading that the scale showed right before the detachment was taken as the detachment force. Note that, we subtracted the gravity force as it acted in a direction opposite to the magnetic force.

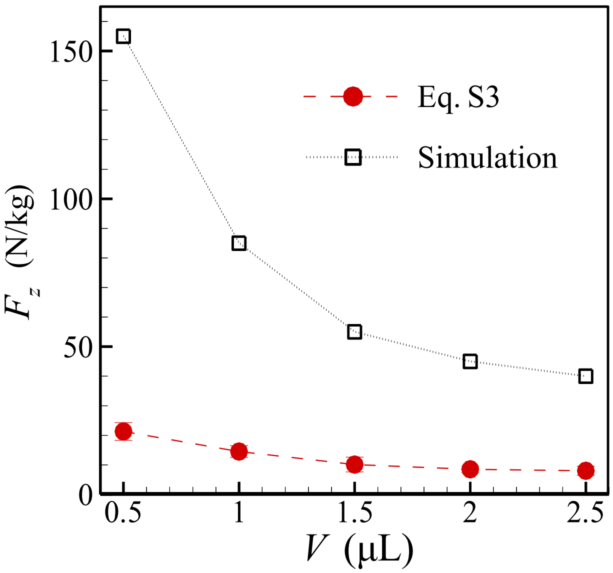

Figure A3: Force per unit mass required to detach ferrofluid droplets with different volumes from a fiber with a diameter of 215 μm. Comparison between predictions of Eq. A3 (red circles) and numerical simulation (black squares).

Appendix-A-1: Demagnetization correction factor for M-H data

When an external magnetic field is applied to a body, in addition to the induced magnetization, a demagnetizing field is generated within the material, which opposes the applied magnetic field, as given by the equation A4 (168)

$$H_d = N \cdot M \tag{A4}$$

where H_d is the demagnetizing field (Oe in CGS units), M is the induced magnetization (emu/cc in CGS units), and N is the demagnetization coefficient which is largely a shape-dependent factor. In the CGS units, the demagnetization factors along the three orthogonal axes is a constant, given by

$$N_a + N_b + N_c = 4\pi \tag{A5}$$

For the Fe_3O_4 powder, we approximate its volume to be that of the cylindrical powder holder (semi-major/minor axes, *a*, *b* = 0.145 cm, *c* = 0.075 cm, and *m* = *a/c*) as an oblate spheroid (major and minor axes, *a* = *b*) (169),

$$N_a = N_b = \frac{1}{2(m^2-1)}\left\{m^2(m^2-1)^{-\frac{1}{2}} \times sin^{-1}[\frac{(m^2-1)^{\frac{1}{2}}}{m}] - 1\right\} \tag{A6}$$

The demagnetization factor N was calculated along the in-plane axis of the applied magnetic field and found to be 0.2411. The demagnetizing field H_d, which opposes the applied magnetic field *H*, results in a lower effective magnetic field within the material/body,

$$H_{in} = H - N \cdot M \tag{A7}$$

Appendix-A-2: Demagnetization correction factor for ferrofluid droplet influenced by a magnet

As in section Appendix-1, one also needs to correct the demagnetization coefficient to account for the change in droplet shape when influenced by a magnet (i.e., droplet elongation toward the magnet before detachment).

The demagnetization coefficient, $N_{droplet}$, is given by (170)

$$N_{droplet} = K^2\left(-2\epsilon + ln\left((1+\epsilon)/(1-\epsilon)\right)\right)/2\epsilon^3 \tag{A8}$$

where *K* = *b/a* is the aspect ratio of the droplet (*a* and *b* are the semi-major and semi-minor axes of an ellipse, respectively), and $\epsilon = (1-K)^{\frac{1}{2}}$ is the ellipse eccentricity. We acknowledge that this is a simple approximation, as in reality the droplet shape may not be elliptical, and the Fe_3O_4 nanoparticle distribution within the droplet may be very non-uniform (not mapping the shape of the droplet). These factors can affect the demagnetization field significantly. Incorporating these effects and their ramification on the demagnetizing factor however is beyond the scope of chapter 6.

Appendix B: Vita

MANA MOKHTABAD AMREI

Cell: 804-549-7169; Email: mokhtabadamm@vcu.edu

SUMMARY

- Demonstrated problem-solving leadership in operational and analytical environments.
- Distinctive technical proficiency, with several publications in leading scientific journals.
- Highly capable and creative software programmer, with fluency across multiple languages.

PROFESSIONAL EXPERIENCE

Virginia Commonwealth University Richmond, VA

Graduate Research Assistant September, 2015 – December, 2016

Assisted in several research projects by developing numerical, experimental and analytical models to predict fluid/solid interaction. Collaborator for industrial and academic partners.

- Conducted pioneering research on droplet detachment mechanism from fibrous filtration media; designed innovative experimental methodologies using multiple analytical techniques and developed analytical formula that predicted experimental results with remarkable accuracy.
- Created analytical algorithms using multiple software packages and computer languages.
- Published or presented 11 papers during 3.5-year Ph.D. program.
- Mentored 3 PhD and 2 undergraduate students, including technical instruction, programming and preparation of scientific articles.
- Developed experiments and predictive models for numerous fluid/surface interactions including ferrofluid droplet motion in fibrous media, aerosols loaded fibers, entry pressure of various superhydrophobic surfaces and filters.

Graduate Teaching Assistant January, 2013 - August, 2015

Assistant for Numerical Methods, Thermodynamics, Topics in Nuclear Engineering, and Advanced Mathematics.

- Recognized as Outstanding Teaching Assistant for leadership and passion within VCU engineering program.

IranAir Tehran, Iran

Quality Assurance Engineer / Deputy to Quality Manager April, 2008 - December, 2012 *Original member of first company-wide quality department, created to address critical gaps in company's adherence to international air travel standards.*

- Established quality department's credibility in solving key operational and safety issues, resulting in successful adherence to international flight safety requirements. Overcame change resistance and interdepartmental communication barriers by building non-punitive reporting culture.
- Developed and implemented company-wide quality and safety management systems, including establishing metrics; writing safety, quality, operations and security manuals; and setting up document control, data management, record retention and information exchange protocols.
- Promoted to Deputy Manager after 4 years; managed department, consisting of 8 auditors, for 8 months following retirement of quality manager.
- Became go-to person for understanding standards in preparation of audit checklists.
- Drove continuous improvement through internal audits, including analyzing findings, identifying and resolving root causes, and presenting reports to senior managers, including CEO.

Aerospace Research Institute Tehran, Iran
Intern Summer, 2006

EDUCATION

Virginia Commonwealth University Richmond, VA
Ph.D., Mechanical & Nuclear Engineering August, 2016
Dissertation: "Modeling Fluid Interactions with Granular and Fibrous Surfaces," supervised by Dr. Hooman Tafreshi. GPA: 4.00

- Used analytical formulation, computer simulation and experimental set-up to model two phase flow through granular and fibrous media.

Sharif University of Technology Tehran, Iran
MSc, Aerospace Engineering Month, 2009
Thesis: "Numerical Study of Diffusion Flame in Micro-Propulsion Systems"

- Developed a FORTRAN code to simulate diffusion flame by using Finite Element-Finite Volume Method (FEM-FVM) to simulate diffusion flame.

Amirkabir University of Technology (Tehran Polytechnic) Tehran, Iran
BSc, Aerospace Engineering Month, 2006

- Developed a C++ code to simulate aerodynamic coefficient of a six-degrees-of-freedom object.

HONORS AND AWARDS

- School of Engineering Dissertation Fellowship Award, Fall 2016, VCU, Richmond, VA.
- 1st place student poster competition, *American Filtration and Separation Society*, Spring Conference, May, 2016, Houston, TX.
- 1st place student poster competition, *American Filtration and Separation Society*, Annual Meeting, April, 2015, Charlotte, NC (https://www.youtube.com/watch?v=yJgNjn4p7QE).
- Outstanding Graduate Teaching Assistant Award, Engineering school, VCU 2015.

RELEVANT COURSEWORK AND RESEARCH INTERESTS AND ACTIVITIES

- Liquid absorption and Porous media
- Multiphase flow
- Thermodynamics
- Filtration and separation
- Combustion and heat transfer
- Interfacial phenomena
- Superhydrophobic Surfaces
- Computational fluid dynamics (CFD)

TECHNICAL AND EXPERIMENTAL SKILLS

- **Programming:** FORTRAN, C++, MATLAB, Mathematica, Surface Evolver, ANSYS Fluent, CATIA, AutoCAD, FlexPDE.
- **Experimental:** SEM, high speed imaging, VSM, microcharacterization, microfabrication.
- **General Skills:** Latex, Tecplot, Adobe Photoshop, Microsoft Office, Linux.

PUBLICATIONS AND CONFERENCE PRESENTATIONS

- **M.M. Amrei,** H.V. Tafreshi, Break-up Force of a Droplet Deposited on Trilobal Fibers, Colloids *and Surfaces A* (in preparation).
- N. Farhan, **M.M. Amrei,** A.A. Hemeda, H.V. Tafreshi, Capillarity of Heterogeneous Superhydrophobic Coatings of Multilayer Fibers, *Colloids and Surfaces A* (in preparation).
- **M.M. Amrei**, M. Davoudi, G.G. Chase, and H.V. Tafreshi, Effects of Roughness on Droplet Apparent Contact Angles on a Fiber, *Separation and Purification.* (under review).
- **M.M. Amrei**, D.G. Venkateshan, J. Atulasimha, H.V. Tafreshi, Novel Approach to Measure Droplet Detachment Force from Fibers, *Langmuir* (accepted).
- H. Aziz, **M.M. Amrei**, and H.V. Tafreshi, Modeling Cassie Droplets on Superhydrophobic Coatings with Orthogonal Fibrous Structures, *Colloids and Surfaces A* 512, 61–70 (2017).
- D.G. Venkateshan, **M.M Amrei**, A.A. Hemeda, Z. Cullingsworth, J. Corbet, and H. Vahedi Tafreshi, Failure Pressures and Drag Reduction Benefits of Superhydrophobic Wire Screens, *Colloids and Surfaces A* 511, 247–254 (2016).
- Hemeda, **M.M. Amrei**, H.V. Tafreshi, Wetting States of Superhydrophobic Surfaces Made of Polygonal Pores or Posts, *Journal of Applied Physics* 119, 175304 (2016).
- **M.M. Amrei**, H.V. Tafreshi, “Effects of Pressure on Wetted Area of Submerged Superhydrophobic Granular Coatings. Part II: Poly-Dispersed Coatings”, *Colloids and Surfaces A* 481 547–560 (2015).
- **M.M. Amrei**, H.V. Tafreshi, “Effects of Hydrostatic Pressure on Wetted Area of Submerged Superhydrophobic Granular Coatings. Part 1: Mono-Dispersed Coatings”, *Colloids and Surfaces A* 465, 87–98 (2015).
- T.M. Bucher, **M.M. Amrei**, H.V. Tafreshi, “Effect of Wetting Heterogeneity on Capillarity of Superhydrophobic Coatings with Orthogonally Layered Fibers”, *Surface & Coatings Technology* 277 117–127 (2015).
- Emami, A.A. Hemeda, **M.M. Amrei**, A. Luzar, M. Gad-el-Hak, and H.V. Tafreshi, “Predicting Longevity of Submerged Superhydrophobic Surfaces: Surfaces with Parallel Groove”, *Physics of Fluids* 25, 062108 (2013).
- Emami, S. Fotovati, **M.M. Amrei**, H.V. Tafreshi, “On the Effects of Fiber Orientation in Permeability of Fibrous Media to Power-Law Fluids”, *International Journal of Heat and Mass Transfer* 60, 375-379 (2013).
- **M.M. Amrei**, H.V. Tafreshi, Modeling Water Droplet Equilibrium Shape on Fiber with Trilobal Cross-Sections, accepted for presentation at Nanofibers*, Applications & Related Technologies (NART) conference*, Sept. 13-15 2016, Raleigh, NC.
- **M.M. Amrei**, H.V. Tafreshi, Detachment of a Droplet from Crossing Fibers, *American Filtration and Separation Society Spring Conference*, May 9-11 2016, Houston, TX.
- T.M. Bucher, **M.M. Amrei**, H.V. Tafreshi, Modeling Water Entry Pressure of Fibrous Materials, *American Filtration and Separation Society*, Annual Meeting, April 27-30 2015, Charlotte, NC
- M. Darbandi and **M.M. Amrei**, Numerical Study of Micro Diffusion Flame around a Micro Jet, 13*th Annual and* 2*nd international Fluid Dynamics Conference*, Oct 2010, Shiraz, Iran
- M. Darbandi and **M.M. Amrei**, Numerical Study of Diffusion Flame in Micro-Combustion, 9*th Iranian Aerospace Society Conference*, Feb. 2010, Tehran, Iran.